EXPERIMENTAL INVESTIGATION OF NUCLEATE BOILING AND THIN-FILM EVAPORATION ON ENHANCED SILICON SURFACES

by

SHAILESH MALLA

Presented to the Faculty of the Graduate School of

The University of Texas at Arlington in Partial Fulfillment

of the Requirements

for the Degree of

DOCTOR OF PHILOSOPHY

THE UNIVERSITY OF TEXAS AT ARLINGTON

May 2014

Acknowledgements

All my academic accomplishments belong to my parents, Bhumi Malla (mother) and Ram Bahadur Malla (father). Their passion for education and countless sacrifices for my higher education cannot be expressed in words. It is to them I dedicate this dissertation. I would like to thank my beloved sister, Sangita M. Rana and brother, Santosh Malla for all their support and encouragement. I would also like to thank my brother-in-law, Prem Rana.

I am thankful to my supervising professor Dr. Hyejin Moon and Dr. Seung Mun You for allowing me to participate in their research activities. Guidance of Dr. Miguel Amaya cannot be forgotten. His efforts in resolving various issues were valuable. Next, I would like to thank all my past and present lab members. Their support and friendship have always been motivational.

April 08, 2014

Abstract

EXPERIMENTAL INVESTIGATION OF NUCLEATE BOILING AND THIN-FILM EVAPORATION ON ENHANCED SILICON SURFACES

Shailesh Malla, PhD

The University of Texas at Arlington, 2014

Supervising Professor: Hyejin Moon

The present work consists of two major studies. The first study investigates the effects of surface energy or wettability on nucleate pool boiling and the second study investigates the thin-film evaporative cooling for near junction thermal management. For the first study, effects of surface energy or wettability on critical heat flux (CHF) and boiling heat transfer (BHT) of smooth heated surfaces was studied in saturated pool boiling of water at 1 atm. For this purpose hydrophilic and hydrophobic surfaces were created on one side of 1cm x 1cm double-side polished silicon substrates. A resistive heating layer was applied on the opposite side of each substrate. The surface energies of the created surfaces were characterized by measuring the static contact angles of water sessile drops. To provide a wide range of surface energies, surfaces were made of Teflon (hydrophobic), bare silicon (hydrophilic) and aluminum oxide (most hydrophilic). The measured contact angles on these surfaces were ~108, ~57 and ~13 degrees respectively. The results of pool boiling tests on these surfaces clearly illustrate the connection between surface energy and CHF. CHF was shown to linearly decrease with contact angle increase, from ~125 W/cm^2 on aluminum oxide (most hydrophilic) to nearly one tenth of this value on Teflon (hydrophobic). The most hydrophilic surface also produced increasingly better BHT than plain silicon and Teflon as heat flux increased. However, below ~5 W/cm^2 the

hydrophobic surface demonstrated better heat transfer due to earlier onset of nucleate boiling, reducing surface superheats by up to ~5 degrees relative to the other two surfaces. Above ~5 W/cm^2 the BHT of the hydrophobic surface rapidly deteriorated as superheat increased towards the value at CHF. To further understand the effect of surface energy on pool boiling performance, the growth and departure of bubbles from single nucleating sites on each surface were analyzed from high-speed video recordings. A distinct bubble behavior was observed in the hydrophobic surface where bubble growth and departure period was extremely long compared to plain silicon and aluminum oxide surfaces.

This study also investigated the performance of thin-film evaporative cooling for near-junction thermal management. A liquid delivery system capable of delivering water in small volumes ranging 20~75 nl at frequencies of up to 600 Hz was established. On one side of the silicon chip, a resistive heating layer of 2 mm x 2 mm was fabricated to emulate the high heat flux hot-spot, and on the other side a superhydrophilic nanoporous coating (SHNC) was applied over an area of 1 cm x 1 cm. With the aid of the nanoporous coating, delivered droplets spread into thin films of thicknesses less than 10μm. With this system, evaporative tests were conducted in ambient in an effort to maximize dryout heat flux and evaporative heat transfer coefficient. During the tests, heat flux at the hot spot was varied to values above 1000 W/cm^2. Water was delivered at either given constant frequency (constant mass flow rate) or at programmed variations of frequency (variable mass flow rate), for a given nanoliter dose volume. Heat flux and hot spot surface temperatures were recorded upon reaching steady state at each applied heat flux increment. Relative to bare silicon surface, dryout heat flux of the SHNC surface was found to increase by ~5 times at 500~600 Hz. Tests were also conducted at various system pressures and temperatures in a micro-gap to emulate the actual embedded thermal management system. The micro-gap was made by positioning a top cover plate 500 μm above the test surface. System

temperature did not influence the hotspot temperature. This was due to the formation of near saturation temperature inside the micro-gap for all cases as a result of vapor accumulation. Increase in system pressure increased the hotspot temperature. At 1500 W/cm^2, hotspot temperature increased by 6^oC and 24^oC by increasing the system pressure by 7.32 and 14.7 psi respectively. This was due to increase in saturation point as a result of increase in pressure.

On the SHNC surface a mixed mode of heat transfer comprising of thin-film boiling and thin-film evaporation was observed particularly at moderate heat flux (~700 W/cm^2). To further enhance the heat transfer coefficient, aluminum microporous coating was developed that increased the number of nucleation sites for thin-film boiling and also maintained the wettability for thin-film evaporation at higher heat fluxes. Test results showed a marginal improvement in dry-out heat flux compared to SHNC, however, significant reduction was achieved in hot-spot temperature at all heat flux levels. A net reduction of ~ 58^oC was obtained at ~1600 W/cm^2 by using aluminum based microporous coating.

Table of Contents

List of Illustrations

List of Tables

Chapter 1

Introduction

1.1 Background

Phase change heat transfer is one of the most effective cooling mechanisms used in applications like microelectronics, nuclear power plant cooling etc. The efficacy of phase change cooling comes from the latent heat of vaporization associated with the working fluid. Most common phase change heat transfer techniques are pool and flow boiling, jet impingement and spray cooling. Operating range of these cooling schemes is highly dependent on the choice of working fluid and the heated surface structure. For example, refrigerants are efficient in cooling applications that dissipate low heat fluxes while water is used in cooling high heat flux applications because of its much higher latent heat of vaporization, as shown in Table 1.1.

Table 1-1 Commonly Used Refrigerant

Fluid	Latent Heat of Vaporization (KJ/Kg)
Water	2400
FC-72	88
HFE-700	108
R-134a	198

Surface topography plays equally important role in phase change heat transfer. A number of works have been reported that incorporate surface modification to enhance the heat transfer. Honda et al. [1] demonstrated CHF enhancement by using micro pin fins with and without sub-micron scale roughness. Ujereh et al. [2] examined the effects of carbon nano tube arrays on nucleate pool boiling and observed dual enhancement in nucleate boiling heat transfer (BHT) coefficient and CHF. You et al. [3] demonstrated a dramatic increase in CHF using nanofluid. Recently Moreno et al. [4] used sintered porous structure

and reported an enhancement by over 300% in heat transfer coefficient. Kaviany and Liteer [5] fabricated a modulated porous layer for pool boiling CHF enhancement. There are several other works that have successfully shown the drastic reduction in surface temperature by tailoring the surface. These surfaces yield CHF values that are higher than the ones predicted by well-established correlations. This could be due to the lack of integration of surface parameters. For instance, wettability and micro structures [6] [7] can complicate the boiling phenomena. The correlations that attempt to employ surface wettability in the form of contact angle measurement, do not address surface roughness. One prime focus of the current investigation is to study the effect of surface energy (wettability) only on CHF and BHT. Any effects from surface roughness are eliminated by using polished silicon surface.

The current study also aims to implement phase change heat transfer for cooling localized high heat fluxes or hot-spots in microelectronics. In recent years, the rapid evolution of integrated circuit design has surfaced the issue of increased power dissipation, leakage power and non-uniformity in heat distribution. Hot-spots have become more prevalent and their cooling has become of primary concern to operate the system without degrading performance and reliability. Conventional cooling techniques like air cooling are not a viable option due to fundamental limitations on cooling performance primarily at higher heat flux. Phase change heat transfer by thin-film evaporation is intended for thermal management of hot-spot. Water is the preferred coolant due to high latent heat of vaporization as shown in Table 1.1. The efficiency of thin-film evaporation comes from the reduced thermal resistance across the water film thickness. The thinner the water film, the lower is the surface temperature due to faster evaporation. Hence, surface wettability is critically important to enhance thin-film evaporation. A number of surface modification techniques has been established in recent studies to enhance wettability. This includes

dispersion of nanoparticles, photo induced hydrophilicity, micro patterning and porous coating. In this study, an attempt will be made to establish a surface that promotes wettability and thin-film evaporation.

1.2 Project Objectives

The main objective of this study is to assess the enhancement in heat transfer coefficient and critical heat flux/dry-out heat flux using enhanced surfaces. For this, the project is divided into two major portions each with multiple objectives. The first portion of the study utilizes pool boiling as heat transfer mechanism. This will investigate the effects of wettability on heat transfer performance. The nobility of this study is that wettability is induced on a polished silicon surface without altering the surface roughness. Heat transfer coefficient and the critical heat flux will be the focal point of discussion. The second part of the study is conducted with the intention to create thin-film evaporation similar to microlayer evaporation in bubble nucleation in pool boiling but at higher frequency on a localized high heat flux area. The objectives and goals of the two major portions of the study are listed below.

1. Investigation of the effects of wettability on heat transfer coefficient and critical heat flux.
    - 1.1 Fabrication of robust thin film heater on silicon substrate that can survive up to critical heat flux (CHF)
    - 1.2 Fabricate surfaces with wettability ranging from highly hydrophilic to hydrophobic without altering the surface roughness
    - 1.3 Quantify the enhancement in CHF and BHT
    - 1.4 Bubble dynamics study at lower heat flux for all testing surfaces
    - 1.5 Effects of surface orientations
2. Thin-film evaporation of water on enhanced surfaces for high heat flux dissipation

2.1 Establish liquid delivery system capable of delivering liquid droplet in small doses and high frequency

2.2 Fabricate a resistive layer that serves as heater and temperature sensor

2.3 Develop superhydrophilic coating that transforms the water droplet into thin film upon contact

2.4 Study the effects micro-gaps, system pressure and temperature

With respect to the first objective, three different surfaces aluminum oxide coated silicon (highly wettable), plain silicon substrate (moderate wettability) and Teflon coated silicon (hydrophobic) were fabricated and tested in pool boiling. Atomic force microscope was used to quantify the surface roughness of all surfaces. Test results were compared to analyze any effects of wettability on BHT and CHF. High speed filming was conducted at lower heat flux for all the surfaces to understand the bubble dynamics. All the results from this study is described in chapter 2.

For the second objective of the study, thin-film evaporation tests were conducted on a superhydrophilic nanoporous coating (SHNC) and aluminum microporous coating. These tests were also repeated at various system pressure and temperature. Tests were also conducted in gassy situation in a micro-gap to emulate the embedded thermal management system. All the test results from this study is discussed and compared in chapter 3 and 4.

Chapter 2

Nucleate Boiling on Silicon Surfaces with Different Wettability

Nucleate boiling is an efficient heat transfer mechanism where heat is transferred from a heated surface to surrounding fluid. The incipience of bubble from a heated surface, its growth and departure is primarily responsible for intense heat removal from the heated surface. The drawback of nucleate boiling is its application envelope, which is limited by a phenomenon called critical heat flux (CHF) where a rapid temperature rise occurs. The arrival of CHF in cooling system can result in system failure. This phenomenon still remains unclear after decades of research in various fronts. Efforts have been made to delay this point. Surface modification technique like micropillars, nanorods, microporous coating, dispersion of nanoparticles etc. has been often implemented to delay CHF.

A number of models have been established to predict CHF. However, there still lacks a model that incorporates all the factors influencing phase change heat transfer. Surface energy or surface wettability has been abandoned in most of all the well-known correlations. The main focus of this chapter is to investigate any influence surface energy has on CHF and boiling heat transfer (BHT). The effect of surface energy or wettability will be isolated from the effect of surface roughness (microscale) by using polished silicon surface.

2.1 Fundamentals of Nucleate Pool Boiling

Pool boiling process is dependent on thermo-physical properties of the working fluid, surface material, structure and number of nucleation cavities on the surface, size of the heated surface and applied heat flux. The different regimes of pool boiling like nucleate

boiling and CHF as shown in Fig. 2.1 is observed even with the variation of these parameters.

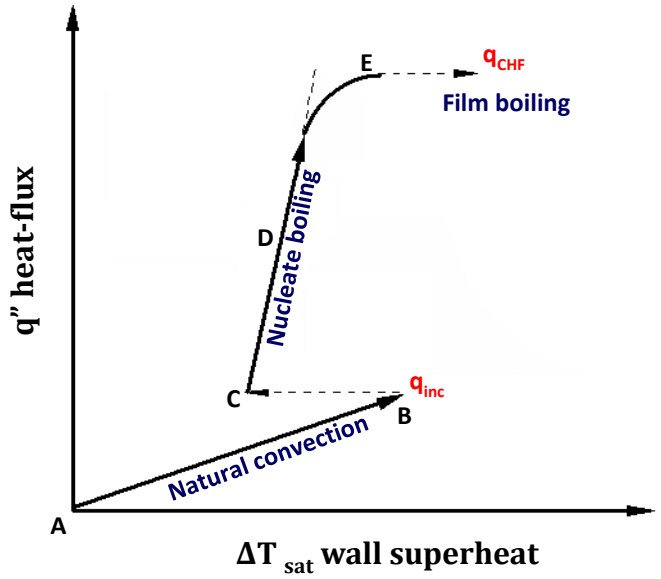

Figure 2-1 Typical Pool Boiling Curve

At low heat flux, heat transfer from the heated surface to the bulk liquid occurs by natural convection, corresponding to segment AB of Fig.2.1. The motion of the working fluid caused by density gradient is primarily responsible for this mode of heat transfer. Natural convection possesses lower heat transfer coefficient. Hence, wall superheat increases faster with heat flux. Natural convection is usually suppressed in surfaces where nucleation occurs at a very small wall superheat like boiling of porous structure in water [8]. On the other hand, natural convection regime magnifies if wall superheat required for nucleation is higher like boiling in refrigerants [9]. Increase of heat flux beyond natural convection results in the nucleation of bubbles on heated surface. The details of nucleation criterion will be discussed in section 2.3.1. Point B in Fig. 2.1 identifies the onset of nucleate boiling. This jump from point B to C is seen when heat flux is controlled. At the initial stage of nucleate boiling (CD in Fig. 2.1), bubbles are isolated due to fewer and

widely separated active nucleation sites. As the heat flux increases, the number of nucleating sites also increases [10] [11] [12]. At sufficiently higher heat flux, bubbles are located so close that the adjacent bubbles merge before departure. This regime, represented by section DE in Fig. 2.1 is also referred as regime of slugs and columns as the rapidly growing bubbles merge to form columns of vapor slugs. Eventually, the drag of vapor column on liquid becomes so severe that the liquid could not reach the heated surface on time resulting in a large temperature spike. This point is the CHF and is represented by point E in Fig. 2.1. Investigation on CHF has a long history and has yielded a number of correlations for predicting CHF. A complete account of all the attempts made to date is beyond the scope of this chapter. However, some of the models relevant to the current study are mentioned. One of the widely accepted models to predict CHF is provided by Zuber [13], which is given by:

$$q_{CHF,Zuber's} = 0.131\rho_v h_{lv}\left[\frac{\sigma\,(\rho_l-\rho_v)g}{\rho_v^2}\right]^{\frac{1}{4}} \tag{2.1}$$

This model attributes CHF to the instability of the vapor column leaving the surface. This model like most of other models does not incorporate influence of geometry and wettability of the heated surface. This model oftentimes under-predicts CHF. The effect of surface geometry on CHF was studied by Lienhard et al. [14], Sun et al. [15] and Ded et al. [16]. There is an abundance of experimental studies that attempt to address wetting behavior and the roughness of the test surface. Chowdhury and Winterton [17] found nucleate boiling heat transfer unaffected by contact angle value. However, they reported the enhancement with increasing surface roughness by relating heat flux and number of active nucleation sites. Takata et al. [18] reported CHF enhancement and excellent heat transfer characteristics during nucleate boiling in a photo induced superhydrophilic surface. Liaw and Dhir [19] reported a significant influence of surface wettability on transition boiling

heat fluxes. Takata et al. [20] demonstrated a stable film boiling in super hydrophobic surface. Kirishenko and Cherniakov [21] were one of the few researchers to incorporate surface energy in CHF correlation as given by:

$$q_C^{"} = 0.171 h_{fg}\sqrt{\rho_g}[\sigma g(\rho_l - \rho_g)^{1/4} \frac{(1+0.324.10^{-3}\beta^2)^{1/4}}{\sqrt{0.018\beta}} \quad (2.2)$$

The authors reported close agreement of this correlation with the experimental data for the contact angle within 20-60 degrees. Haramura and Katto [22] described CHF as a consequence of liquid macrolayer dry-out under large mushroom shaped bubbles hovering above the heated surface preventing inflow of liquid. Their expression of CHF is given by:

$$q_{CHF}^{"} = \rho_f h_{fg} \delta_e (1-\alpha) f_m \quad (2.3)$$

In this equation "δ_e" is an expression of macrolayer thickness which incorporates the effect of contact angle [23]. Kandlikar [24] developed a theoretical model to predict CHF in pool boiling that includes dynamic receding contact angle, β, and is given by:

$$q_c^{"} = h_{fg}\rho_g^{\frac{1}{2}}\left(\frac{1+cos\beta}{16}\right)[\frac{2}{\pi} + \frac{\pi}{4}(1+cos\beta)cos\emptyset]^{1/2}[\sigma g\left(\rho_l - \rho_g\right)]^{1/4} \quad (2.4)$$

Equation 2.4 predicts the CHF for saturated pool boiling incorporating hydrodynamic and non-hydrodynamic interaction. The receding contact angle used in this model is the index of wettability and ϕ is the surface orientation. This was one of the few models that directly incorporated wettability through contact angle.

In order to understand the CHF mechanism it is also important to understand how the bubble interacts with surfaces of different wettability in terms of bubble generation, growth and departure. When a bubble grows out of an active nucleation site, it goes through mainly two different growth processes, which are inertia controlled and heat transfer controlled growth [25]. During the inertia controlled growth, a rapid growth occurs and the bubble assumes a near hemispherical shape. A wedge shaped, thin liquid microlayer is left

in between the liquid vapor interface near the base and the heated wall. Figure 2.2 illustrates the different regions of bubble growth from a heated surface. There exists a dry-spot at the center of the base of the bubble. This dry-spot increases in size during microlayer evaporation. Heat and mass transport through the microlayer evaporation significantly influences the overall heat transfer. At some point in the growth process, the heat transfer to the interface becomes a limiting factor and growth from this point onwards is heat transfer controlled growth. This is also indicated by transformation of bubble shape from hemispherical to spherical [25].

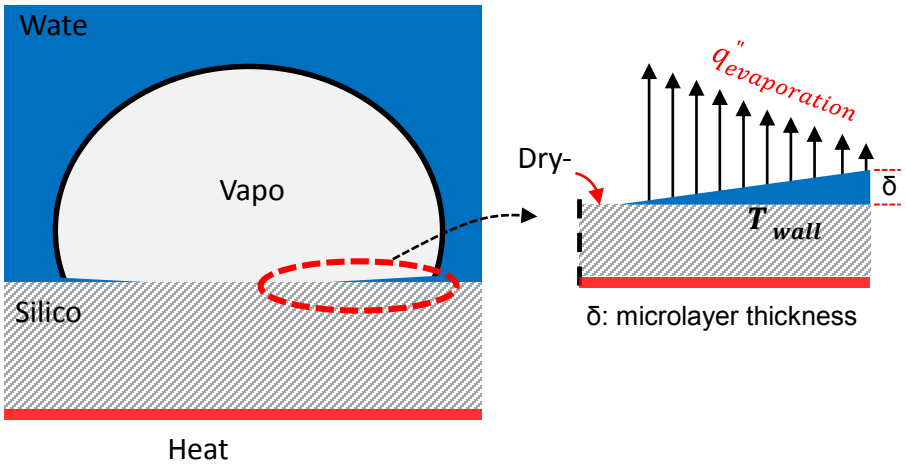

Figure 2-2 Different Regions of a Growing Bubble on a Heated Surface

Mikic and Rohsenow [26] proposed a correlation for heat transfer in nucleate boiling that includes the effects of surface characteristics. This correlation assumes transient heat conduction to be the most important contributor of heat transfer in nucleate boiling. In doing so, it completely sidelines heat transfer through microlayer evaporation. Jawurek [27] observed microlayer geometry and bubble dynamics simultaneously using an optical technique. They reported that the microlayer becomes progressively thinner with time near the dry spot. Everywhere else the microlayer local thickness increases with time

due to continuous replenishment of liquid. Cooper and Lloyd [28] estimated the thickness of this microlayer using a simplified hydrodynamic theory given by:

$$\delta = 0.8\sqrt{\nu\, t_g} \tag{2.5}$$

This estimate of microlayer thickness does not include the effect of wettability or surface energy. In a more recent study Zhao et al. [29] proposed a new microlayer model to predict heat transfer in nucleate boiling region including CHF. This theoretical model attributes the heat transfer during nucleate boiling to microlayer evaporation. In an effort to understand the microlayer structure in nucleate boiling Utaka at al. [30] measured the microlayer thickness by employing the laser extinction method. They reported the reduction in microlayer thickness over time due to evaporation. The initial microlayer thickness was found to increase linearly from the site of bubble incipience. Their results are in agreement with the numerical calculation and the ones reported by other researchers. However, there still lacks a model or understanding of microlayer that incorporates the surface energy. The direct analysis of the microlayer underneath a bubble is beyond the scope of this study. However, the alteration of surface wettability without changing the roughness will indicate the effects of microlayer evaporation on heat transfer performance.

2.2 Experimental Apparatus and Procedure

2.2.1 Test Vessel

A schematic of the test vessel used for pool boiling tests is shown in Fig. 2.3. The test vessel consists of an aluminum chamber with the dimensions of 15 cm (width) x 15 cm (height) x 22cm (depth). There are two glass viewports for high speed camera recording of bubble growth and departure. Temperature inside the chamber (both liquid and vapor) and heater temperature were measured using T-type thermocouples. An Omega PX 302 pressure transducer, which has a range of 0~50 psia, measured and monitored chamber

pressure. Two cartridge heaters (1000W) heated and degassed the working fluid in the boiling chamber. The top cover plate of the chamber was connected to a condenser through a Swagelok valve in order to prevent the loss of working fluid during degassing. The condenser was connected to a chiller. Band heaters were attached to two sides of the test vessel in order to maintain saturation temperature of the working fluid. These band heaters were controlled by a PID controller.

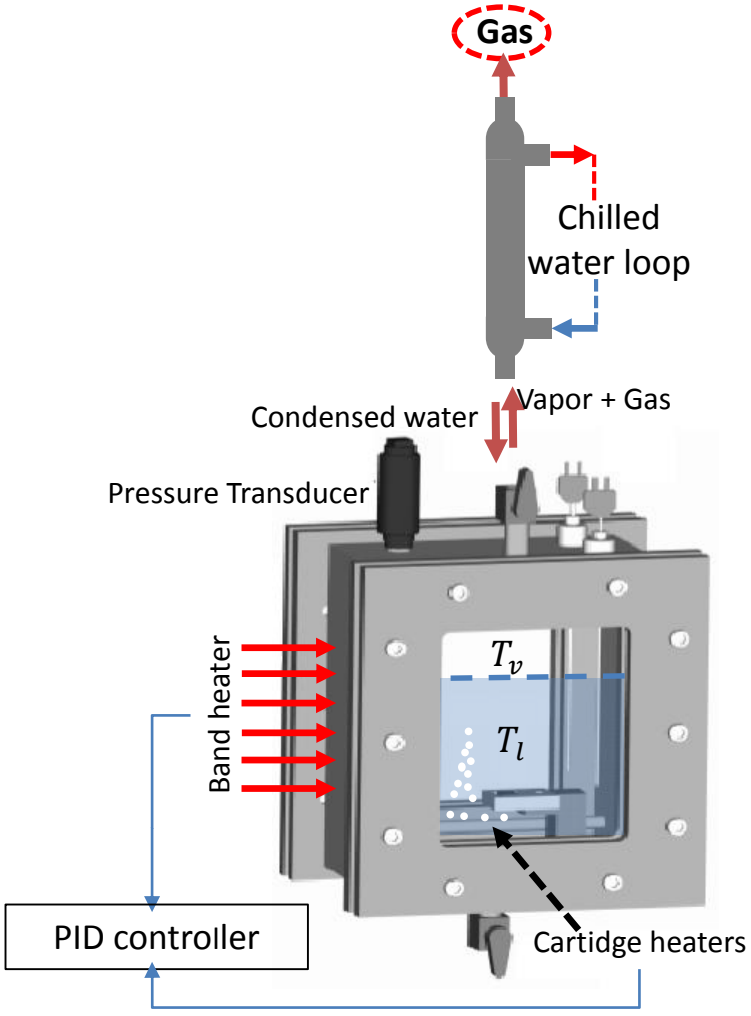

Figure 2-3 Pool Boiling Vessel

2.2.2 Test Heater Preparation

Different features of the thin-film heater were fabricated by photolithography and patterning processes. All the films were deposited at room temperature in an argon atmosphere. The base pressure of deposition was 2×10^{-7} Torr. A step-by-step description is given in Fig. 2.4. The heater was fabricated on one side of the wafer and the other side (bottom surface in Fig. 2.4(a)) was reserved for the test surface. As illustrated in step 1, three layers were laid on the silicon. The silicon was insulated by sputtering silicon nitride. A very thin film of titanium with a thickness of 80 nm was deposited on top of the silicon nitride. This titanium film acts as a resistor of the heater. In order to solder the thermocouple at the center of the resistor, a small portion of the surface needs to be metalized with nickel. It is also necessary to insulate this portion before metallization.

As shown in step 2 of Fig. 2.4(a), the center portion is open and everywhere else is covered with photoresist using photolithography. After depositing a thick layer (0.4 μm) of silicon nitride (step 3), photoresist was stripped off the surface (step 4). As shown in steps 5 and 6, the surface was coated with photoresist in such a way that during sputtering three areas were metalized, a 3mm x 3mm area at the center for thermocouple attachment, and two 1mm x 10mm areas on the edges to serve as buss bars (steps 7, 8). After removing the photoresist, fabrication was complete. After fabrication, the heaters were diced into 10mm x 10mm pieces. During dicing process, the residue from the dicing marks can scratch the resistive layer. Hence, both sides of the surface was masked by spin-coating photoresist which can be easily removed once the dicing process is complete. Figure 2.4(b) shows an exploded view of a piece with thermocouple attached and Fig. 2.4(c) shows a view from the bottom.

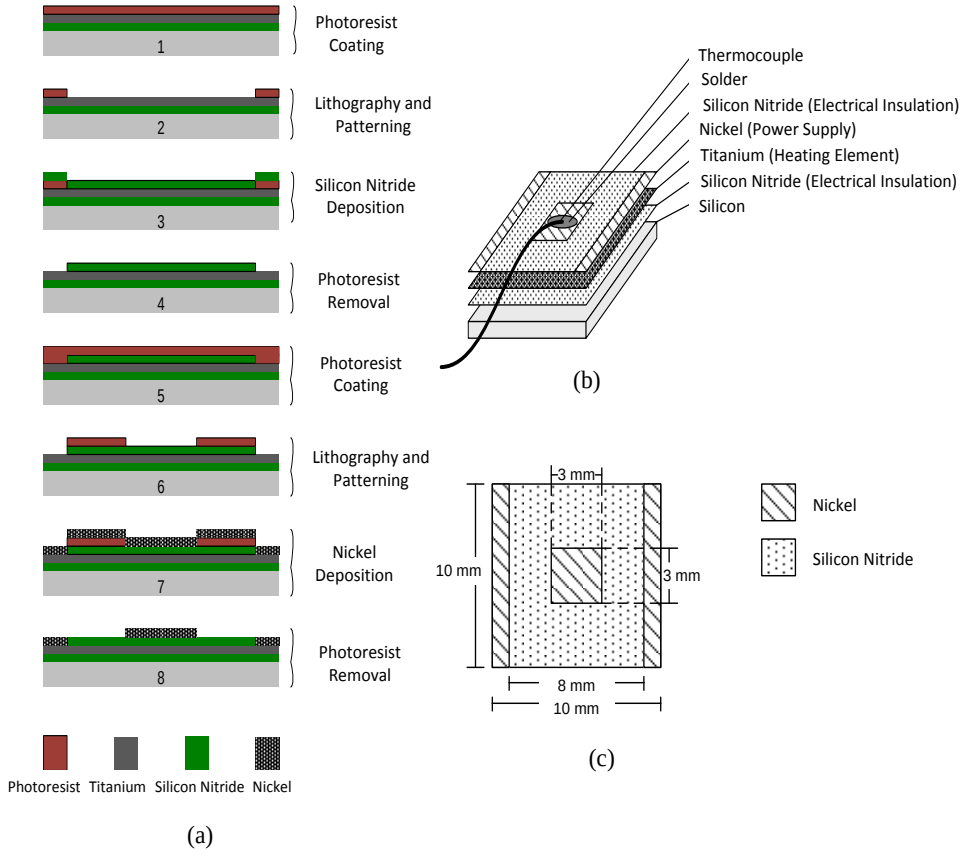

Figure 2-4 Thin Film Heater, (a) Fabrication Process, (b) Exploded View and (c) Side View

To prepare further the heater for a test, copper wires were soldered to the buss bars. The wired heater was then mated to a Lexan plate for mounting and insulation, and was surrounded with epoxy to fix it in place, leaving the test surface exposed and flush with the epoxy level. The epoxy prevents perimeter boiling and provides additional insulation. A schematic of the prepared heater is shown in Fig. 2.5.

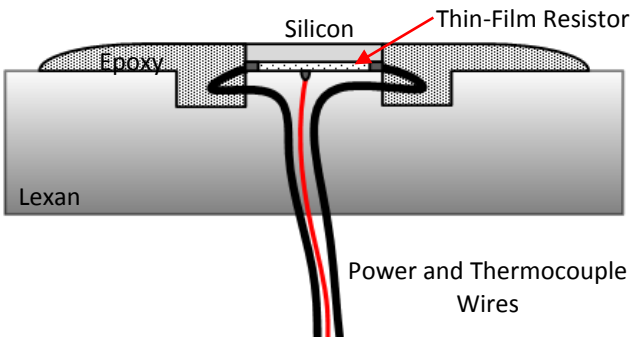

Figure 2-5 Assembled Test Heater

2.2.3 Test Surface Preparation and Wettability Measurement

Three different surfaces were prepared for testing on the 10mm x 10mm pieces, which were plain silicon, aluminum oxide (Al_2O_3) and Teflon surface. The aluminum oxide test surface was deposited in a thin layer of 100 nm thickness by RF sputtering. During this process, the silicon wafer was rotated at a frequency of 3000 RPM in order to maintain uniformity across the wafer. To fabricate the Teflon test surface, a Teflon solution was prepared by dissolving Teflon amorphous fluoropolymer into FC40 in 4% wt/vol. ratio. This solution was spin-coated on the silicon substrate at 3000 RPM. The coating was heat-treated at 250^{o}C to strengthen its bonding in order to insure that it survived the pool boiling test. The plain silicon test surface was obtained after dipping the wafer in very dilute hydrofluoric acid (HF) solution in order to remove the native oxide.

The present study aims to provide a range of wettability without altering surface roughness. Hence, a polished silicon was used as a substrate and thin film deposition was used to alter its surface energy. In order to confirm surface roughness integrity after thin film deposition, atomic force microscope (AFM) was used to obtain mean roughness of the surface. All the images gathered from AFM analysis are demonstrated in Fig.2.6. The scan was conducted in a scan size of 2 µm using a fast scan AFM provided by Bruker.

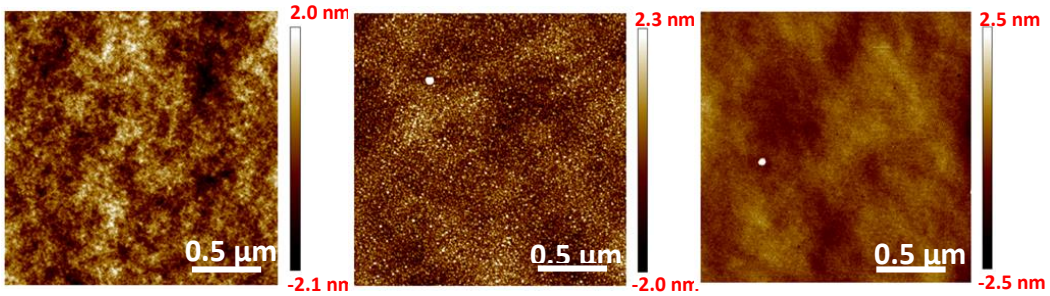

Figure 2-6 AFM Images of All Test Surfaces

Again, the objective here is to induce diverse surface wettability without altering the surface roughness. And the deposited films, Teflon and aluminum-oxide, have a very small thickness of ~150 nm and ~100 nm respectively, which are believed to maintain the surface roughness closer to the plain surface. As shown in table 2.1, the increase in surface roughness by Teflon and aluminum oxide deposition is very small.

Table 2-1 Surface Roughness Measurement Obtained from AFM

Surface	R_a (nm)	R_q (nm)
Teflon	0.450	0.570
Aluminum-oxide	0.475	0.610
Plain Silicon	0.287	0.385

The wettability on thus prepared samples was quantified by static contact angle (θ) between liquid-vapor interface and the solid surface as shown in Fig.2.7. In Fig.2.7 σ_{lv},σ_{sv}, σ_{sl} represent the interfacial tension along liquid-vapor, solid-vapor and solid-liquid interface respectively.

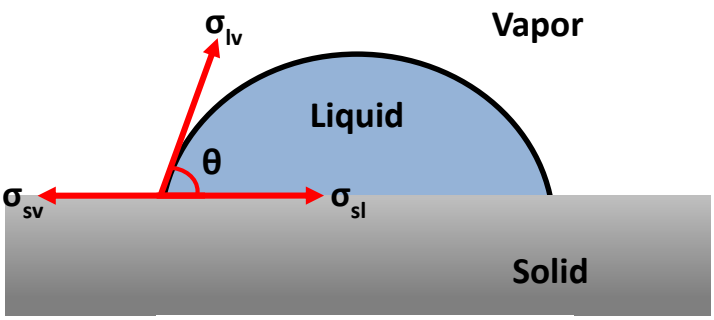

Figure 2-7 Interfacial Tension Forces Acting along Different Interfaces

At equilibrium, the force balance along horizontal axis results in equation 2.6 which is also known as Young's equation.

$$\Sigma_{sv} = \sigma_{sl} + \sigma_{lv} cos\theta \tag{2.6}$$

$$cos\ \theta = \frac{\sigma_{sv} - \sigma_{sl}}{\sigma_{lv}} \tag{2.7}$$

Based on equation 2.7, the solid surface can be classified into hydrophilic and hydrophobic as shown by the inequalities:

$$\text{Hydrophilic} \qquad 0 < cos\ \theta = \frac{\sigma_{sv} - \sigma_{sl}}{\sigma_{lv}} < 1 \tag{2.8}$$

$$\text{Hydrophobic} \qquad -1 < cos\ \theta = \frac{\sigma_{sv} - \sigma_{sl}}{\sigma_{lv}} < 0 \tag{2.9}$$

For the present study, if $cos\theta$ in hydrophilic surface approaches to 1, the surface is called highly hydrophilic. Liquid has higher affinity for hydrophilic surfaces compared to hydrophobic surfaces.

Contact angle was assessed using a goniometer. The images of static contact angle on all the surfaces and their respective measurements over a period of 60 seconds are shown in Fig.2.8. For the measurement, the test surface was positioned ~5 mm below a syringe that delivers a distilled water droplet of 20µl volume. The goniometer automatically takes measurements at a given frequency beginning as soon as the droplet

touches the surface. The contact angle values reported are those obtained in the 60th second of measurements.

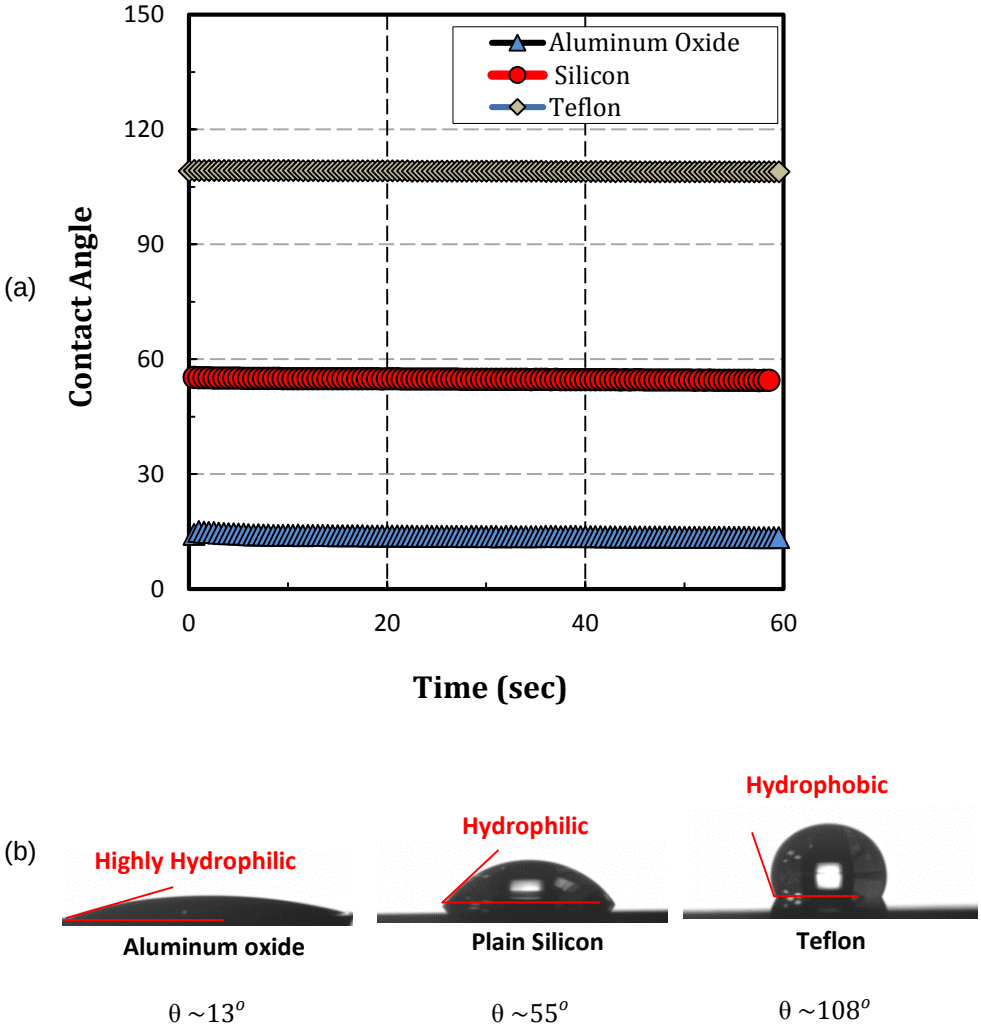

Figure 2-8 (a) Contact Angle Measurement of Three Different Surfaces for a Period of 60 Seconds and (b) Snapshot of Static Contact Angle at t = 60 sec.

2.2.4 Experimental Procedure

Cleanliness of the test vessel and working fluid is crucial for pool boiling tests on a silicon surface. Amounts of foreign matter that would be inconsequential in pool boiling

of rough surfaces can change boiling behavior of silicon. Hence, the test vessel was thoroughly rinsed in distilled deionized water prior to each test. After cleaning the vessel, the test fluid (distilled-deionized water) was poured into the vessel and the top cover, with test heater attached, was secured in place. Just prior to the test, the attached condenser was opened to ambient through a valve in order to allow non-condensable to vent during degassing. Heating power was then applied to the cartridge and band heaters, and once the test fluid was heated to saturation temperature, heating power was kept on for an additional 45 minutes to degas the working fluid. During degassing, as the non-condensable vented through the condenser, the water that condensed continuously flowed back by gravity into the test vessel. At the end of 45 minutes, the cartridge heaters were shut down, the valve on the condenser was closed and the band heaters, which are connected to a temperature controller, maintained the test fluid at saturation temperature ($100^{o}C$). The pressure was checked to ensure that it corresponded to the saturation temperature.

A LabVIEW program controlled the power supply to the test heater and the data acquisition system. To start the test, heating power was applied to the test heater. Four-wire method was used for the power supply measurement. This method can be explained with the aid of Fig.2.9. Here two of the four wires supplied power to the heater and the remaining two wires measured the voltage drop across it. A shunt was connected in series with the heater. The known resistance of the shunt was used to calculate the value of the current in the circuit which along with the voltage drop measurement across the heater was used to calculate the power.

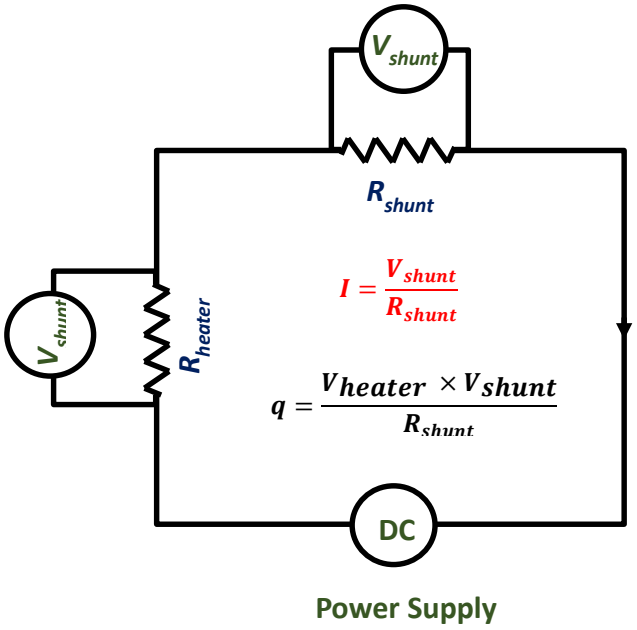

Figure 2-9 Circuit of Four Wire Method

The temperature from the thermocouple attached to the heater was monitored every half second for 50 seconds, the values were averaged, and the process was repeated for the next 50 seconds. If the difference between consecutive averages was below 0.1°C, steady-state was assumed, and the thermocouple temperature and applied heating power were recorded. Heating power was then incremented to the next programmed level, and temperatures and power were again recorded upon reaching the new steady-state. This process continued until the CHF was reached. The program assumed that the CHF condition was reached when the temperature of the heater exceeded the previously recorded steady-state temperature by more than 20°C. The power to the heater was then shut down and all data including temperatures, pressure, and power were saved.

2.2.5 Uncertainty Analysis

Power values were obtained from measurements of the voltage drop across the test heater (V_{heater}) and the voltage drop across a reference resistor (V_{shunt}) connected in series. Using these voltage measurements, heat flux was calculated by:

$$q^{"} = \frac{V_{heater} V_{shunt}}{R_{shunt} A_{heater}} \tag{2.10}$$

where R_{shunt} is the resistance value of the reference resistor or shunt, and A_{heater} is 1cm^2. Uncertainty analysis is conducted using method by Kline and McClintock [31] and the calculation procedure is shown below.

$$U_{q^{"}} = f(V_{heater}, V_{shunt}, A_{heater}, A_{shunt}) \tag{2.11}$$

$$U_{q^{"}}^2 = \left(\frac{\partial q^{"}}{\partial V_{heater}}\right)^2 U_{V_{heater}}^2 + \left(\frac{\partial q^{"}}{\partial V_{shunt}}\right)^2 U_{V_{shunt}}^2 + \left(\frac{\partial q^{"}}{\partial R_{shunt}}\right)^2 U_{R_{shunt}}^2 + \left(\frac{\partial q^{"}}{\partial A_{heater}}\right)^2 U_{A_{heater}}^2 \tag{2.12}$$

$$\boxed{U_{q^{"}}^2 = q^{"2}\left[\frac{U_{V_{heater}}^2}{V_{heqter}^2} + \frac{U_{V_{shunt}}^2}{V_{shunt}^2} + \frac{U_{R_{shunt}}^2}{R_{shunt}^2}\right]} \tag{2.13}$$

Using equation 13 and considering heat losses estimated by finite element analysis to be less than 1%, the uncertainty in heat flux measurement is below 5%. The temperature and the pressure measurements were estimated to have less than ±0.5^{o}C error and ±0.25% error in full scale including calibration error, respectively.

2.3 Test Result

2.3.1 Effects of Surface Wettability

The surfaces characterized in section 2.2.3 were subjected to pool boiling test to assess the influence of wettability on CHF and boiling heat transfer (BHT). The pool boiling tests were conducted in atmospheric pressure and saturation temperature. Test results are shown in Fig. 2.10.

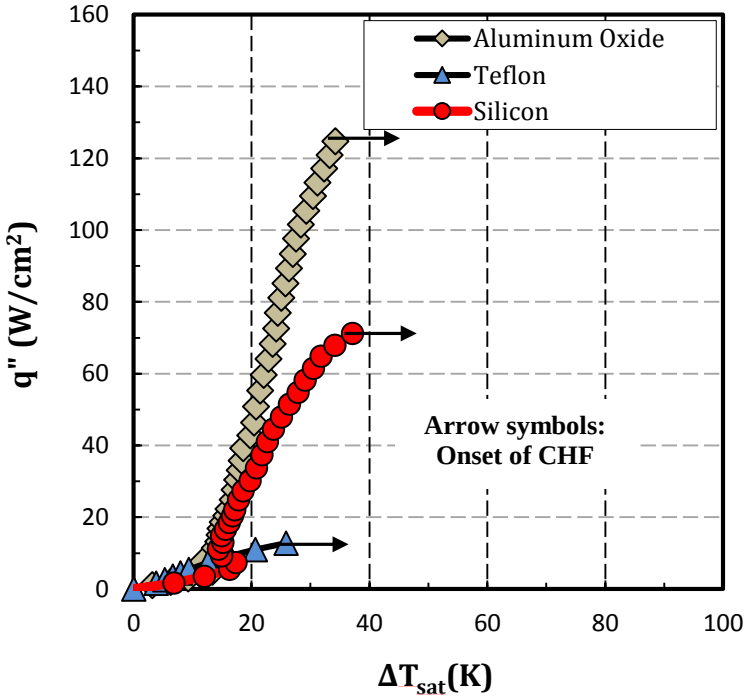

Figure 2-10 Pool Boiling Curves for Test Surfaces of Different Wettability

Again, the substrate used is polished silicon and the thin films deposited on it to establish a range of wetting surfaces are in the angstrom level. Hence, the surface roughness was found to be in nanoscale. This fabrication of wettable and non wettable surface condition without altering the surface roughness separates the current work from the previous studies. Here, the nucleation sites are much smaller as compared to the micron scale conventional cavities. These surfaces demonstrate heterogeneous boiling

similar to normal pool boiling tests. The most hydrophilic aluminum oxide surface (θ = 13°) yields a CHF of ~125 W/cm^2, which is 84% higher than that of the less hydrophilic plain silicon surface (θ = 57°). The hydrophobic Teflon surface (θ = 108 °) yields the lowest CHF, lower by 81% than that of plain silicon surface. The CHF values vs. contact angle are plotted in Fig. 2.11 and this shows that CHF varies linearly with contact angle, with higher CHF as contact angle decreases.

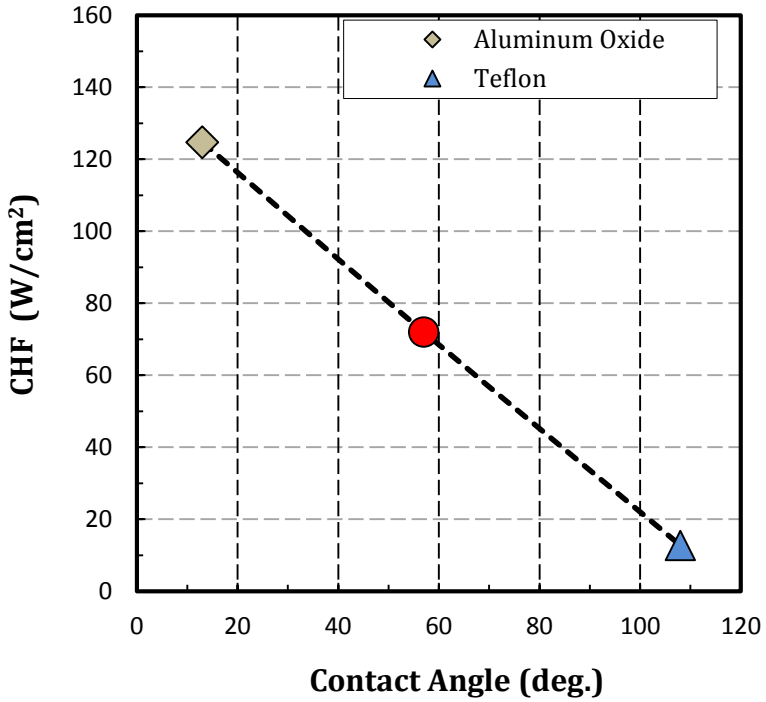

Figure 2-11 Relationship of CHF with Static Contact Angle

This result is consistent with that of Kwark et al. [32], although they worked with nanoparticles on a copper substrate. They generated different wettability by depositing aluminum oxide nanoparticles through nanofluid boiling to form nanoporous layers of different thicknesses and roughnesses. They showed that CHF and contact angle values were linearly related, with higher CHF as contact angle decreased. The current result of Fig. 2.11, even though follows a straight line different from Kwark et al. [32], confirms the

strong influence of wettability on CHF, where increasing wettability (lower static contact angle) acts to increase CHF. The increase in CHF in the current results, as they were in Kwark et al. [32], can be ascribed to better rewetting of the evaporating microlayer and the accompanying reduction of the dry-spot in nucleating bubbles.

Returning to Fig. 2.10, it is seen that boiling heat transfer performances of the aluminum oxide and plain silicon surfaces gradually diverge, with the aluminum oxide surface yielding increasingly better BHT coefficients with increasing heat flux. For the hydrophobic Teflon surface, the BHT coefficients drastically degrade and a CHF of only ~13 W/cm^2 is soon reached. Figure 2.12 amplifies the low heat flux range (0-5 W/cm^2) of the same pool boiling curves.

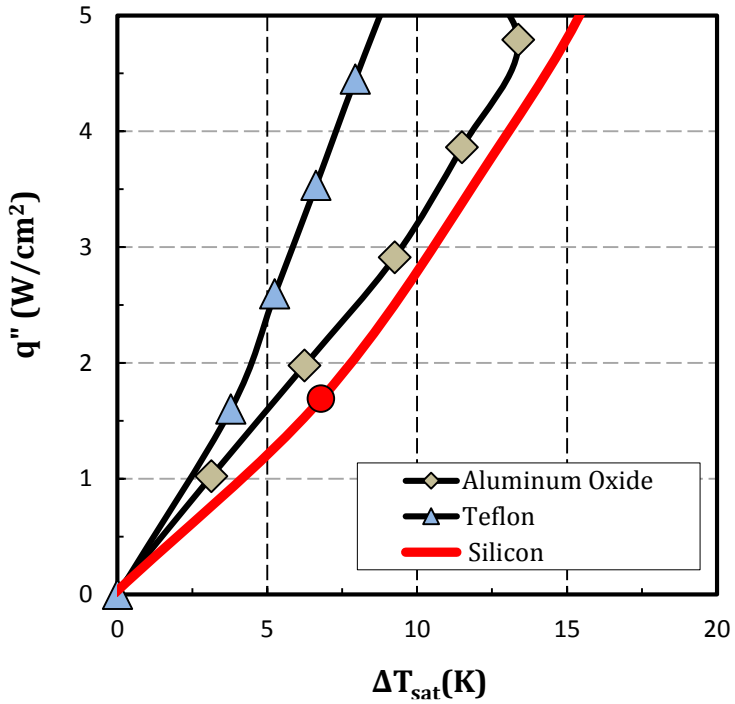

Figure 2-12 Low Heat Flux Portion of Pool Boiling Curves for Test Surfaces with Different Wettability

It can be observed in this figure however, that Teflon demonstrates the best BHT at this lower range of heat fluxes, reducing surface superheats by up to ~5^{o}C relative to the other two surfaces. This can be explained by early incipience of nucleate boiling over Teflon. During the tests, it was observed that in the 0-5W/cm^2 range, nucleate boiling on Teflon seemed to start immediately upon applying heating power, while on the other two surfaces only intermittent nucleation was observed in this range. This intermittent nucleation could give rise to the difference in superheats in Fig. 2.12 between these two surfaces (aluminum oxide and silicon). At 5W/cm^2 and above, where the two wetting surfaces were observed to be in full nucleate boiling regime, their heat transfer performances become even more differentiated as shown in Fig. 2.10.

For Teflon surface, with growing heat flux, the bubbles start to merge creating a vapor blanket which is responsible for surface temperature increment as heat flux exceeds 5 W/cm^2. Figure 13 illustrates the bubble merger on Teflon surface at heat flux of 2 W/cm^2.

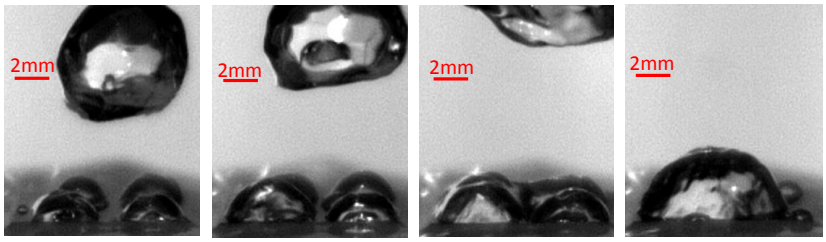

Figure 2-13 Bubble Merger into a Vapor Blanket on Teflon Surface at *2* W/cm^2

Initially, there were nearly four nucleating bubbles as shown by image at 4.50 ms. As time progressed, these bubbles merged to form a bigger bubble as shown by image at 25 ms. At 41.25 ms, the vapor completely engulfed the heated surface. The total resident time for the larger bubble formed by merger of four smaller bubbles was 110.75 ms before departure. This was nearly 75% of the total growth period. The resident time of larger bubble or vapor blanket increased with the heat flux until CHF.

As the heat flux grows the boiling curve of the aluminum oxide surface moves to the left of the plain surface. This signifies a better boiling heat transfer coefficient of highly wettable aluminum oxide surface. Figure 2.14 quantifies the heat transfer coefficient at various heat flux levels. The maximum heat transfer coefficient attained by plain and aluminum oxide surfaces are ~20 kW/m^{2}K and ~36 kW/m^{2}K respectively. At 648 kW/m^2, where plain silicon yields the maximum BHT, aluminum oxide reached 28 kW/m^{2}K which is a 40% enhancement in BHT.

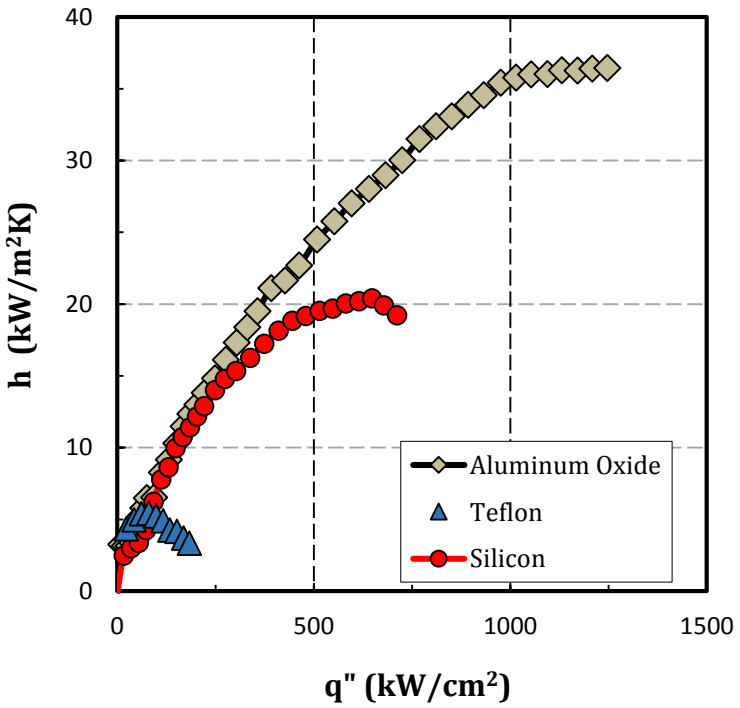

Figure 2-14 Comparison of Boiling Heat Transfer Coefficient (BHT) of All Surfaces

2.3.1.1 Bubble Emission Frequency

Bubble departure frequency, bubble diameter and their distribution on heated surface are primarily responsible for rate of heat transfer in nucleate boiling. Bubble emission frequency depends collectively on the time taken by the fluid adjacent to the

heated surface to develop thermal boundary layer through transient conduction, and total time for growth and departure of the bubble. The departure frequency (f_d) is given by:

$$f_d = \frac{1}{t_{cycle}} = \frac{1}{t_w + t_d} \tag{2.14}$$

Where, t_w is the wating period and t_d is the remaining time until bubble departs. Once the bubble departs the thermal boundary layer is reestablished during the waiting period.

Bubble departure frequency in the present study is obtained by high speed visualization for all surfaces. Figure 2.15 reveals the effect of wettability on the duration of the ebullition cycle.

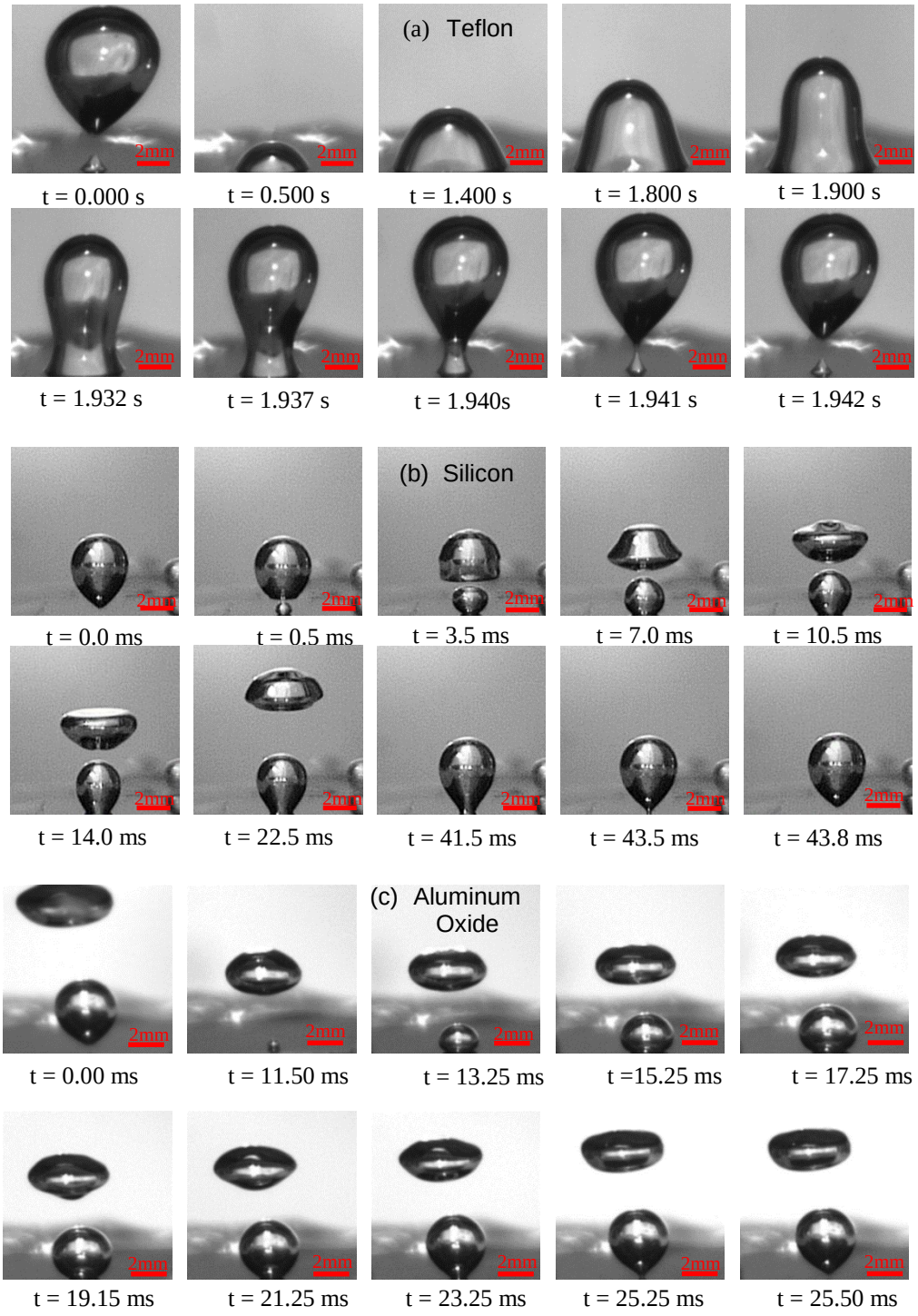

Figure 2-15 Single Bubble during One Ebullition Cycle of (a) Teflon, (b) Plain Silicon and (c) Aluminum Oxide Surfaces

The last two images shown for each test surface pin-point or bracket the end of the cycle on each test surface. From the time-stamps of Figs. 2.15 (a), (b) and (c), cycle durations are 1.942 sec, 43.8 ms, and 25.25 ms, for the Teflon, silicon and aluminum oxide test surfaces, respectively. The period over Teflon (Fig. 2.15(a)) is 44 and 76 times longer than the periods over plain silicon and aluminum oxide test surfaces, respectively. The longer duration could be due in part to the relative value of the net surface tension force on a hydrophobic surface, acting parallel to the surface at the triple-contact line. The high contact angle results directly from this force balance [25]. On Teflon, the high contact angle means that the bubble is shaped initially as a hemisphere (Fig.2.15 (a), t= 0.500, 1.400 sec). That is, the shape has a relatively large base (solid-vapor interface) on the substrate. As the bubble continues to grow and to stretch upward due to buoyancy, in order to maintain the high contact angle, an inflection develops (Fig. 2.15(a), t=1.800 sec) and the liquid/vapor interface becomes concave towards the bottom. As growth and stretching continues, as a consequence of the high contact angle, the diameter at the plane of the concavity is reduced into the cut-off and departure point of the bubble, the small vapor volume is left behind on the surface (Fig. 2.15(a), t=1.942 sec), and the cycle ends. Nam et al. [33] and Jo et al. [34] have also reported similar behavior on hydrophobic surfaces. The cycle over Teflon is lengthened because of the larger initial base, and the longer time thus required to reduce the base, and to reduce the plane above of the concave region into the cutting-off point of the bubble. On the other hand, on the two wetting surfaces (Fig. 2.15(b) and (c)), the contact angles below 90^{o} dictate a sphere-like shape throughout the whole cycle. This also dictates that the bases (microlayers and dry-spots) are small, and that bubble detachment takes place at the bases, as the images show. Due to the smaller

starting base, as the vapor moves upward due to buoyancy, reduction of the base into the cut-off point of the bubble requires much less time, thereby shortening the ebullition cycle.

In Fig.2.15 (b) and (c), the waiting period for hydrophilic (silicon) and highly hydrophilic (aluminum oxide) surface is notable. The waiting period is defined as the time that elapses between the departure of a bubble and incipience of a new bubble. The waiting period is prolonged by 11ms in case of aluminum oxide surface as compared to plain silicon which has a waiting period of just 0.5 ms. This huge difference caused by variation in wettability can be explained with the aid of an idealized conical cavity as shown in Fig. 2.16.

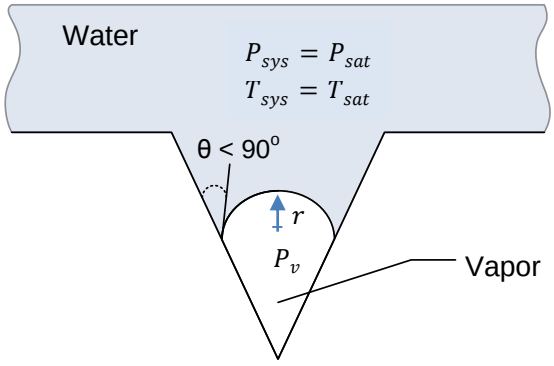

Figure 2-16 An Idealized Conical Cavity for Surfaces with Contact Angle Smaller than 90°

The pressure difference across the interface of the embryonic bubble resting inside the cavity is given by:

$$P_v - P_{sys} = \frac{2\sigma}{r} \tag{2.15}$$

The vapour pressure, P_v, is assumed to be the saturation pressure of the liquid at the surface temperature and the system pressure, P_{sys}, is saturation pressure of the liquid at the bulk temperature. And, r is the radius of entrapped embryonic bubble. Clausius-

Clapeyron equation relates this pressure difference across the interface to the temperature difference which is given by:

$$\left(\frac{dP}{dT}\right)_{sat} = \frac{h_{fg}}{T_{sat}\nu_{lv}} \tag{2.16}$$

Using equation 2.15 and 2.16, the wall superheat required for the incipience of a bubble can be expressed as:

$$\Delta T_{sat} = \frac{2\sigma T_{sat}\nu_{lv}}{h_{lv}r} \tag{2.17}$$

All the liquid properties in equation 2.17 are constant except embryonic bubble radius which is inversely proportional to the superheat required to initiate the nucleation [25].

In Fig. 2.16, the angle θ between liquid-vapor and liquid-solid interface inside the cavity is a function of surface energy. A larger angle provides better chance of trapping vapor inside the cavity. This trapped gas facilitates the initial nucleation. With the applied heat flux, the initial vaporization may occur on the liquid-vapor interface of this entrapped gas. The contact angle at the triple line inside the cavity as shown in Fig.2.16, diminishes with increasing wettability which also means a decrease in embryonic radius, r. Now, with this dependency of embryonic radius on wettability and equation 2.17, it is plausible to state that the wall superheat required for the incipience is higher for the surfaces with lower contact angle, that is, for the more wettable surfaces. This increase in required superheat is responsible for the prolonged waiting period for highly hydrophilic surface, although the total growth period was smaller.

Bubble emission frequency with corresponding contact angle is tabulated in Table 2-2. Highly wettable aluminium oxide surface nucleates bubbles that are comparable in

size with those of the plain surface. However, the frequency with which the bubble departs from the aluminium oxide surface is ~1.7 times that of plain silicon surface.

Table 2-2 Comparison of Bubble Emission Frequency

Surface	Contact Angle (θ)	Frequency (Hz)
Aluminum-oxide	13	39.22
Plain Silicon	57	22.83
Teflon	108	0.51

The volume of bubble departing from the boiling surface is also important in conjunction with the bubble emission frequency to dictate the heated surface temperature. Since the bubbles are not spherical, volume is not a function of diameter alone. For this study, the frontal areas are compared to differentiate the rate at which the vapor is releasing from the surface. The frontal area is calculated by image processing in Matlab. The growth of frontal area with time in plain and aluminium oxide surface is shown in Fig. 2.17. Both surfaces show faster initial growth which is also called inertia controlled growth. When the bubble emerges out of the cavity, a sudden change in bubble radius triggers the rapid expansion in bubble size [25]. The growth rate is higher in aluminium oxide (highly hydrophilic) surface than plain silicon (hydrophilic) surface. As time advances the growth rate decreases for both surfaces, indicated by change in slope (Fig. 2.17). This phase of growth is also called heat transfer controlled growth. Aluminium oxide surface goes through a shorter heat transfer controlled growth. The last point for each surface coincides with the bubble departure. A new bubble cycle initiates from this point.

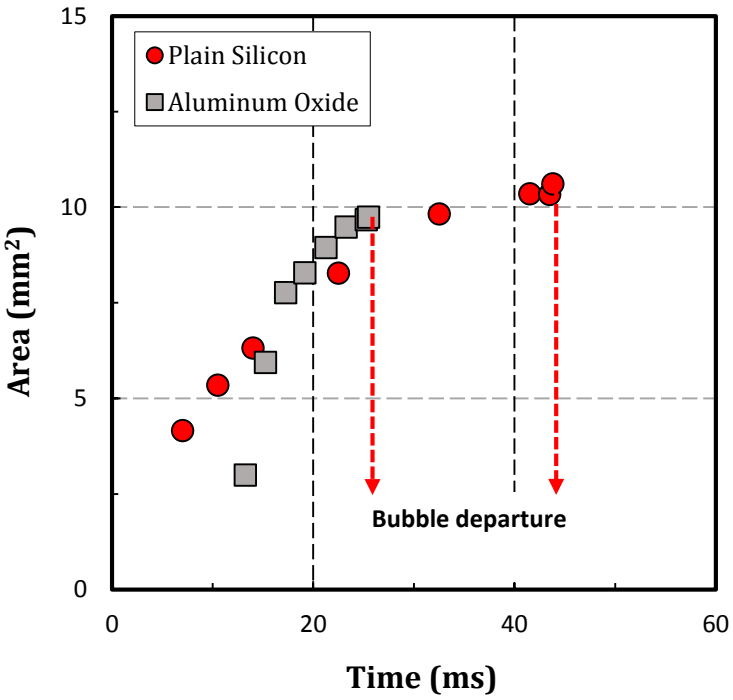

Figure 2-17 Frontal Area Growth Rate of Bubble

2.3.1.2 Bubble Base and Height

The growth of bases and heights of the bubbles in Fig. 2.15 were measured using the video analysis software of the high-speed video system, and are compared in Fig. 2.18. The measured growth pattern on each surface is unique, with Teflon (triangles) differing mainly in its much larger scale and slower timing. The inertia-controlled and heat-transfer-controlled growth phases of the ebullition cycle appear identifiable on plain silicon (circles). Judging from the growth pattern of the base, the two phases are demarcated by the abrupt shift in slope seen at ~0.006 sec, from positive, or enlarging base, to horizontal, or constant base. The growth during the first ~0.006 sec would correspond to inertia-controlled, and beyond, to heat-transfer-controlled growth. The later shift in slope seen at ~0.038 sec, from horizontal to negative and nearly vertical, indicating shifting to a fast-shrinking base,

corresponds to the approach to bubble departure from the surface. See images starting with t = 41.5 ms, Fig. 2.15(b). Over aluminum oxide (rhomboids, Fig. 2.18(a)), there also appears to be an initial inertia-controlled phase, which lasts up to ~0.004 sec, followed by heat-transfer-controlled growth blending with shrinkage of the base, as the bubble approaches the moment of departure. By roughly curve-fitting the data of Fig. 2.18(a), rates of initial or inertia-controlled base growth are demonstrated to decrease with increase in contact angle. The base of the bubble on the aluminum oxide surface ($\theta = 13^o$) grows the fastest, at ~519 mm/s, followed by the base on plain silicon ($\theta = 57^o$) at ~176 mm/s, and the base grows dramatically much slower on Teflon ($\theta = 108^o$), at ~5 mm/s. By curve-fitting the height data of Fig. 2.18(b), initial growth rates of bubble heights are seen to follow the same trend with respect to wettability. They are ~641 mm/s, ~293 mm/s and ~2.4 mm/s for aluminum oxide, silicon and Teflon surfaces, respectively. (The rates for Teflon were obtained over the range of 0 to 1 second.) This growth trend with wettability could reflect the availability of microlayer evaporation under each bubble. On the more wettable surface, such as on the aluminum oxide surface, the microlayer is thinner and more extensive under a given bubble volume, therefore, the rate of microlayer evaporation is higher, causing the bubble to grow faster as observed in Figs. 2.15 and 2.18. Given heat fluxes are dissipated at lower superheats on the more wettable surfaces due to thinner and more extensive microlayers. This could explain why BHT over the more wettable aluminum oxide is better than on the less wettable silicon for the whole range of pool boiling as seen in Fig.2.14.

(a)

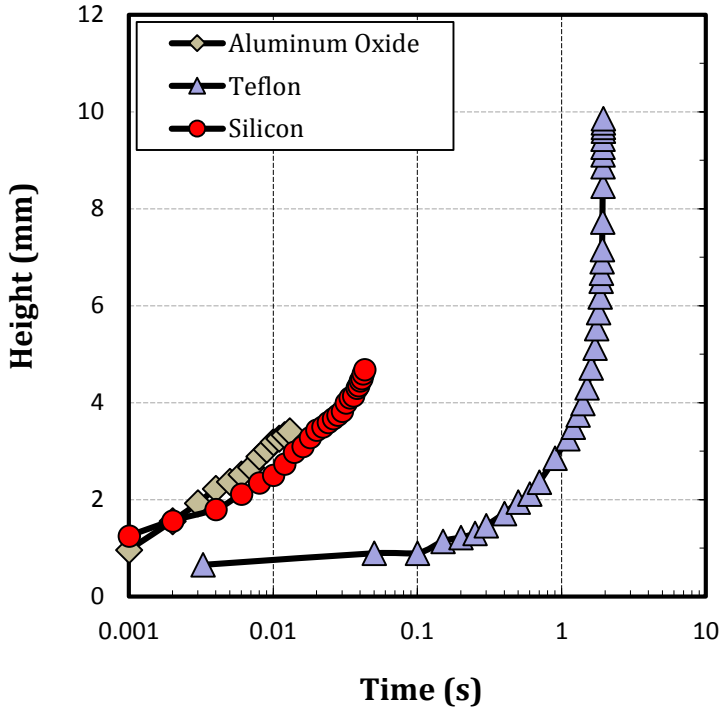

(b)

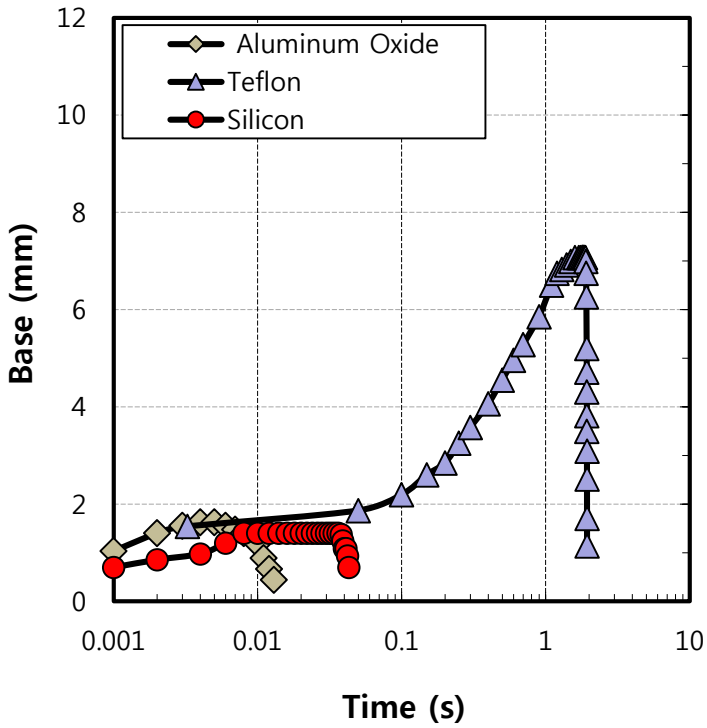

Figure 2-18 Growth with Time of Bubble's (a) Base and (b) Height on the Three Test Surfaces

2.3.2 Effects of Surface Orientation

Effects of surface orientation on pool boiling heat transfer have been long investigated. The results from these studies clearly indicate the influence of orientation on CHF. Howard and Mudawar [35] conducted saturated pool boiling experiments and flow visualization at various orientations to understand its effect on CHF. From visualization at different orientations, they reported the vertical liftoff of the bubble by buoyancy in upward orientation (0-60^o), wavy liquid vapor interface at near vertical region (60-165^o) and repeated stratification of the vapor on downward facing surface (>165^o). They suggested that separate CHF modeling in these three different regions to be more meaningful than an overall single CHF model that accounts for all the orientation.

In the present study, aggregate effect of inclination and wettability on CHF has been investigated experimentally on the three test surfaces studied so far, plain, Teflon and aluminum oxide coated surfaces. All the tests are conducted in saturated and degassed condition at atmospheric pressure. The test results are shown in Fig.2.19, Fig. 2.20 and Fig. 2.21 which correspond to the surfaces with static contact angle of 13 ^{o} (aluminum oxide), 57^o (plain silicon), and 108^o (Teflon) respectively.

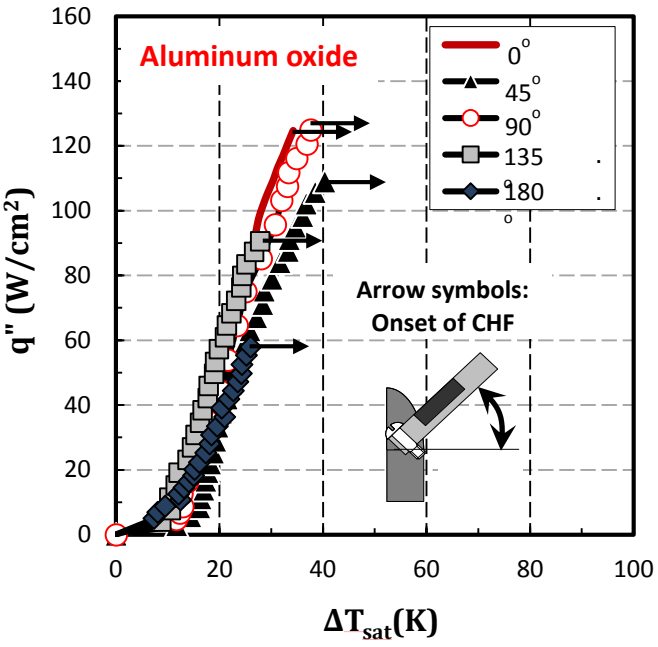

Figure 2-19 Effects of Orientation on Highly Hydrophilic

(Aluminum Oxide) surface

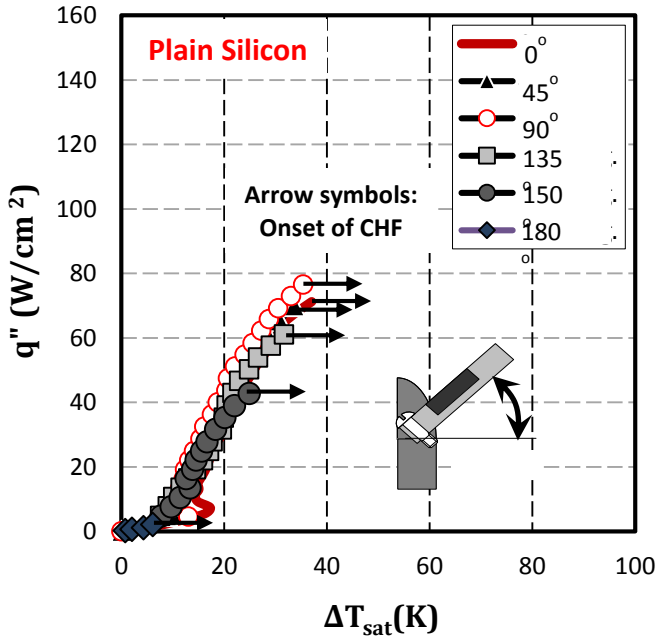

Figure 2-20 Effects of Orientation on Hydrophilic (Plain Silicon)

Surface

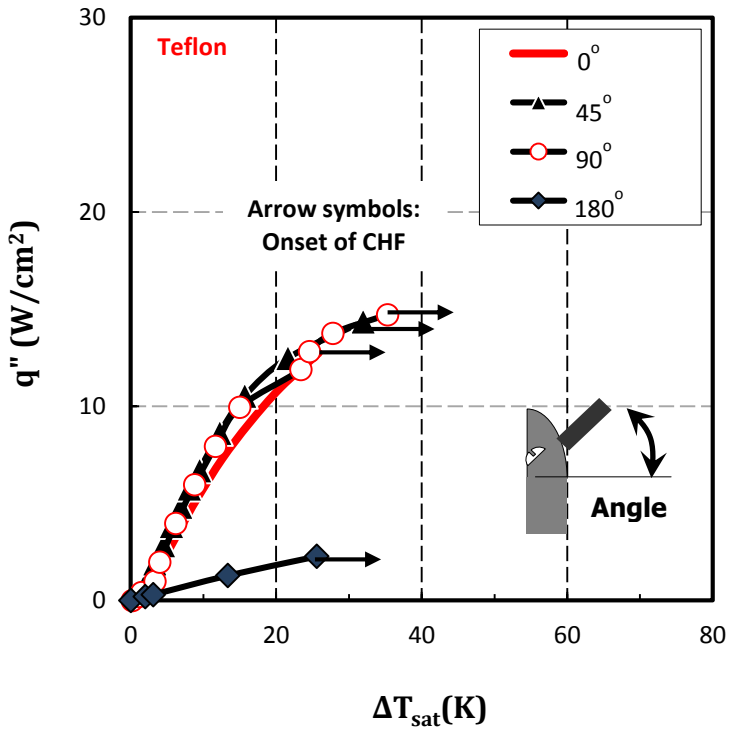

Figure 2-21 Effects of Orientation on Hydrophobic (Teflon) Surface

Effect of orientation on CHF was found to be marginal up to 90 ^{o} orientation in all cases. The escape route for the bubble is not obstructed by the substrate up to this orientation. A sliding of bubbles rather than departure was observed. A continuous degradation of CHF occurred upon exceeding the inclination thereafter.

CHF of surfaces with different wettability respond similarly to change in inclination shown in Fig.2.22. CHF degradation at orientation of 180^{o} is noticeable. Longer vapor residence at this orientation is responsible for the severe decline in CHF. Bubble does not depart from the surface; instead, they accumulate, grow and coalesce until it reaches to the boundary of the mounted heater. Thus accumulated bubbles prevent the liquid supply to the microlayer for evaporation. Hence, it is believed that dry spot on the heated surface is remarkably large which triggers the surface temperature beyond the set criterion of CHF.

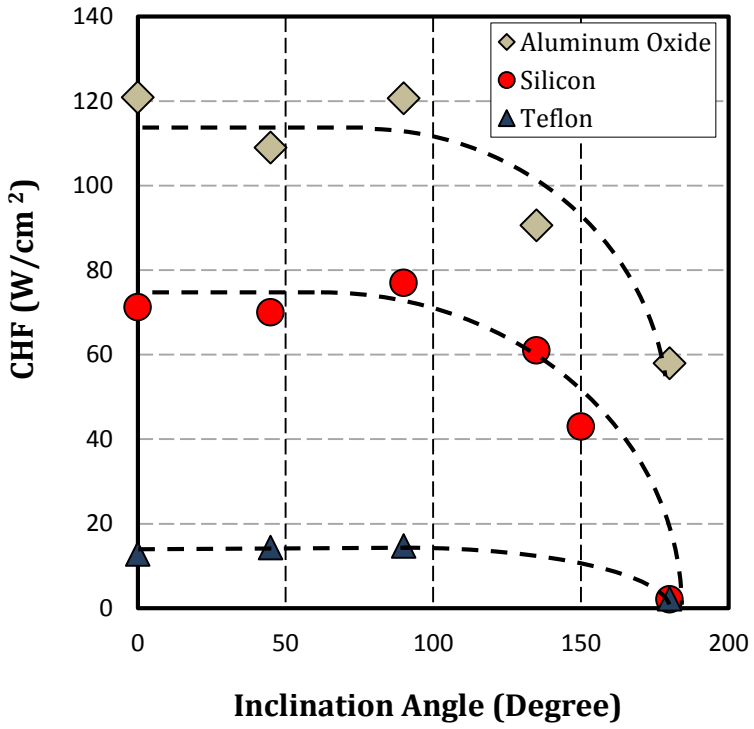

Figure 2-22 Comparison of Effect of Inclination on all Tested Surfaces

In case of plain silicon and Teflon coated surface a very early arrival of CHF was observed for the 180^{o} orientation. However, aluminum oxide, which is highly hydrophilic in nature shows relatively smaller CHF degradation as compared to other two surfaces. The net degradation in CHF as compared to horizontal surface for plain silicon, Teflon and aluminum oxide surfaces are 98, 82 and 51% respectively. Again, the highly hydrophilic nature of aluminum oxide surface replenishes the microlayer region of the accumulated bubbles to considerably higher heat fluxes compared to other surfaces which naturally delays CHF.

Chapter 3

Thermal Management of a Hot-Spot by Pulsed Jet Impingement on a Superhydrophilic Nanoporous Coating (SHNC)

Advances in semiconductor technology have allowed the continuous growth in number of transistors per chip as described by Moore's law. The circuits are becoming faster and smaller in feature size providing better computing power. The rapid evolution of integrated circuit design has surfaced the issues of increased power dissipation, leakage power, interconnect resistance and non-uniformity in heat distribution, spatially and temporally, ascended from higher levels of device integration. With this trend, hot spots have become more prevalent. Thermal management of thus formed hot spots has become a primary concern to operate the system without degrading performance and reliability. Without the adaptation of a highly efficient cooling scheme, the issue of thermal management will linger and become even more pronounced as the transistor density will continue to grow with the advent of new high resolution photolithography technique in the future.

Conventionally used air cooling scheme is not a viable cooling option primarily at elevated heat flux due to its fundamental limitations on cooling performance. The bottleneck in conventional air cooling scheme is the thermal transport from chip to heat spreader through one or multiple thermal interfaces. Extensive research intended for eliminating microscopic air pockets in thermal interface has brought various exotic thermal interface materials to light. This has resulted in noticeable improvement in air cooling. However, it still remains inefficient for managing high power dissipation triggered by continuous trend of shrinking feature size and increasing transistor density. Aerodynamic efficiency of fan also plays equally significant role. And the use of fan at higher speed could be useful to increase the performance of air cooling, however, the tradeoff with excessive

electrical power consumption and the increased noise level becomes critical. Liquid cooling particularly by phase change could be a viable option to elevate the cooling performance far beyond the limits of air cooling. The cooling capacity of liquid cooling comes from the high latent heat of vaporization associated with the working fluid. Odhani et al. [36] has compared the efficiency of air, liquid and phase change cooling. They reported a thermal resistance reduction of 10.5 and 4 times by two-phase force-fed manifolded micro channel cooling than air and single phase liquid cooling respectively. They also reported the reduction of pumping power in microchannel flow boiling by 12.6 and 24.3 times that of air and single phase liquid cooling respectively. The reduction in pumping power compared to conventional flow boiling was attributed to the fact that the major mode of heat transfer was forced convection boiling and thin-film evaporation over high aspect ratio microchannels with limited fluid flow running length. Results of various experimental studies in phase change heat transfer have been reviewed by Agostini [37]. In this work various modes of heat transfer (single and two phase flow, jet impingement etc.), its benefits and drawbacks, has been discussed with recommendation of micro channel flow boiling as better cooling option due to low pumping power and high heat dissipation rate. However, this work does not include thin film evaporation as computer chip cooling technology. This could be a result of a limited work conducted in thin film evaporative cooling. Thin film evaporation has been studied mostly in a meniscus. Jiang et al. [38] conducted experiments on thin liquid film on a heated cylinder. They reported a maximum heat transfer coefficient corresponding to evaporating thin film region which was 2.5 to 3 times higher than the rest of the solid liquid surfaces. Höhmann and Stephen [39] used temperature sensitive liquid crystals to measure the temperature distribution underneath an evaporating meniscus and reported a local cooling due to high evaporation rate in the contact line region. Wang et al. [40] investigated the thin film region of an evaporating meniscus in a microchannel. They

reported that the micro region which extends from non-evaporating region to the region where the film thickness is 1 μm, is responsible for more than 50% of the total heat transfer. Dhavaleswarapu et al. [41] experimentally investigated heat transfer characteristics of the thin film region in a two dimensional meniscus and reported a distinct temperature drop at the triple line. The studies mentioned so far emphasize evaporation of meniscus. Limited work has been reported that utilizes thin film evaporation for thermal management of microelectronics. Hsieh et al. [42] performed evaporative spray cooling on micro structured silicon surface and reported four heat transfer regimes including flooded, thin film, partial dry-out and dry-out. In this study, start of liquid film breakup was held responsible for heat transfer coefficient deterioration at higher heat flux. Bond number which is a comparison between gravitational force and surface tension was identified to increase the liquid breakup heat flux. Kim et al. [43] performed evaporative spray cooling on plain and microporous coated surfaces. They found an enhancement up to 400% by evaporative cooling on microporous coated surface as compared to dry air cooling with uncoated plain surface. Capillary pumping of the coolant through the micro cavities in porous coating was described as the major contributing factor for this enhancement. Amon et al. [44] described the use of Microelectromechanical system to develop evaporative spray cooling device for package level cooling of high heat flux electronics. This work combines the use of micro structured surface and liquid jet atomization through micronozzles. A uniform heat flux removal of 45 W/cm^2 using mass flux of 33.2 g/cm^2 of HFE-7200 coolant was reported. Bar Cohen et al. [45] examined the advantages of gas assisted evaporative cooling of high density microelectronics. They used Helium or Nitrogen assisted flow of FC-72 through a channel and attained volumetric heat dissipation rate of 18 W/cm^3. Most recently Narayanan et al. [46] utilized perspiration nanopatch for thermal management of hot spots. In their experiments, the evaporating thin film was induced by capillary confinement of

coolant, and jet impingement of dry air on nanoporous membrane was used to facilitate evaporation.

The current study will investigate the localized cooling of a hot spot using phase change heat transfer, preferably thin film evaporation, which is capable of absorbing significant amount of heat from a heated surface compared to any known heat transfer mechanism. High heat transfer efficiency of evaporative cooling has been reported by various researchers [38] [39] [40] [41] as described earlier. Formation of thin liquid film is the foremost ingredient of effective evaporation. Its efficacy is a direct consequence of reduced thermal resistance across the thin film. The reduced thermal resistance of thin film brings the liquid vapor interface temperature closer to the substrate temperature immediately upon contact. This in turn results in faster evaporation of the thin film at the liquid vapor interface given that surface temperature is greater than saturation temperature of the coolant at system pressure. Hence, thinner liquid films leads to the faster evaporation which ultimately results in much reduced surface temperature. The overall effectiveness of evaporative cooling also depends on the coverage of heated surface by thin liquid film at all instances. Lack of on time liquid replenishment on heated surface will introduce dry zones resulting in elevated surface temperature. Premature replenishment will lead to thicker liquid layer increasing the thermal resistance. At the same time, coolant replenishment that is delayed for too long can increase the chip temperature beyond critical point. Hence, the effort in present study is to deliver smaller coolant droplets in proper frequency. Smaller droplet will result in thinner film upon contact with heated surface and faster delivery will diminish the formation of dry zones.

Conventional cooling schemes that rely on evaporation utilizes components like heat pipes and vapor chambers. In these components, the working environment is degassed, so the reduced working pressure can instigate phase change heat transfer at

relatively lower temperature. However, constructing such scenario for embedded microelectronic systems could be challenging in terms of providing hermetic seal to the degassed environment. Hence, any consequence of gassy environment needs to be addressed. In this regard, the current work systematically studies any influence of noncondensables on evaporative cooling of localized heat flux or hot spots. Narrow space available for vapor transport in embedded microelectronics can be of concern as well. The accumulated vapor can build pressure and degrade heat transfer coefficient. This space constraint was incorporated by tests conducted in a micro-gap at various conditions of pressure and system temperatures.

3.1 Experimental Apparatus and Procedure

3.1.1 Liquid Delivery System

A liquid delivery system was designed to generate liquid droplets precisely in nanoliter volumes. The schematic of liquid delivery system is illustrated in Fig 3.1. The setup consists of a cylindrical water reservoir made of stainless steel with a pressure rating of 500 psig. The minimum wall thickness of the cylinder is 2.4 mm. It can hold up to 300 ml of water which is pressurized using compressed air. An air filter is used to remove any particulates prior to entering the reservoir. The pressure inside the reservoir is continuously monitored by using an Omega PX 302 pressure transducer, which has a range of 0 to 50 psia. The reservoir is connected to a solenoid valve through transparent Teflon tubing. The solenoid valve is connected to a nozzle with internal and external diameters of 0.127 mm and 1.27 mm, respectively.

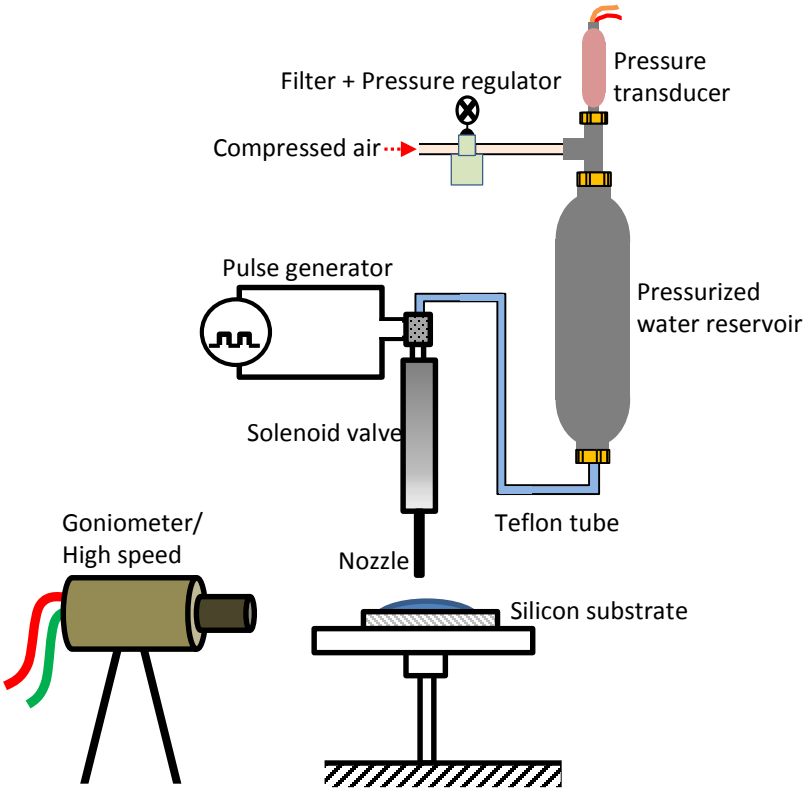

Figure 3-1 Liquid Delivery System

The solenoid valve actuates upon receiving a signal from a pulse generator. A square pulse of 5 volt was used which is illustrated in Fig. 3.2. Pulse duration (PD) is the valve on time. The separation between pulses dictates the frequency/period with which the droplets are dispensed. This system was calibrated to operate with distilled water as working fluid at pressure conditions ranging from 5 to 15 psi.

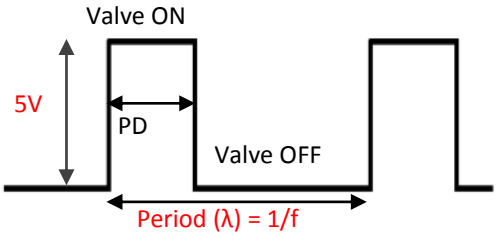

Figure 3-2 A Pulse Signal Used to Actuate Solenoid Valve

3.1.1.1 Droplet Characterization

The droplet dispensed from this system was characterized using images captured from a goniometer and high speed camera. A plain silicon surface was used as substrate. The distance between the nozzle and silicon substrate was maintained at ~ 0.5mm as shown in Fig. 3.3(a). The top view of the droplet is shown in Fig 3.3(b) which shows a near circular shape. This small deviation can add minor error to droplet volume calculated by goniometer.

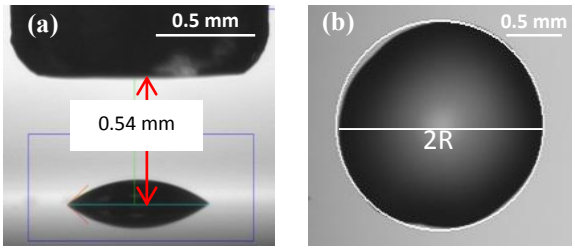

Figure 3-3 (a) Profile View of a Droplet Taken from Goniometer and (b) Top View Taken from Optical Microscope

Performance envelope of the liquid delivery system, its volume range and accuracy were measured. Average dispensed volumes at various air pressures and pulse durations are demonstrated in Fig.3.4. The error bars indicate two standard deviations for fifty repeated deliveries of the same nominal volume. During the measurement the liquid droplets were assured to be spherical caps. However, the snapshot of a droplet taken from top view using microscope demonstrates small deviation from perfect circular shape as shown in Figure 3.3(b).

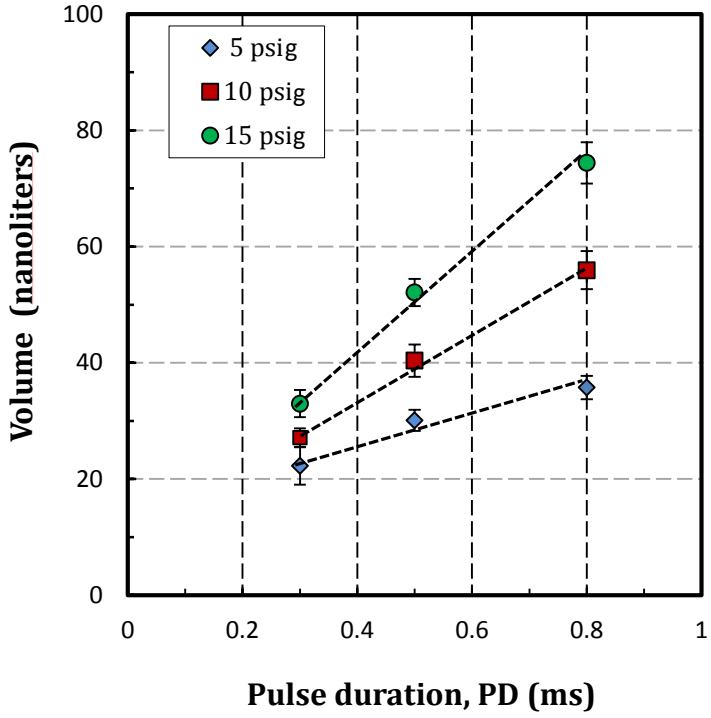

Figure 3-4 Average Volumes at Various Pressures and Pulse Durations

As Fig. 3.4 shows, the dispensed liquid volume was found to linearly increase with pressure and pulse duration. The increase in droplet volume with pressure and pulse duration is visually demonstrated in Fig. 3.5.

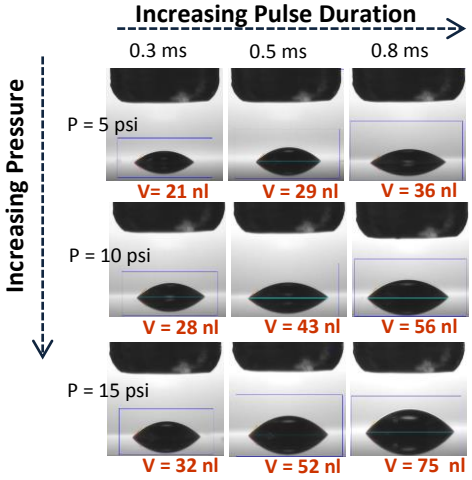

Figure 3-5 Images of Water Drops at Various Pressures and Pulse Durations

The droplet size increases from left to right (increasing pulse duration) and also increases from top to bottom (increasing pressure). All the images were captured using a goniometer.

3.1.1.2 Quality of Dispensing at Higher Frequency

Valve actuation time does not exactly match 5V pulse input time. Thus, at a sufficiently short period, but still larger than the selected PD, dispensing might no longer be discrete and dispensing could become nearly continuous which is not desirable. Hence, the valve was tested to determine a minimum period (max frequency) where adequate time gap, or air time, between doses still exists. For this purpose high speed video was taken at 58,000 frames per second. Results, as shown in Fig. 3.6, show no less than ~40% of period is air time or gap between liquid deliveries at the smallest period tested, 2 ms (f = 500 Hz). Therefore, discreteness of dispensing is still maintained at 500 Hz. The percentage air time is based on time of valve closed and cycle period as shown by:

$$\%\ air\ time = \frac{t_{valve\ closed}}{\lambda} \times 100 \tag{3.1}$$

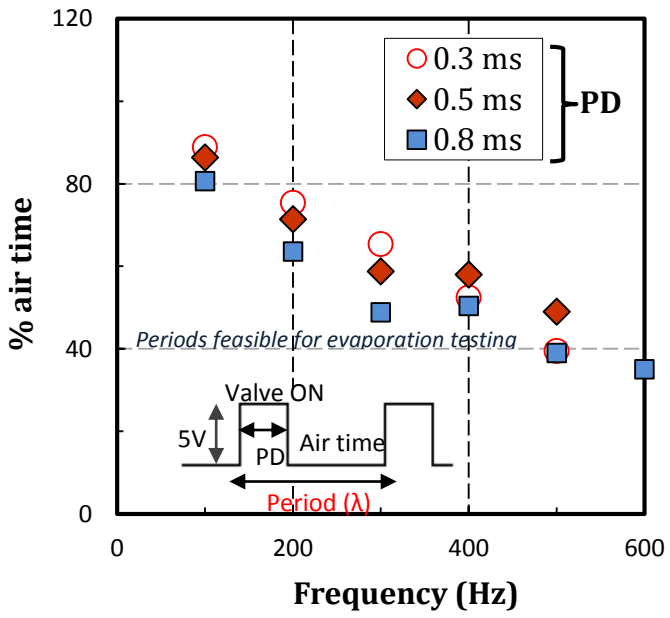

Figure 3-6 Discreetness of Liquid Deliveries at Higher Frequencies

The images captured from the high speed filming of water delivery at 600 Hz flow rate is shown in Fig 3.7. The first image is taken when water is about to come out of the nozzle and remnants of the previous water dose are within view. The following images are the snapshots at various time interval. The last image taken at 1.081 ms of delivery cycle demonstrates the end of the water delivery as indicated by the circle. The time that elapses from this point onwards until the appearance of another dose of water is called the air time as shown in equation 3.1.

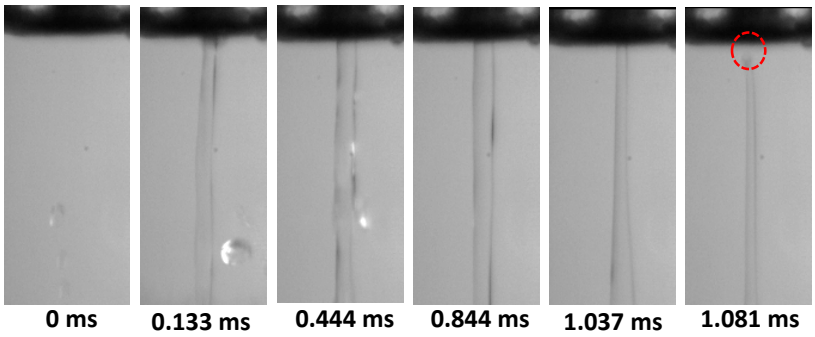

Figure 3-7 High Speed Images Taken During 600 Hz Water Delivery

3.1.2 Integration of Liquid Delivery System and Pressure Vessel

Tests were also conducted at various system temperatures and pressures to emulate the actual embedded thermal management system. A pressure vessel was integrated with the liquid delivery system. The schematic of the integrated system is shown in Fig. 3.8. The pressure vessel is made of stainless steel with the height and diameter of 406 mm and 154 mm respectively. Three cartridge heaters are installed at the bottom of the vessel to heat the water. There are five band heaters, two on each side and one at the bottom, externally attached to the vessel. There is also an internal water cooled condenser. Both the band and the cartridge heaters along with the internal condenser were used to control the desired system temperature. The test vessel was insulated with a 15 mm thick

foam insulation. Two T-type thermocouples were placed inside the chamber to measure the water and vapor temperature. The test vessel was also connected with compressed air to create various gassy and pressurized conditions. The pressurized air passes through an air filter to remove any particulates. The system pressure was monitored using an Omega PX 302 pressure transducer, which has a range of of 0 to 50 psia. There are two glass view ports to observe the water level and for high speed visualization.

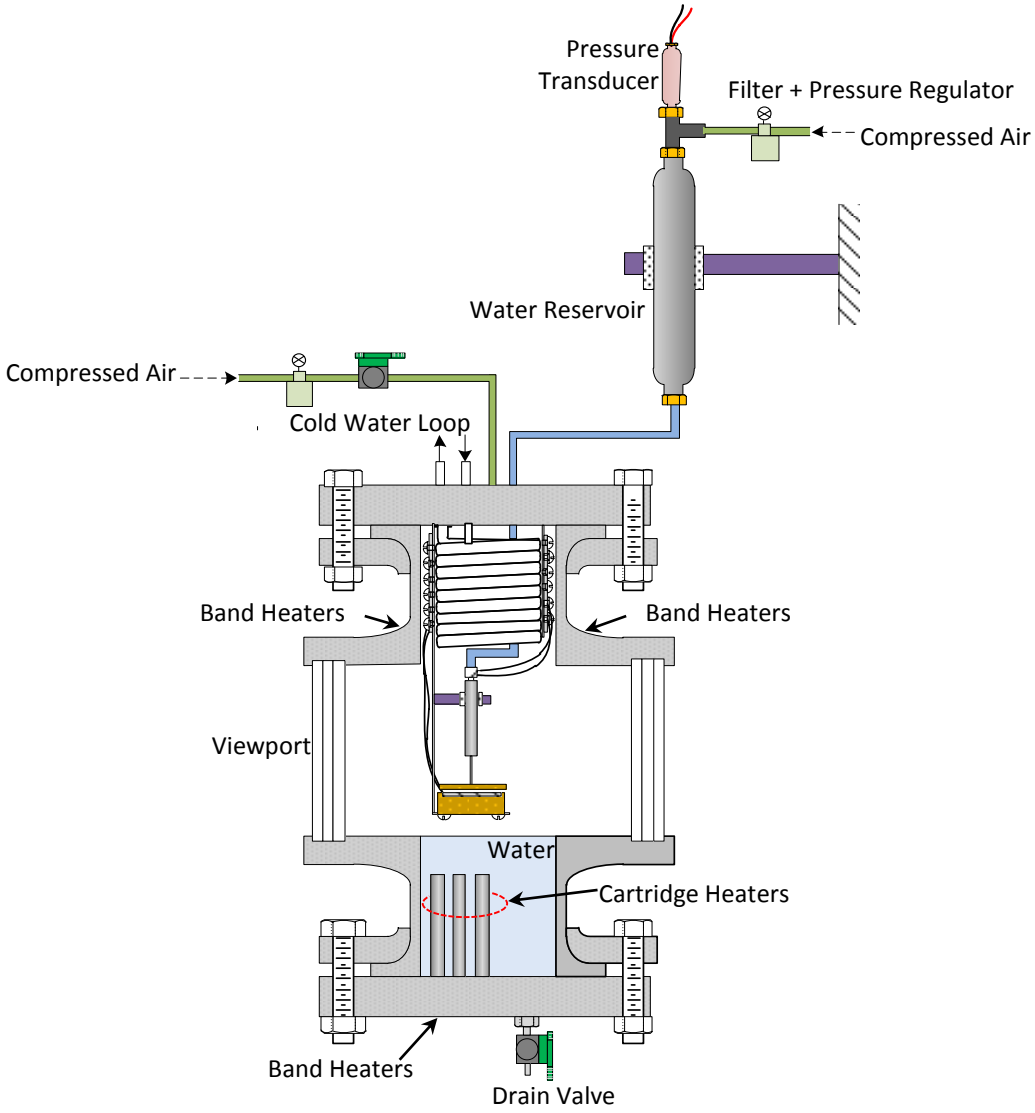

Figure 3-8 Integrated Liquid Delivery System and Pressure Vessel

3.1.3 Hot Spot/Temperature Sensor

A robust resistive layer of 2×2 mm^2 size was fabricated on a 10×10 mm^2 silicon substrate by using standard photolithography and liftoff process. The detailed design of the hotspot/temperature sensor is shown in Fig.3.9. There are several fabrication steps starting with a thorough cleaning of 4" silicon wafer in a Piranha solution (H_2SO_4:H_2O_2) for five minutes and rinsing in distilled deionized water. This is followed by the deposition of a thin silicon nitride film with thickness of ~0.5 µm using low pressure chemical vapor deposition (LPCVD). During this process ammonia and dichlorosilane were flown inside the deposition tube at 37 sccm and 13 sccm respectively.

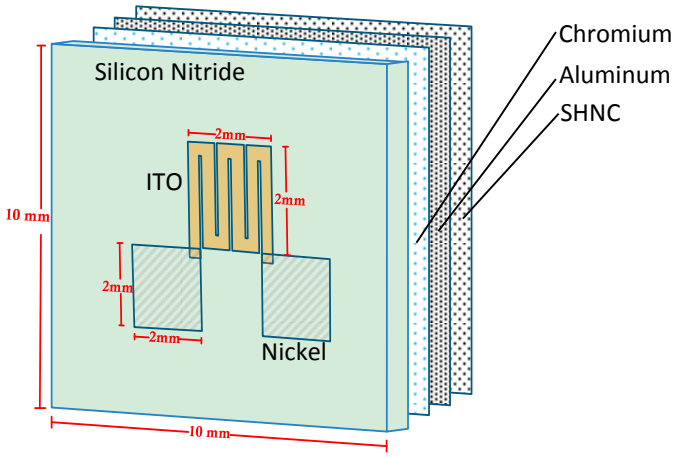

Figure 3-9 Resistive Layer/Temperature Sensor Design

The temperature was maintained at 770°C and pressure was kept below 200 mTorr. This method usually provides excellent uniformity of film thickness across the wafer. The deposited silicon nitride film serves as a passivation layer. A thin layer of positive photoresist (S1813) was spin-coated on the silicon nitride surface at the rate of 4000 RPM for 30 seconds which results in ~1.2 µm thick coating. This layer was soft baked at 110°C prior to the UV exposure through photomask. The UV light controller was set to a constant intensity of 20 milliWatt/cm^2 and the exposure lasted for 7 seconds in order to obtain a

required dose. The wafer was then baked at 90°C and developed in positive resist developer (MF319) for 40 seconds followed by rinsing in distilled deionized water. All the soft baking steps were carried out on a hot plate. At the end of these fabrication steps, the desired pattern was transferred from the photomask to the substrate. A thin layer of Indium Tin Oxide (ITO) with thickness of ~8000 °A was deposited at 120 Watts using ITO (In_2O_3/SnO_2, 90/10 wt%) sputtering target. This process was conducted in an Argon environment at a pressure of 3 mTorr. The substrate holder was rotated at 50 Hz during the deposition in order to achieve uniformity in thickness. Liftoff of the resist was carried out in a positive resist remover (Microposit remover 1165) bath heated at 80°C. After lifting off the resist, the pattern of ITO resistive layer that serves as hot spot and temperature sensor as well, was obtained. A nickel buss of 2×2 mm^2 size was fabricated to provide electrical connection for power supply. Nickel was deposited using E-beam evaporation at a rate of 0.5°A/s. Deposition was carried out at a base pressure of ~2×10^{-4} mTorr.

3.1.4 Heater Assembly

The test surfaces were set up for thermal testing in two ways. In the first case the silicon substrate was open to the ambient and in the second case a cover was placed over the silicon substrate which creates a micro-gap with the surface. Furthermore the micro gap case was also tested at various conditions of temperature and pressure inside the vessel shown in Fig.2.8. The detailed design of the heater is explained in the following sections.

3.1.4.1 Open Design

The fabricated heater was connected to the power supply using a copper wire. The wired heater was then mated to a Lexan plate for mounting and insulation, and was surrounded with epoxy to fix it in place, leaving the test surface exposed and flush with the epoxy level. A schematic of the prepared heater is shown in Fig. 3.10. There are three

pathways for excess cooling liquid removal during thermal testing. Two of them were outside of the chip area of 10×10 mm2 for the excess water that spreads out due to high mass flow rate. And the third was to remove the water that condensed on the surface of the nozzle. All the excess liquid was drained using a vacuum pump.

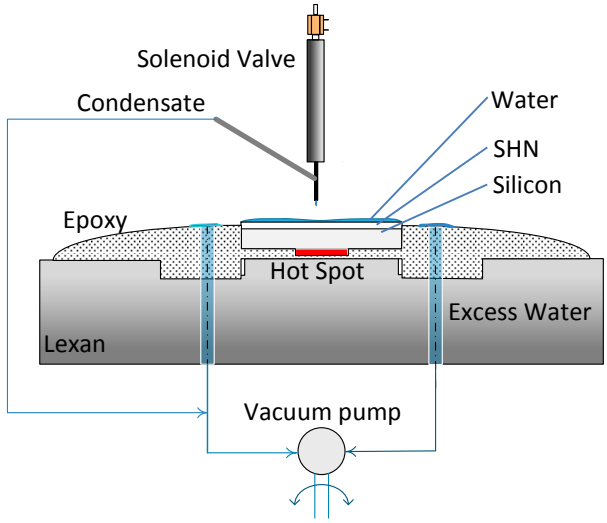

Figure 3-10 Assembled test Heater for Open Testing

3.1.4.2 Micro-Gap Design

The micro-gap design includes device similar to open testing as shown in Fig. 3.10, but sandwiched between two Lexan plates. The detailed design of the micro-gap is shown in Fig.3.11. The thickness of top cover Lexan plate is crucial as Lexan has a tendency to bend or deform at elevated temperature. In the current test, a heat flux is held until steady state is reached. Hence, the inner side of the top cover plate may have to sustain vigorous evaporation, particularly at higher heat flux, for extended period of time. This could deform a thinner piece of Lexan and alter the gap size between the top cover and the test sample during the test. Hence, a thick Lexan plate with thickness of ~5.5 mm was used in order to preserve a constant gap size throughout the testing. The width of the plate (10 mm) matches the footprint of the silicon substrate. The two sides of the micro-gap where the top

cover plate mates with the bottom substrate are sealed with epoxy. The remaining two sides are left open for excess water and vapor removal. The vacuum pump, as done in open cases (Fig.3.10), cannot be used in enclosed testing. The pressure built inside 0.5mm gap between silicon surface and the top cover plate rejects the excess water/vapor. The nozzle is inserted through the top cover directly above the center of the hot spot. Structural stability of thus attached nozzle needed to be insured because the momentum of droplet exiting the nozzle may detach the delivery system or increase the distance between nozzle and substrate during the test. Hence, a hole of ~1.27 mm diameter was drilled at the center of top cover plate to provide a pressure fit for the nozzle. Thus inserted nozzle was furthermore sealed with silicon sealant around the nozzle to prevent any outflow of water/vapor and also to provide more stability. Outlet of the nozzle is leveled with the inner surface of top cover plate so that the nozzle to chip separation is ~0.5 mm.

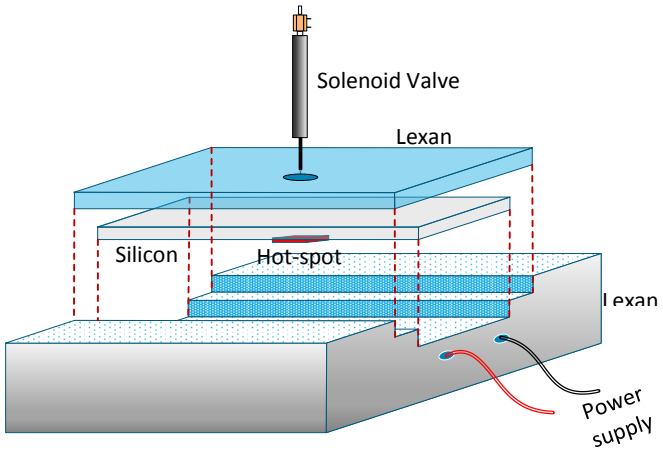

Figure 3-11 Assembled Heater for Micro-Gap Testing

3.1.5 Resistance Temperature Detector (RTD) Calibration

The purpose of RTD calibration is to determine the electrical resistance of ITO film as a function of temperature. This temperature-resistance relation obtained from the calibration converts the measured resistance value into temperature at various heat fluxes

during the test. Calibration was carried out in a convective oven and in a water bath separately and compared. Results are shown in Fig 3.12. For water bath, hot plate with magnetic stirrer were used to uniformly heat the fluid at various temperatures, and the respective resistance values were recorded. During the calibration, temperatures at the top, middle and bottom of the bath were continuously monitored using t- type thermocouple.

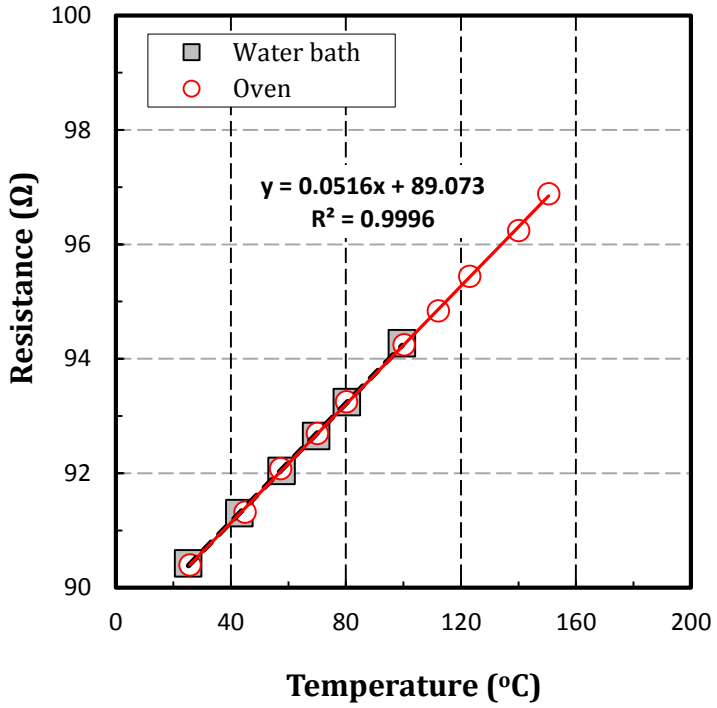

Figure 3-12 Temperature Calibration for 2 x 2 mm^2 ITO Heater

The resistance reading was taken using four-wire method only upon reaching a desired steady state value of temperature. Four wire circuitry is shown in Fig. 2.9. The significance of using four-wire measurement is that it provides more accuracy in measuring the voltage drop across the resistor than two wire measurement where the measured voltage drop also includes the wire resistance. In four-wire measurement, current is supplied to the resistor through one set of wires and the voltage drop across the resistor is measured at the same

point through a different set of wires. Hence, the voltage sensed by the data acquisition system (DAQ) is the same as voltage across the resistor due to the fact that the sensing wires connected to the DAQ carry miniscule current. It is recommended to connect the sensing wire as close to the resistor as possible to completely eliminate the addition of wire resistance to the reading. Results shown in Fig. 3.12 shows resistance versus temperature curves that are similar for both calibrations conducted in water bath and convective oven. And the temperature dependency of resistance was found to be very linear in both cases.

3.1.6 Experimental Procedure

Prior to starting the tests, the reservoir was filled with distilled water and pressurized using compressed air. The pressure inside the reservoir was monitored using a pressure transducer. The liquid delivery system was turned on at 500 Hz for ~1 minute in order to remove any trapped air inside the tubing between reservoir and the solenoid valve. This made the liquid delivery system ready to dispense the desired mass flow rate.

A LabVIEW program controlled the power supply to the test heater and the data acquisition system. To start the test, the liquid delivery was initiated and heating power was applied to the test heater. The temperature from the ITO temperature sensor was monitored every half second for 50 seconds, the values were averaged, and the process was repeated for the next 50 seconds. If the difference between consecutive averages was below 0.3^{o}C, steady-state was assumed, and the temperature and applied heating power were recorded. Heating power was then incremented to the next programmed level, and temperatures and power were again recorded upon reaching the new steady-state. The temperature measurement was obtained by using four wire method. The power increment and the respective steady-state temperature measurement continued until the dryout was reached. The program assumed that the dryout condition was reached when the temperature of the heater exceeded the previously recorded steady-state temperature by

more than 40°C. The power to the heater was then shut down and all data including temperatures and power were saved.

3.2 Superhydrophilic Nanoporous Coating (SHNC) Fabrication

Fabrication of a surface with exceptionally high affinity to water is essential for thin film evaporation. This property of the surface can transform liquid droplet into thin film immediately upon contact which results in reduced thermal resistance of evaporation. Therefore, an attempt was made to fabricate a surface with superior wettability or superhydrophilicity. Static contact angles were measured to quantify wettability of such surfaces. Any surface with the contact angle in the proximity of 0^o was declared as superhydrophilic. Work required to spread liquid on unit area of superhydrophilic surface is almost negligible as compared to hydrophilic and hydrophobic surfaces. This is also known as work of liquid spreading or spreading coefficient given by:

$$W_s = \gamma_l(cos\theta - 1) \tag{3.2}$$

Spreading coefficient, W_s, is a measure of liquid's tendency to wet and spread into a thin film. A variety of work has been reported in regards to induction of superhydrophilicity. Takata et al [47] fabricated a photo induced superhydrophilic surface for pool boiling test. This work also reports the loss of wettability upon deprivation of light. Nam et al [48] fabricated superhydrophilic surface by generating needle shaped copper oxide nanostructures on copper microposts using electrochemical deposition and chemical oxidation technique. Chen et al [49] induced superhydrophilicity by nanowire arrays made of Si and Cu by electroless etching technique. Kwark et al [50] fabricated nanoporous coating by boiling a copper substrate in ethanol based nanofluid. These works were successful in enhancing the surface wettability, however, they do not elaborate on the bonding strength of the nanowires or nanoparticles to the substrate which is equally

important to wetting. Most of these surfaces were tested in pool boiling tests where the stagnant pool of water does not offer any turbulence to test the integrity of the coating. However, the present study demands the superhydrophilic coating to adhere well with the substrate and endure the droplet impact during cooling water delivery. Hence, the strength of superhydrophilic coating is equally essential and will be addressed in this study.

3.2.1 Coating Method

Alumina (Al_2O_3) nanoparticles with diameter of ~200 nm were used to induce superhydrophilicity on silicon substrate. Dispersion of these particles on the surface introduce nanoscale roughness which is partially responsible for enhanced wettability. A solution of nanoparticles and isopropyl alcohol was prepared to disperse nanoparticles on the substrate. Isopropyl alcohol is a suitable solvent as it has low surface tension which can spread thin layer of nanoparticles evenly on the surface. In contrast, solvents with higher surface tension tend to distribute nanoparticles unevenly, creating spots with agglomerated nanoparticles. Isopropyl alcohol is also non-reactive to the silicon surface and immediately evaporates upon spreading. Hence, nanofluid was prepared by mixing 1 g of alumina nanoparticles with 1 liter of isopropyl alcohol. This mixture was subjected to ultrasonic bath at a frequency of 42 KHz for one hour. Density of the nanofluid can be made different than this prescribed value. This will only increase or decrease the number of cycles required to obtain optimal coating as described in section 2.2.4.

Two different methods were implemented to fabricate Superhydrophilic Nanoporous coating (SHNC), which are spin coating and dipping method. Both of the methods rely on adherence of nanoparticles to the substrate by evaporation of solvent. The silicon substrate was metalized prior to coating fabrication. A thin layer of chromium with thickness of ~400 ^{0}A was deposited by using E-beam evaporation followed by sputtering of aluminum with a thickness of ~1,000 ^{0}A. The chromium layer acts as an adhesive layer

between silicon substrate and aluminum layer. Thus the metalized surface was found to provide better bonding than plain silicon.

In spin-coating technique, aluminum coated silicon substrate was placed on a chuck connected to a vacuum pump which maintains the contact between substrate and chuck at high RPM. Nanoparticle solution was dispensed on the sample placed on the chuck. Initially the nanoparticles solution is puddled on the center of the substrate mainly when a large substrate is used like a four inch wafer. In order to spread the nanoparticle evenly all over the sample, it was spun at 500 RPM for 5 seconds as shown in Fig. 3.13. The thickness of the nanoparticle solution was considerably thicker even at the end of this step. If the nanoparticle solution is left to dry at this point, amalgamated nanoparticles will form unevenly throughout the sample, which can be visually observed. Reducing this thickness is important for uniform distribution of nanoparticles. Hence, a second spin cycle was incorporated in the fabrication process where the sample was spun at 1500 RPM for 20 seconds, reached by incrementing the RPM as indicated in Fig. 3.13.

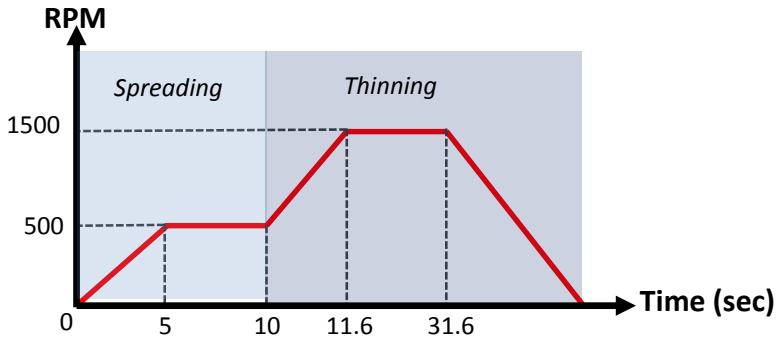

Figure 3-13 Steps of Spin Cycle

In the dipping method, aluminum coated silicon sample was dipped in the nanofluid solution and the sample was held vertically after removing from the nanofluid solution to get rid of excess nanofluid. Remaining nanofluid solution on the substrate was dried by blowing hot air. Thus dried nanoparticles solution layer is comparatively thicker than the

one in spin coated samples. Amalgamated nanoparticles are found to be unevenly distributed on the sample. This again is visible on the surface.

3.2.2 Hot Water Treatment

Bonding strength of the fabricated nanoporous coating is not strong enough for the evaporative cooling tests. One way of reinforcing the bonding of the nanoparticles to the substrate is hot water treatment of the coating. This process promotes the oxidation-hydroxylation of the surface and strengthens the bonding between aluminum coated silicon and alumina nanoparticles. The nanoporous coatings obtained by dipping and spin-coating underwent hot water treatment of 10 minutes in a boiling water bath.

3.2.3 Coating Durability

Durability of the hot water treated SHNC was evaluated by measuring contact angle of the coating after intervals of ultrasonic washing. The steadiness of contact angle value (stability of wettability) with accumulated time in ultrasonic washing would indirectly indicate the coating's bonding strength. The initial contact angle of water was ~3^{o} for both methods as shown in Fig. 3.14. For the spin coating method, contact angle stabilized at ~15^{o} after ~12 minutes (blue rhomboids), indicating that a substantial remnant of highly wetting coating endured. The initial degradation in the first 12 minutes could be attributed to the unattached particles that could not bond with the substrate during hot water treatment. However, contact angle of the sample prepared by dipping method continuously increased (red circles), indicating continuous coating detachment. This indicates that spin-coated SHNC promises high durability under liquid delivered during the testing. Hence, spin coated SHNC was used for all the testing.

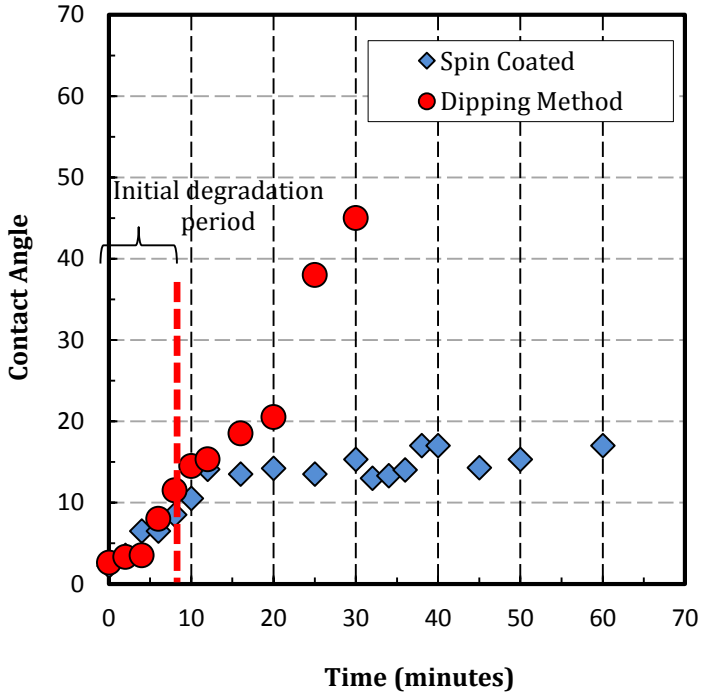

Figure 3-14 Durability Evaluation of SHNC Options Fabricated by Two Different Coating Methods

3.2.4 Coating Optimization

A variation of SHNC surfaces was prepared by varying the number of nanoparticle deposition cycles. Wettability of these surfaces was evaluated by dispensing a water sessile drop of volume ~75 nl using the solenoid valve. Images obtained from high speed camera shown in Fig. 3.15 were used to quantify the area of spreading over time.

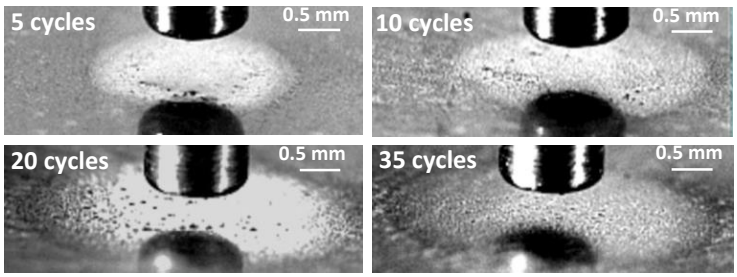

Figure 3-15 Illustration of Spreading of Single Dose of Delivered Water (~75 nl) on Different SHNC Coating Options

Results shown in Fig. 3.16 indicate significant gains in the rate of spreading when number of cycles was increased from 5 to 35.

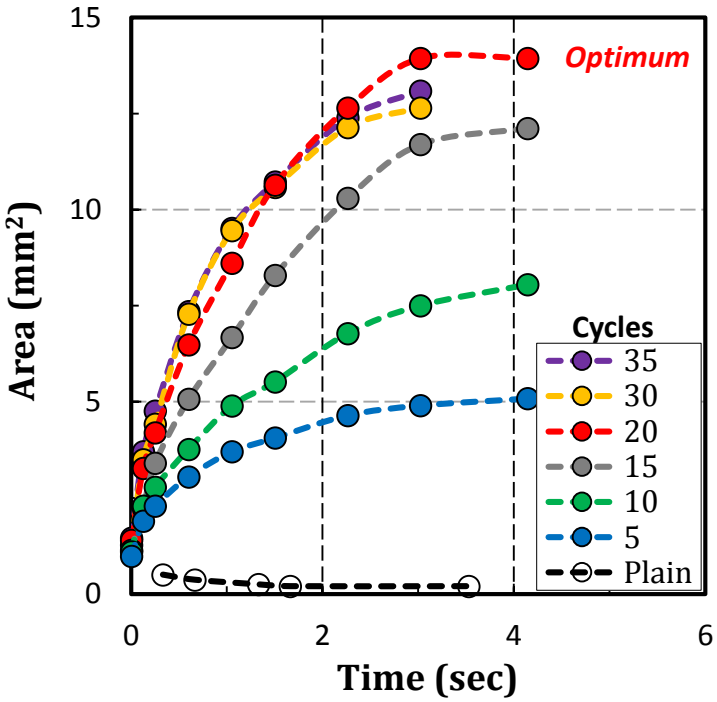

Figure 3-16 Measured Areas of Spreading on Various SHNC Coating Options

Maximum area of spreading (at t ≈ 3 sec) was increased up to ~14 mm^2, for SHNC coatings made in 20 cycles or more, as compared to ~5 mm^2 of 5 cycle coatings. Based on the volume of dispensed sessile drop and the area of spreading, the thin film thickness at ~4 sec of spreading is estimated to be ~9 µm and ~5 µm for the coatings made in 10 and 20 cycles, respectively. SEM images of these coatings were taken at a very high magnification (20K and 100K) as shown in Fig. 3.17. For surfaces made in 20 cycles, their structures appear to be more closely located as compared to those of 5 cycles. Surface roughness of all the samples was also measured using a profilometer. The average roughness value was calculated over a 500 µm length on a 10×10 mm^2 substrate. The

average roughness for the coatings made in 5, 10, 15, 20, 30 and 35 cycles were found to be ~37 nm, 71 nm, 86 nm, 123 nm, 134 nm and 108 nm, respectively.

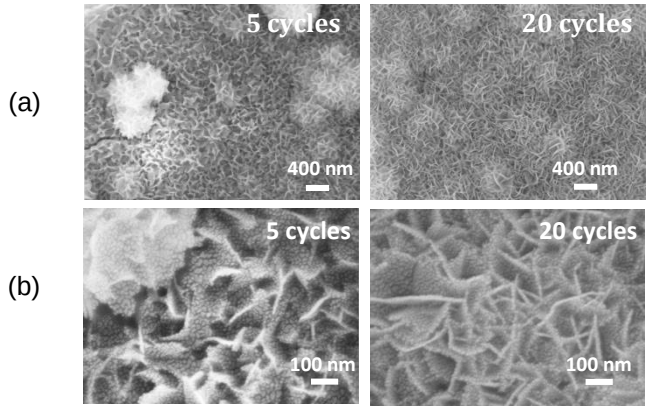

Figure 3-17 SEM Images of SHNC at (a) 20K (b) 100K Magnification.

3.3 Test Results

3.3.1 Liquid Cooling Tests (Open Tests in Ambient Conditions)

3.3.1.1 Baseline Case (Plain Silicon)

The experiment was first conducted on a plain silicon surface which was used as a baseline case for comparison. The test was conducted in ambient conditions of pressure and temperature at constant flow rate of 500 Hz with a droplet size of 74 nl. Liquid delivery system was started prior to applying any heat flux. During the test, delivered water accumulates on the plain silicon surface which eventually spreads out of the chip footprint (10×10 mm^2). This excess water was drained using a vacuum pump as shown in Fig 3.10. The use of vacuum pump for excess water removal was limited to tests conducted at open condition and excluded for tests in micro gaps. The cooling test result is shown in Fig. 3.18. The arrow symbol at the end of the test indicates the onset of dry out. This will apply to all the figures in the following sections. At ~260 W/cm^2, the delivered droplet cannot spread on the hot spot fast enough to prevent the rapid increase of hot spot temperature triggering

a temperature spike. This point was considered as the dry out heat flux as previously explained. On time arrival of water drop to the hot spot was not critical here as the droplet was dispensed at high enough frequency (500 Hz). It is the lack of spreading which causes the pooling of liquid plus the exposure of a significant portion of the heated surface to the air and this is primarily responsible for onset of dry-out.

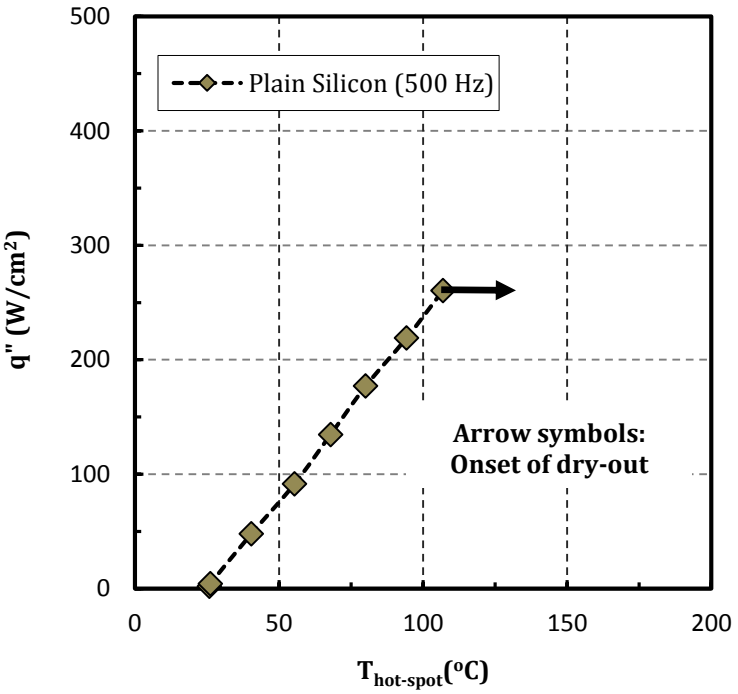

Figure 3-18 Cooling Performance of Plain Silicon Surface

The accumulated water, as shown in Fig 3.19(a), was drained by a vacuum pump. Immediately afterwards, the remnant of the pooled water could not spread on plain surface, exposing a portion of heated surface to the air as shown in Fig 3.19 (b). And this was sufficient to spike the hot spot temperature well beyond the set criteria of dry out. As mentioned earlier, the temperature jump of 40°C or more from the preceding steady state value is defined as the arrival of dry out in the current study.

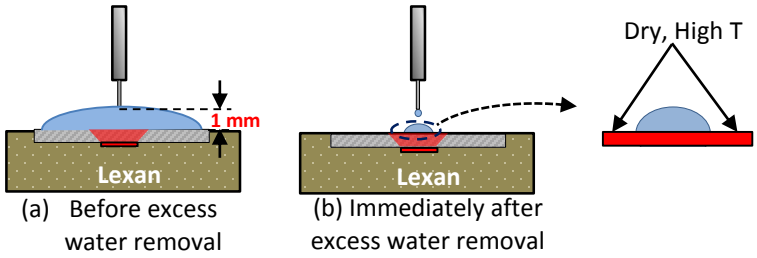

Figure 3-19 (a) Pooling of Liquid and (b) Appearance of Dry Area

3.3.1.2 Performance Comparison of Plain and SHNC Surfaces

The cooling performance of SHNC coating described in section 2.2.4 (10 cycles) was assessed and compared with plain surface in Fig. 3.20. All the tests were conducted at ambient conditions of temperature and pressure in open condition.

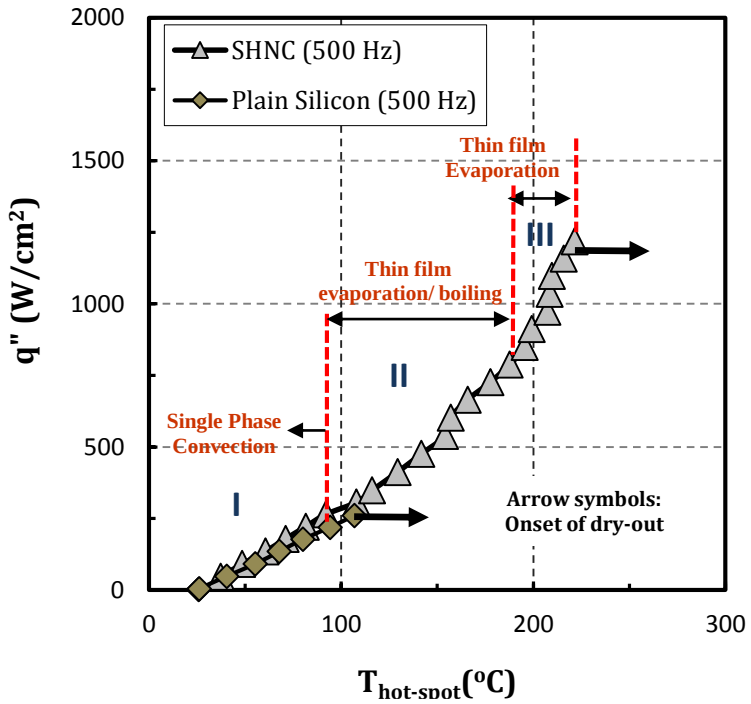

Figure 3-20 Performance Comparison of Plain and SHNC Surfaces

Dry out heat flux enhanced by ~3.5 times as compared to plain surface. This enhancement can be attributed to the faster wetting of liquid and complete coverage of hot spot by individual drop on SHNC. As shown in Fig. 3.16, SHNC fabricated by 10 cycles is capable of spreading water enough to cover the footprint of hot spot (4 mm^2) in just ~1.05 seconds. However, as mentioned earlier, the plain surface could not spread beyond a small fraction of hot spot size even after a long time. This boost in wettability due to SHNC is the major contributor to the remarkable delay in dry out heat flux. Performance below ~300 W/cm^2 (region I) corresponds to minimal phase change heat transfer. This could be attributed to the excessive pooling of liquid observed at lower heat fluxes. The increase in hot spot temperature from ambient at the beginning of the test to ~ 90^oC occurred by increasing the heat flux from 0-300 W/cm^2. As the heat flux grew beyond 300 W/cm^2, phase change becomes more pronounced which is indicated by steeper slope. This is evident in that the total increment in hot spot temperature of only 114 degrees was observed for a net increment of 918 W/cm^2 of heat flux.

High speed visualization was conducted at heat flux of 200, 750 and 1150 W/cm^2 of Fig.2.20. Images from these heat fluxes can provide information on heat transfer mechanism at low, moderate and high heat flux. Fig. 3.21 presents these images with their respective heat fluxes. These snapshots are taken between deliveries of water to the hot spot. Figure 3.21(a) shows snapshot taken at 200 W/cm^2. There is not any visual indication of boiling or evaporation at this heat flux. Hence, this could be either single phase convection or preliminary stage of phase change. However, Fig. 3.21(b) shows that at 750 W/cm^2 there is a growing vapor bubble. This confirms the manifestation of phase-change heat transfer at moderate heat flux in the form of thin-film boiling (region II). The thin-film boiling diminishes at higher heat flux. Figure 3.21(c) shows the complete disappearance of nucleating bubble at ~1150 W/cm^2. It is plausible that the mode of heat transfer at higher

heat flux is mostly thin-film evaporation (region III). This transition of heat transfer mechanism from thin-film boiling to evaporation is ascribed to an incessant thinning of liquid film as the heat flux grows. The range of these heat transfer mechanisms is shown in Fig. 3.20 based on visual observation during the test.

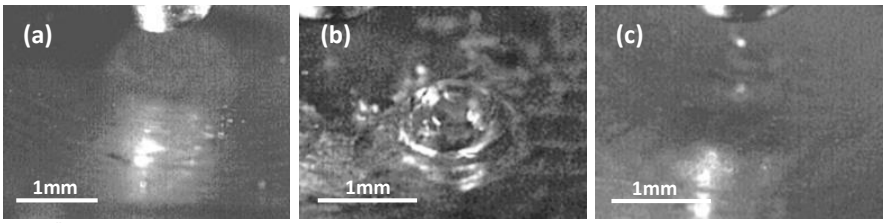

Figure 3-21 Images Taken During 500 Hz Test at (a) Low, (b) Moderate and (c) High Heat Flux on SHNC Surface

Hence, the heat transfer mechanism during the test can be classified into two major categories which are explained with the aid of Fig. 3.22. As shown in Fig. 3.22(a), there exists a mixed mode of heat transfer up to ~800 W/cm2. Here, thin-film boiling is believed to be dominant over evaporation. Further increasing the heat flux will result in transition of thin film boiling into thin film evaporation (Fig. 3.22b) due to reduced liquid film thickness as mentioned earlier. At this point, the water film is in proximity of the mouth of the cavity responsible for thin-film boiling due to thin liquid film. This enables the film to evaporate before the nucleation.

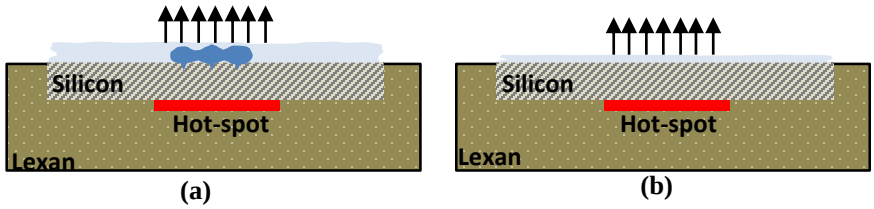

Figure 3-22 Schematic Representation of (a) Mixed Mode of Heat Transfer (Thin Film Boiling Plus Evaporation) and (b) Thin Film Evaporation

Bubble dynamics are different in thin film boiling than in pool boiling. Figure 3.23 shows the life cycle of the bubble shown in Fig.3.21 (b), its inception, growth and rupture. The vapor bubble grows beyond the thin-film boundary and the interface breaks.

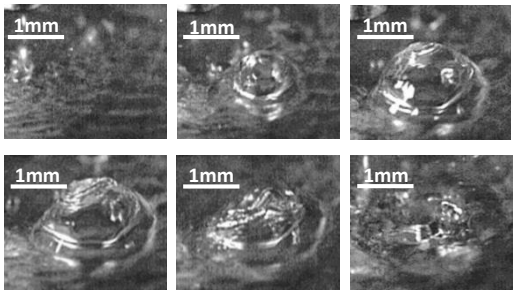

Figure 3-23 Images Taken During a Cycle of Bubble Growth

and Rupture during Thin-Film Boiling

The first snapshot in Fig. 3.23 was taken when the bubble is about to grow out of the thin-film boundary. At 0.986 ms, the bubble has significantly grown beyond the film thickness. Around 1.109 ms, air and vapor interface fluctuates. The interface finally ruptures at about 1.726 ms. This behavior of bubble growth and rupture was captured when there was no droplet delivery in progress that is, during air time of the valve.

3.3.1.3 Effect of Flow Rate

Effects of flow rate on hot spot temperature and dry out heat flux was evaluated by running tests at flow rate of 300, 500 and 600 Hz at ambient and open condition. The test results are shown in Fig. 3.24 (a). There is noticeable enhancement in dry out heat flux with increasing flow rate. This enhancement is a natural consequence of faster droplet arrival, minimizing the dry interval (time between complete water evaporation and next droplet arrival). Figure 3.24(b) demonstrates that there is a linear increment in dry out heat flux with flow rate. At the same time, flow rate has marginal effect on hot spot temperature. There is a net degradation of ~10oC at 200 W/cm^2 for flow rate of 300 Hz as compared to 500 and 600 Hz. This is due to better single phase (or preliminary stage of phase change) forced convection by 500 and 600 Hz as compared to 300 Hz. However, flow rate of 300 Hz showed a net enhancement of ~5 ^{o}C at 800 W/cm^2. This could due to the reduced thermal resistance across the water film as a result of thinner film (caused by lower flow rate). Ideally the mass flow rate desirable for better cooling performance at higher heat flux is such that the droplets arrive at the hot spot before complete evaporation of preceding droplet and provides a complete coverage to the heated surface. However, liquid film breaks exposing a portion of the heated surface to the air at high heat flux when the mass flow rate is relatively lower. This condition can also be called a partial dry out which leads to the degradation of cooling performance and eventually complete dry out.

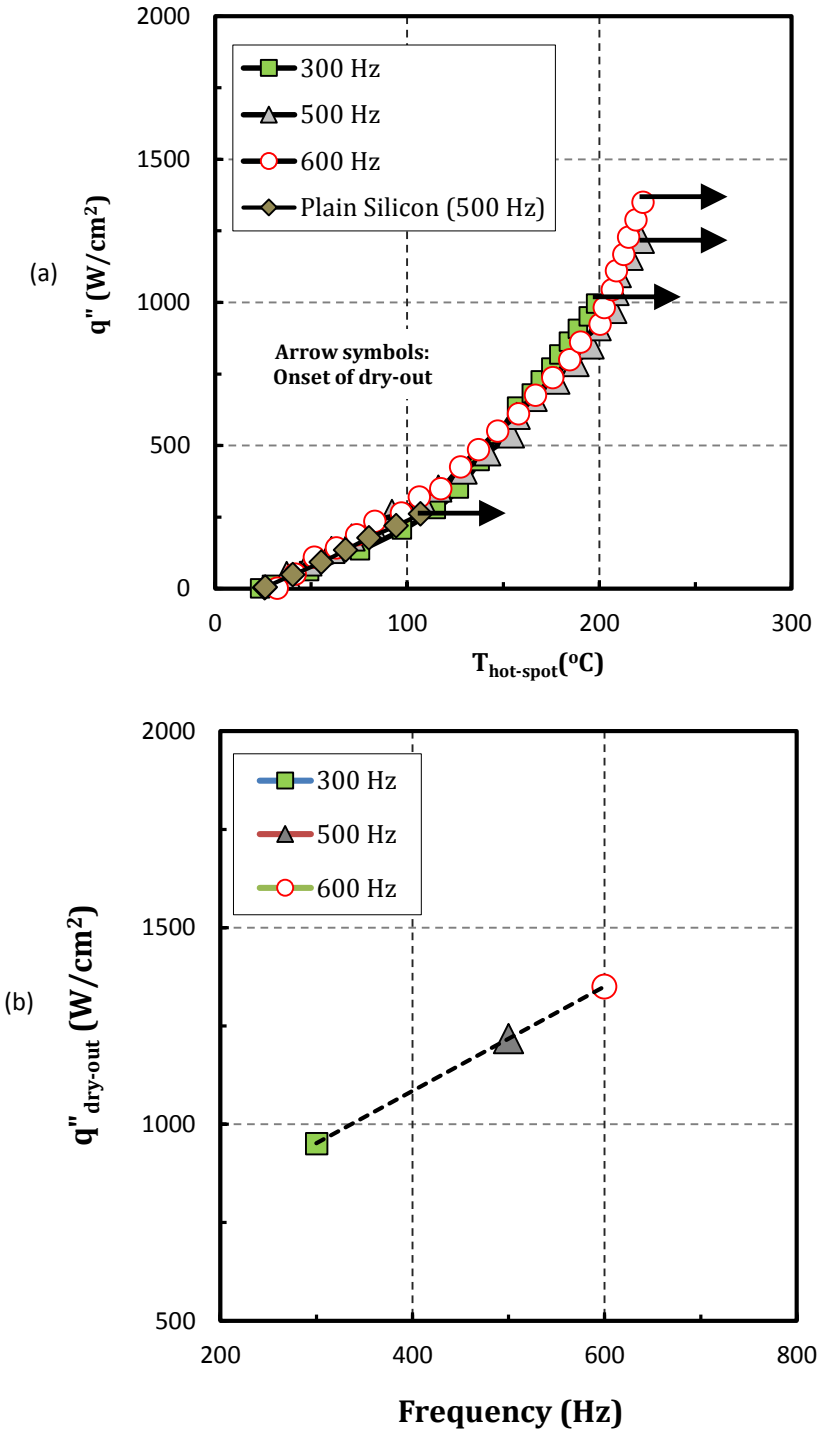

Figure 3-24 (a) Cooling Performance at Various Flow Rates, (b) Relation between Flow Rates and Dry Out Heat Flux

An effort was made to capture the dry out phenomena with the aid of high-speed camera. The vigorous evaporation taking place towards dry out heat flux hindered the visualization particularly for tests conducted at mass flow rate of 500 and 600 Hz. Hence, the dry out process was captured at lower mass flow rate of 300 Hz. The consecutive images during the dry-out are shown in Fig. 3.25(a). Images captured at various intervals indicate the occurrence of Leidenfrost phenomena or film boiling of 74 nl droplets on heated surface. The repulsion of droplet as shown at time intervals of 1.233 and 1.479 ms is a consequence of pressure field established due to rapid vaporization of droplets near superheated surface. If the pressure force balances the weight of the droplet, the droplet hovers on the heated surface as shown in Fig. 3.25(b). However, pressure force must be exceeding the weight of the droplet in the current test as the repulsion of the droplets was perceived. Major heat transfer during this process occurs by conduction through vapor film between droplet and superheated silicon surface, and by radiation. This phenomenon has been observed in cooling rocket nozzles, fuel droplet vaporization in fuel-injected engines, reflooding of nuclear reactor after accident due to loss of coolant [25].

(a)

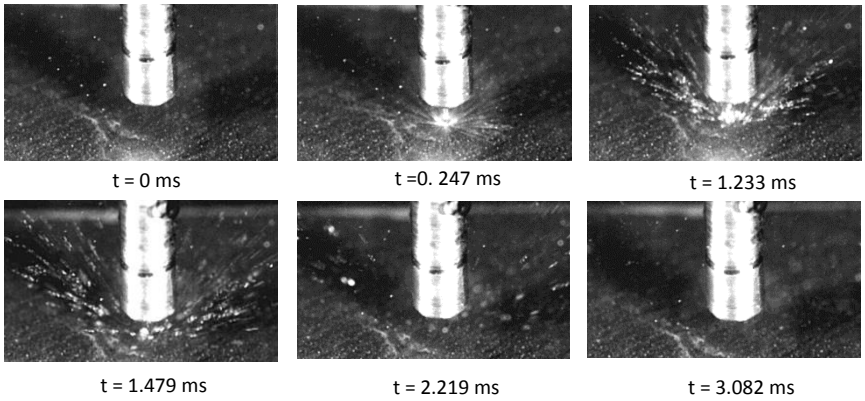

(b)

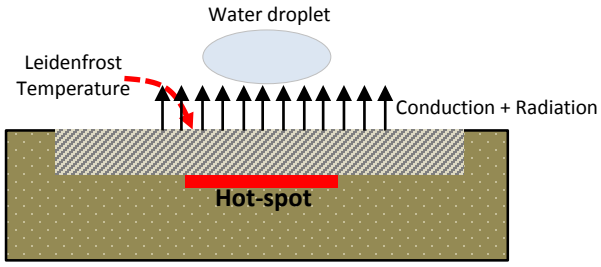

Figure 3-25 (a)) Dry-out Taking Place at 300 Hz, (b) Schematics of Droplet Hovering due to Pressure Field

3.3.1.4 Effect of Wettability

Wettability plays an important role particularly at higher heat flux where heat transfer occurs by thin film evaporation. Better wettability provides faster rewetting of dry spot delaying the dry out. Similar observation was reported in chapter 1 where the wettability promoted the faster rewetting of evaporating microlayer of nucleating bubble in pool boiling and resulted in enhanced BHT and CHF. In an effort to further increase the wettability of SHNC, optimization study was conducted by altering the number of spin cycles. The details of coating optimization are explained in section 3.2.4. Coating fabricated with 25 spin cycles was found to be the optimal in terms of wetting speed and wetting area. The cooling test results obtained in 25 cycles (highly wettable) is compared with the one

with 10 cycles (wettable) in Fig. 3.26. The optimized SHNC yields ~12% enhancement in dry out heat flux. Most importantly, the hot spot temperature is cooler at all heat flux levels above 200 W/cm^2 for the optimized coating. This enhancement is ~19^{o}C at 1000 W/cm^2. Figure 3.16 in section 3.2.4 indicates that there is ~33% enhancement in time required to spread water film on hot spot area (4 mm^2) for optimized SHNC relative to the one made in 10 cycles. This could be responsible for the observed enhancement in dry out heat flux and hot spot temperature.

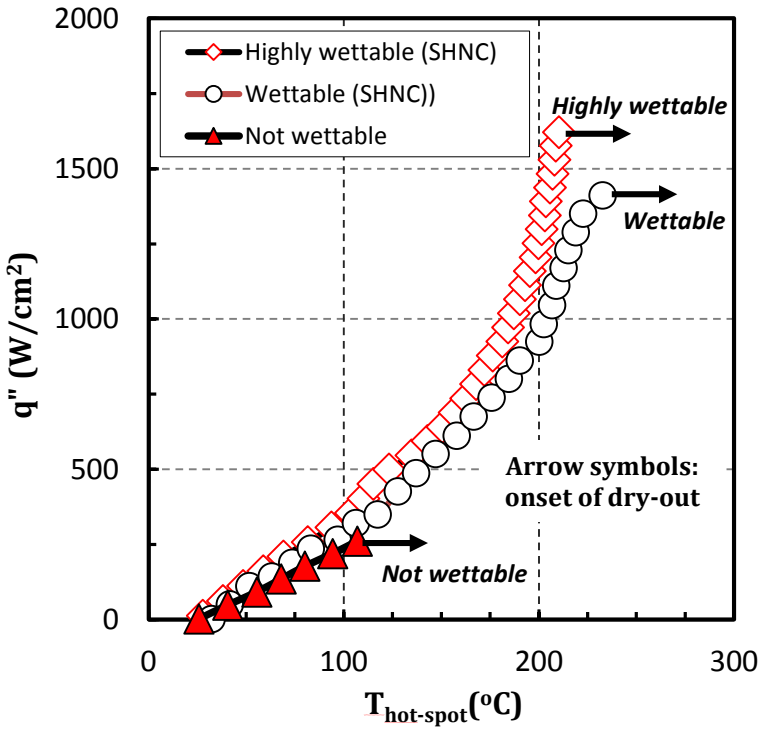

Figure 3-26 Effect of Surface Wettability

3.3.1.5 Effect of Variable Mass Flow Rate

The above tests were conducted at constant mass flow rates set by delivery frequencies of 300, 500 or 600 Hz. All demonstrated noticeable delay in dry out heat flux compared to a plain silicon surface. However, water pooled at lower heat flux and also the

water film thickness appeared to be too thick to instigate thin-film evaporation at moderate heat flux. In order to prevent this excess supply of water up to moderate heat flux, tests were also conducted with variable mass flow rate on SHNC made in 25 cycles (Fig. 3.16) and plain surface. During these testing mass flow rate was increased with increasing heat flux. The required mass flow rate was calculated by utilizing known droplet volume and the latent heat of vaporization of water, as given by:

$$f = \frac{q}{\rho \times V \times h_{fg}} \tag{3.2}$$

where, "f" is the frequency with which the water droplet of volume "V" is delivered to the chip dissipating a power of q. The increment in frequency with heat flux was automated by the data acquisition system (DAQ). DAQ manipulates the pulse duration (PD) of the pulse generator according to the applied heat flux. When temperature at a given heat flux reaches steady state, DAQ signals the increase in power supply and pulse duration simultaneously. During high heat flux (higher frequency) a small portion of delivered droplet appeared to be bouncing from the surface. Hence, lost water was compensated by also running tests at 120% and 150% of the frequency calculated by Eq. (3.1). Test results are plotted in Fig. 3.27. These tests were conducted using the coating made in 25 cycles (Fig.3.16). Dryout heat flux increased by 20% and 80% by increasing the excess mass flow rate by 20% (triangles) and 50% (squares), respectively. Phase change heat transfer is indicated by steeper slope in all cases. Heat transfer coefficient was found to be marginally enhanced by increasing the mass flow rate from 100% to 120% and 150% of the calculated values. When compared to the test conducted at constant mass flow rate (600 Hz), the test result obtained from 150% mass flow rate had higher hot spot temperature up to 500 W/cm^2. However, the curves come closer beyond this heat flux. From visual inspection, initially water spreads into a thin film on SHNC and the thickness of thin film continually grows until heat flux reaches ~100 W/cm^2. Phase change heat transfer is not in full effect

up to this point. Exceeding this heat flux promotes phase change heat transfer and consequently, the liquid film thickness on the surface decreases.

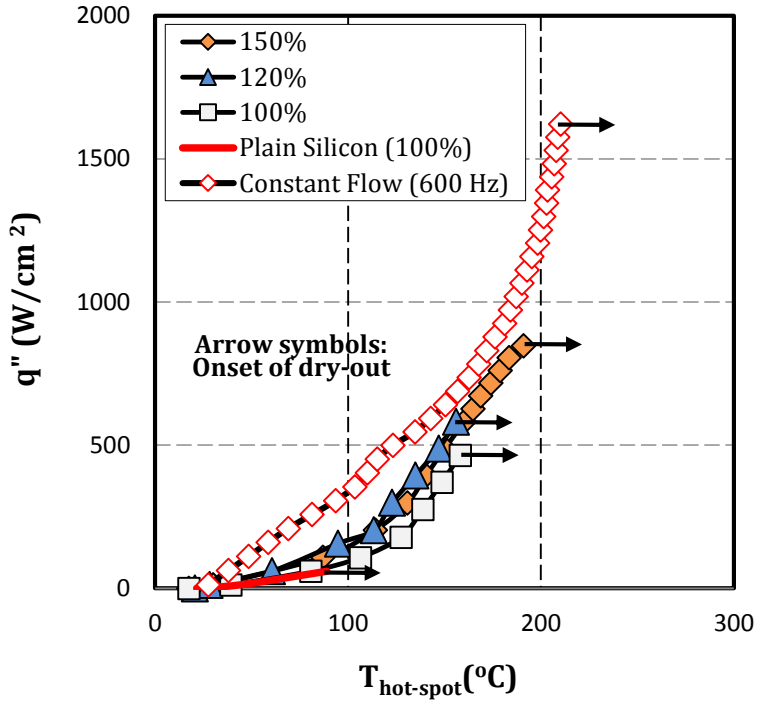

Figure 3-27 Test Results with Variable Mass Flow Rate

Figure 3.28 shows snapshots taken at three different heat flux levels during the course of the test conducted at 100% mass flow rate in Fig. 3.27. Figure 3.28(a) shows spreading of the water film on SHNC surface at 25 W/cm^2. Absence of thin film boiling and absence of dry spot suggests either single phase or preliminary stage of phase change heat transfer. Figure 3.28(b) captures the appearance of the dry zone right above the hot spot at ~200 W/cm^2. There is a net increment of ~ 110 degrees in hot spot temperature from increasing the heat flux from 25 to 200 W/cm^2 (see fig.3.27). Images taken at 400 W/cm^2 of the dry spot's appearance and expansion until the next droplet is dispensed are shown in Fig. 3.28(c). The first snapshot was taken immediately after water had been dispensed. The dry spot, as shown in the images, increases in size as time progress until the next dose

arrives. The maximum dry spot area increases in size with increasing heat flux. At sufficiently high heat flux the successive dose of liquid cannot reach the hot spot before the complete evaporation of liquid film and triggers dry out.

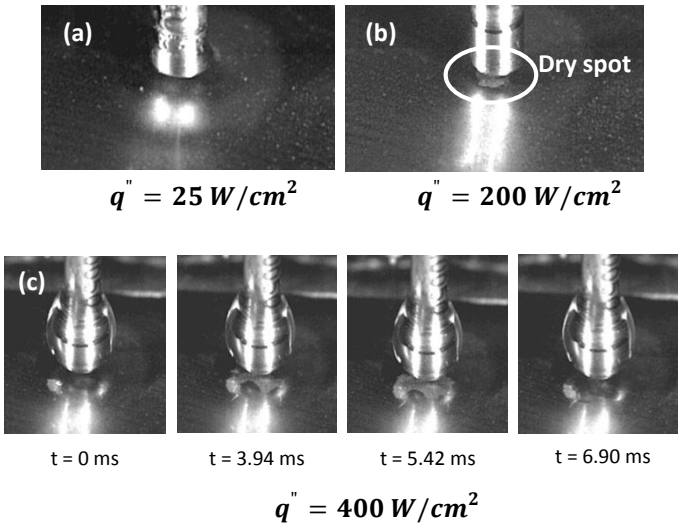

Figure 3-28 Image Taken During 100% Mass Flow Rate at (a) Low Heat Flux (25 W/cm^2) (b) Appearance of Dry Spot (200 W/cm^2). (c) Dry-Zone Expansion and Delivery of Successive Droplet

3.3.2 Test in Micro-Gap and Various Environmental Conditions

Cooling schemes like heat pipe and vapor chamber that rely on evaporation work in a gas free environment. In these components, the working environment is degassed, so the reduced working pressure can instigate phase change heat transfer at relatively lower temperature. However, implementing such component for thermal management of embedded microelectronic system could be challenging in terms of providing hermetic seal. Also, the constraint in space may arise the system pressure and temperature. Hence, a systematic effort is made in this section to address any drawback of cooling hotspots in space constraint gassy situation.

3.3.2.1 Test in a Micro-Gap at Ambient

A test was first conducted on a plain silicon surface in a micro-gap maintaining the ambient conditions of temperature and pressure. This test result was used as a baseline case. The design of the micro-gap is explained in section 3.1.4.2. The two sides of the enclosure are sealed and the other two are left open to allow the water vapor to flow out. The gap size of 500 µm was maintained between top cover plate and the silicon substrate. This gap size was confirmed under the optical microscope prior to each test. The test result conducted at 600 Hz is shown in Fig. 3.29. The micro gap helps to spread the liquid on plain silicon surface irrespective of poor wettability on plain silicon surface. This maintains the complete coverage of hot spot and consequentially delays dry out heat flux compared to open case previously shown in Fig. 3.18.

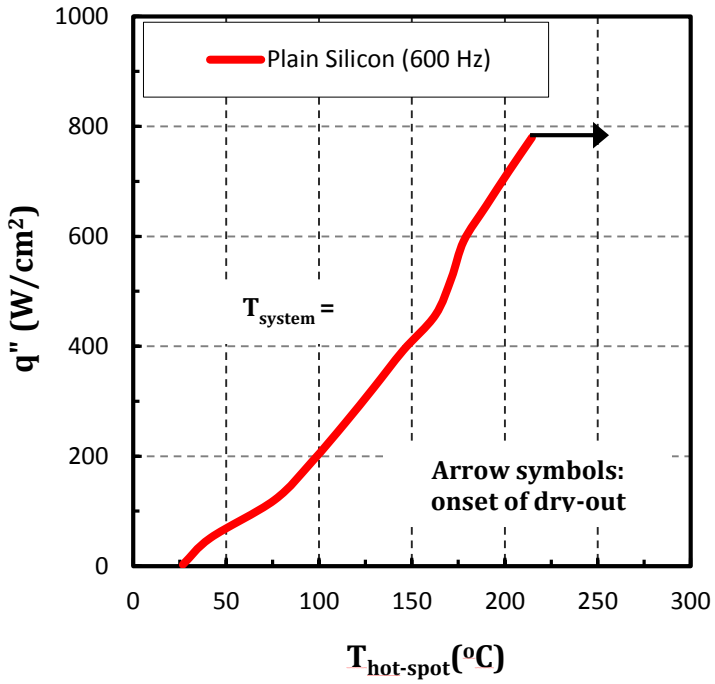

Figure 3-29 Tests on Plain Silicon in a Micro-Gap

Result on the plain surface was then compared with tests conducted at two flow rates on SHNC surfaces as shown in Fig. 3.30. All the tests were conducted on optimized

SHNC (20 spin cycles) and same coating was used in all subsequent tests as well. There was an enhancement of 105% for 600 Hz case in dry out heat flux relative to plain silicon surface. The hot spot temperature was ~63oC cooler at 750 W/cm2. This enhancement is again attributed to better and faster wetting of hot spot by SHNC. Flow rates of 500 and 600 Hz were found to have similar effect on cooling performance as reported in Fig. 3.24 which is that higher flow rate provides higher dry out heat flux with marginal effect on hot spot temperature for heat fluxes common to both flow rate cases. The presence of top cover plate with an embedded nozzle prohibited the visualization during the test. However, intense outflow of vapor from both open ends of the micro-gap was observed. This was a direct consequence of vapor pressure gradient built due to vapor accumulation inside the micro-gap. And this trapped vapor partly contributes to the increase of dispensed water coolant temperature.

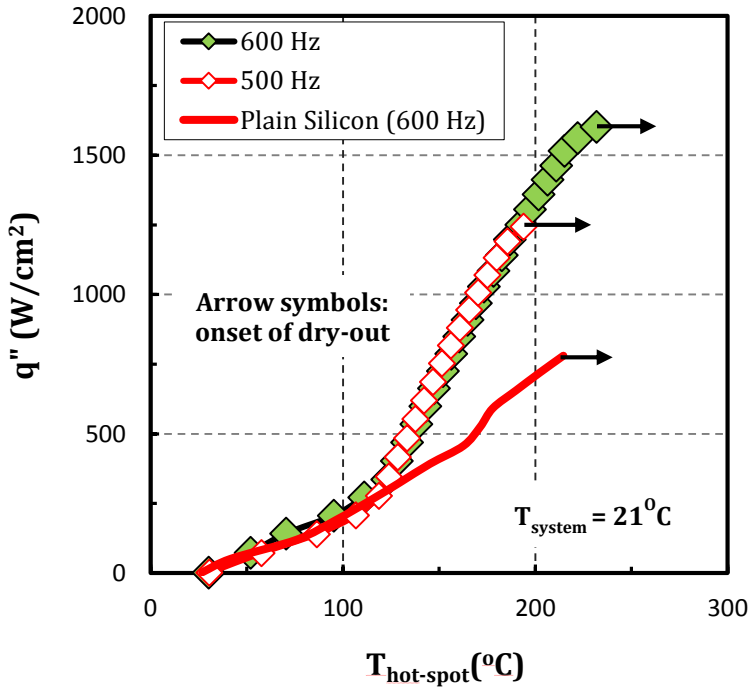

Figure 3-30 Comparison of Plain and SHNC Surfaces in a Micro-Gap

3.3.2.2 Tests in a Micro-Gap inside a Pressure Vessel (Effect of System Pressure)

Cooling tests were then conducted inside a pressure vessel at various system pressures with constant mass flow rate of 600 Hz. The details of the pressure vessel are provided in section 3.1.2. It has been well know that the increased system pressure enhances nucleate boiling heat transfer coefficient. Nishikawa et al [51] explained this as a consequence of increase in active nucleation site density at a given wall superheat. However, the transition of thin film boiling to thin film evaporation as heat flux increases in the current study makes it difficult to predict the effect of pressure. To the author's knowledge, there has not been any work reported quantifying the effect of pressure on mixed mode of heat transfer (thin-film boiling and thin-film evaporation). In the current study, effects of three different system pressures 14.69, 22.04 and 29.39 psi are reported. The pressure was elevated using compressed air maintaining the gassy environment, emulating the actual embedded thermal management system. The dispensed droplet volume is a function of pressure drop across the nozzle. Hence, to maintain the same droplet volume as that used during the tests conducted at atmospheric pressure, the pressure on the water reservoir was adjusted to always be 15 psi above the setting of the higher system pressures. All the test results conducted at elevated pressures are shown in Fig.3.31 (a). There is slight enhancement in dry out heat flux at 22.04 and 29.39 psi compared to the ambient case. In Fig. 3.31(a), the hot spot temperature appears to be degrading with elevated system pressures. This degradation could be a result of increased saturation temperature at elevated pressure. The saturation temperature of water at 14.69, 22.04 and 29.39 psi is 100^{o}C, 112^{o}C and 120^{o}C respectively. This increment in saturation temperature is incorporated in Fig. 3.31(b) by plotting heat flux against the difference of hot spot temperature and saturation temperature.

(a)

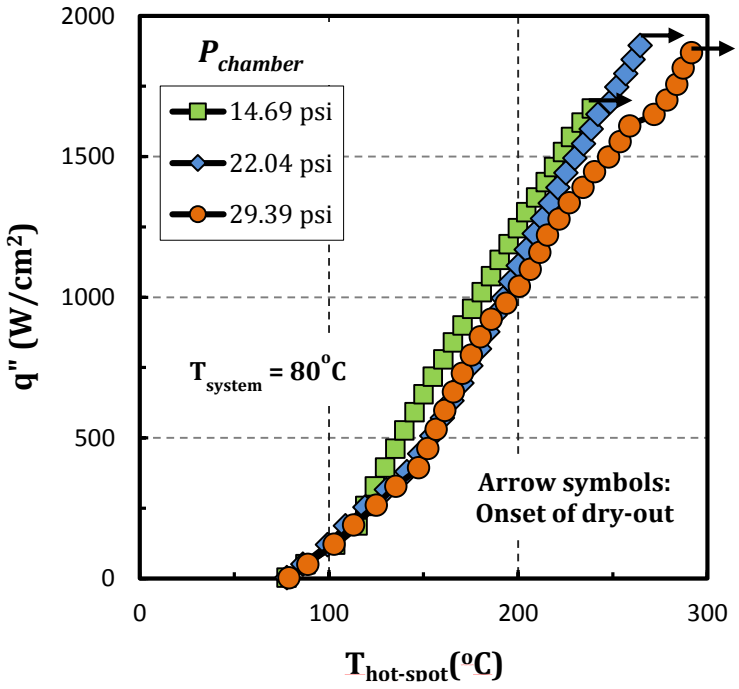

(b)

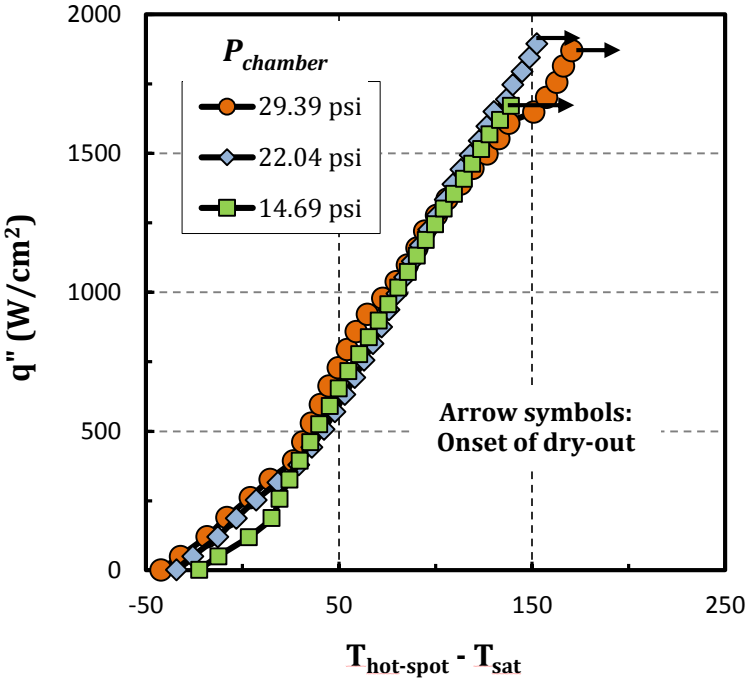

Figure 3-31 Effects of (a) System Pressure on Cooling Tests, (b) Change in Saturation Temperature on Cooling Performance at Elevated Pressures

In Fig.3.31 (b), the curves fit into a narrower band except below 250 W/cm^2, which confirms that the increase in saturation temperature at elevated pressure contributes to increased hot spot temperature.

3.3.2.3 Effect of System Temperature

All the system temperature tests were conducted at atmospheric pressure in gassy condition. The system temperature in the present study can be explained by the thermodynamic system illustrated in Fig.3.32. This system contains two distinct regions which are bulk water and mixture of gas and water vapor. The total system pressure (P_{sys}) is an aggregate pressure of water vapor and non-condensable gas partial pressure (P_g). The system pressure is always maintained at 1 atm for all system temperatures. The bulk water pressure is equivalent to the system pressure (P_{sys}).

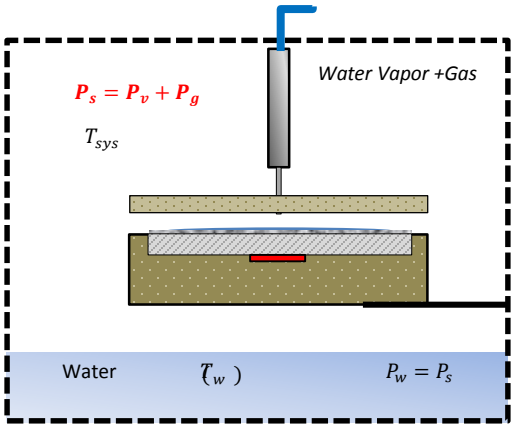

Figure 3-32 Schematic of Thermodynamic System of Subcooled Testing

The subcooling in this work is defined as the amount by which the system temperature (T_{sys}) is reduced below the saturation temperature at system pressure of the bulk water as shown by equation 3.3.

$$\Delta T_{sub} = T_{sat}(P_{sys}) - T_{sys} \tag{3.3}$$

Three different system temperatures were tested in the present work which were 20 ^{o}C, 50 ^{o}C and 80 ^{o}C. Test results are shown in Fig. 3.33. There is not any noticeable effect of system temperature except marginal fluctuation in dry out heat flux. The tests conducted with system temperature of 50 and 80^{o}C yield temperatures lower than their corresponding system temperatures at the two lowest applied heat fluxes. This is because the cooling water is kept at room temperature (~21^{o}C) within a reservoir outside the test vessel. In the current study all the tests conducted at various system temperature collapse on each other after ~300 W/cm^2. This could be a result of vapor environment built in the space between chip and the top cover. This always maintains near saturation environment for the hot spot irrespective of the system temperature. The vapor outflow occurs through the two openings and this discharge of vapor becomes more vigorous with increasing heat flux.

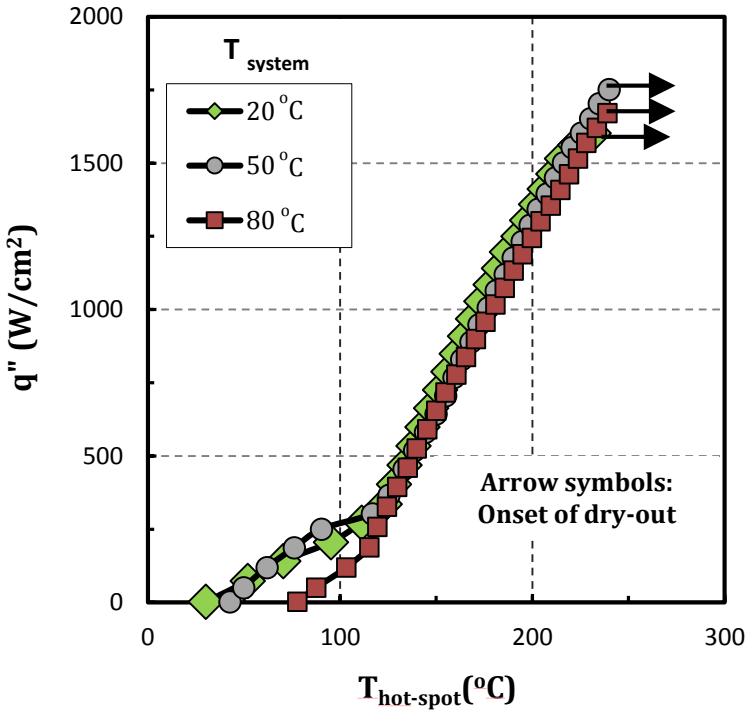

Figure 3-33 Effects of System Temperature on Cooling Performance

3.3.3 Heat Transfer Coefficient (HTC)

FEM analysis was conducted to estimate the heat spreader effect and the heat loss from the side walls at high heat flux. The micro-gap setup was modeled using SolidWorks. This model contains all the major components of actual micro-gap such as base Lexan block, silicon substrate, resistor, epoxy etc. ANSYS 15.0 was used for all the heat loss estimations. Temperature distribution across the silicon substrate at higher heat flux of 1,000 W/cm^2 was obtained by imposing conditions listed in table 3.1.

Table 3-1 Imposed Boundary Condition for Heat Loss Estimation

Surface	Thermal Conductivity (W/m.k)	T_∞(^{o}C)	h (w/m^{2}k)
Silicon	14	20-90	10000-30000
Lexan	0.2	2	5
Epoxy	0.1	2	5

The solution of the heater dissipating 1000 W/cm^2 at various conditions as mentioned in table 3.1 reveals that there is not any heat loss through the side walls. This can be seen in the temperature profile of the heater shown in fig. 3.34.

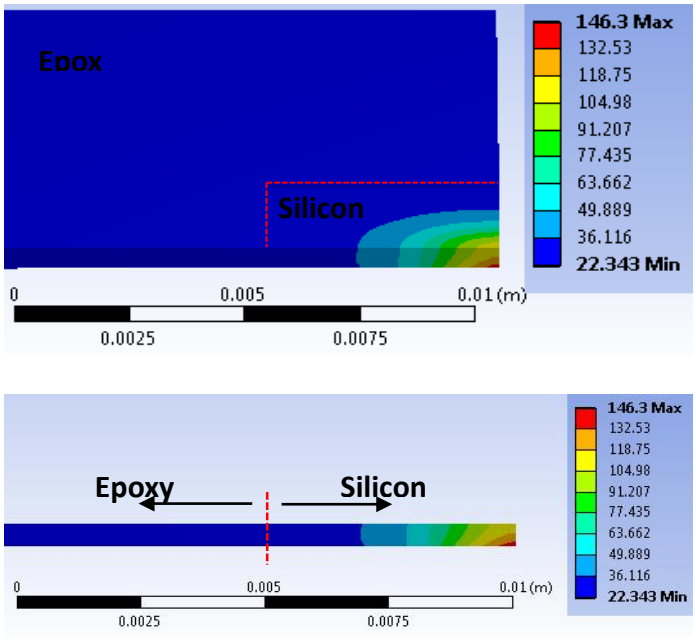

Figure 3-34 A Temperature Solution of Hot-Spot at Heat Flux of 1000 W/cm^2

One dimensional conduction is assumed to calculate the surface temperature for HTC estimation. This was based on insignificant heat loss and negligible spreading effect which was found to be less than 1% of applied power. Two t-type thermocouple was embedded in top-cover Lexan to measure micro-gap temperature at various heat flux levels. Each thermocouple was positioned at a distance of ~ 3 mm from the center of the chip such that the tip of the thermocouple was in contact with the micro-gap environment. The temperature measurements at various levels of heat flux was recorded and used as ambient temperature for the chip while calculating the HTC. Figure 3.35 compares the HTC of SHNC (500 Hz and 600 Hz) and the plain surface (600 Hz). SHNC yields higher HTC than plain silicon surface at all heat flux levels. A maximum HTC of 2.2×10^5 W/m^{2}k was achieved at heat flux of 1130 W/cm^2.

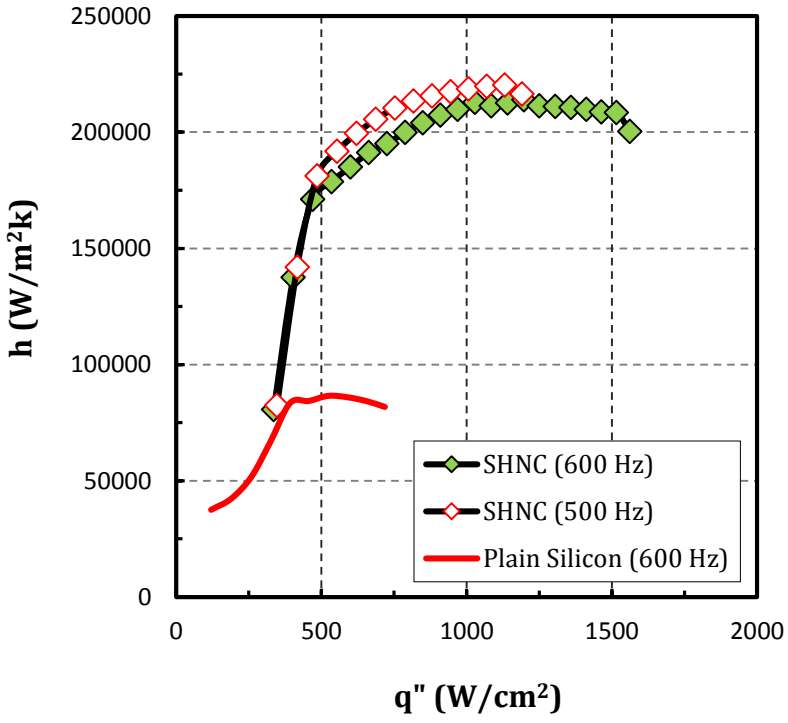

Figure 3-35 Heat Transfer Coefficient Comparison between Plain Silicon and SHNC Surfaces

Chapter 4

Heat Transfer Enhancement of a Hot-Spot by Thin-Film Boiling and Thin-Film Evaporation on Aluminum Microporous Coating

Hot spot cooling tests conducted on Superhydrophilic Nanoporous coating (SHNC) in chapter 3 demonstrated excellent improvements in dry-out heat flux and hot spot temperature compared to the plain surface. Two distinct heat transfer mechanisms were observed which are thin-film evaporation plus thin-film boiling (mixed mode) and thin-film evaporation. Mixed mode of heat transfer was dominant up to a moderate heat flux level. However, at sufficiently high heat flux, thin-film evaporation took over which was confirmed by high speed visualization in Chapter 3. This transition of heat transfer mechanism occurred due to continuous thinning of liquid film on hot spot with growing heat flux. With these observations, it is plausible that heat transfer from the hot spot can be further enhanced by increasing the number of nucleation sites and wettability of the surface. Increased nucleation site density will promote the thin-film boiling at moderate heat flux and improved wettability will enhance thin-film evaporation at higher heat flux. In an effort to increase the nucleation site density and wettability of the surface, a porous structure was created on the silicon surface which demonstrated superior wetting and wicking capability. SEM images also indicated the presence of micro scale cavities which can promote nucleation.

There have been a number of work reported on boiling and evaporation on porous media. King et al [52] studied the effect of microporous coating on evaporative cooling performance of water on aluminum substrate. Mughal and Plumb [53] conducted experiments on planar and channeled porous metal foam. They found evaporation to be the dominant heat transfer mechanism. Li and Peterson [54] evaluated evaporation/boiling heat transport phenomena in thin capillary wicking structures.

4.1 Aluminum Microporous Coating on Silicon Surface

Porous structure have long been the subject of investigation on metallic surfaces where the porosity was introduced by binding micron size particles using a binding agent. O'Connor and You [55] fabricated porous structure by applying a mixture of epoxy and silver flake particles. In this coating, epoxy was used as a binder. Poor thermal property of epoxy introduced a limitation to maximum attainable heat flux. Hence, its application was limited to refrigerants where the maximum attainable heat flux is comparatively lower than other fluid like water. Kim [56] used more conductive solder paste to bind copper particles on copper substrate. This coating demonstrated better performance as compared to earlier work. The current study benefits from these studies of porous structure. However, these works [55] [56] do not elaborate on wettability of the coating. Hence, to find the wettability of the coatings fabricated by O'Connor [55] and Kim [56], a brief investigation was conducted by fabricating similar coatings. Details of the fabrication process can be found in their respective works. Wettability was quantified by measuring static contact angle in a similar way to that shown in chapter 2. Results as shown in Fig 4.1(a) reveals poor wetting characteristics as the static contact angle was found to be 60 and 70 degrees for ABM and TCMC respectively. Both coatings are made of porous structure as shown in Fig 4.1(b), however, poor wetting characteristics of both coatings necessitated the fabrication of a new porous coating that is also wettable. The coating is made of aluminum particles which can be made highly wettable through a hot water treatment. Min and Web [57] conducted experiments to investigate the long term wettability of hot water treated aluminum. In this study, highly wettable aluminum was obtained from immersion in 82^{o}C or 100^{o}C water for 20 minutes. Near constant advancing and receding contact angle measurements was reported during the air exposure tests conducted over a period of 25 days. Usually, a layer

of ~3.1nm [58] thick layer of native oxide is formed on aluminum when exposed to air. Nikaido et al [59] reported the thickness of oxide formed by hot water treatment to be ~1µm. This increased thickness of oxide layer is responsible for enhanced wetting on hot water treated aluminum. Hence, aluminum based microporous structure on silicon substrate was pursued to further the enhancement obtained from the SHNC. During fabrication, high temperature durability of the coating was considered due to the fact that hot spot can reach a temperature beyond the operating range of epoxy and solder pastes used in prior microporous coatings. Hence, brazing paste, with melting temperature of 480^{o}C was used as the binder. This gives a much higher operating range than epoxy [55] and solder paste [56] which have operating limits of 130^{o}C and 170^{o}C, respectively. Another advantage that comes with the use of brazing paste is its higher thermal conductivity as compared to epoxy and solder paste. The constituent elements of brazing paste i.e. Zinc (78%) and Aluminum (22%) are responsible for the increased thermal conductivity.

(a)

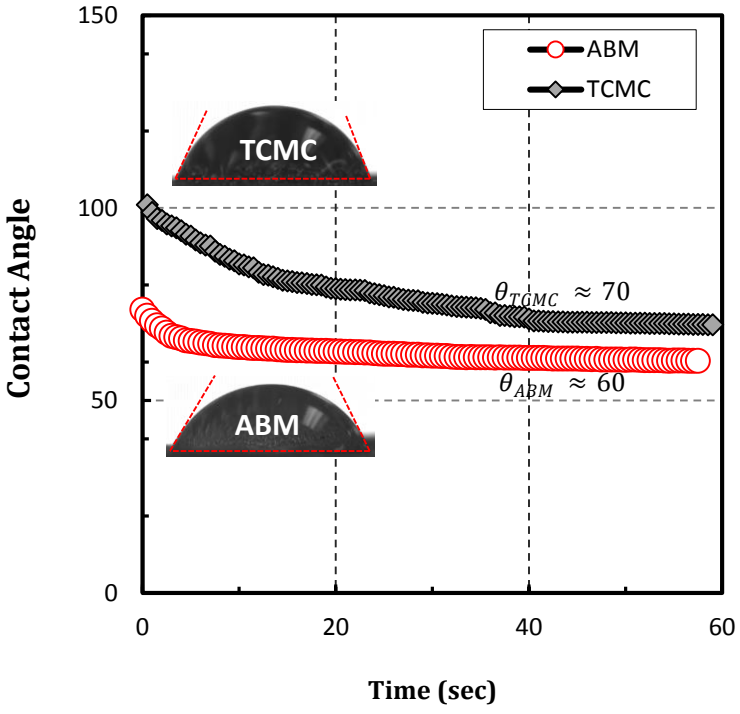

(b)

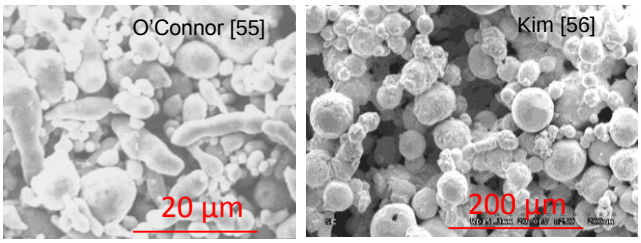

Figure 4-1 (a) Static Contact Angle Measurement and (b) SEM Images

4.1.1 Fabrication

Single side polished silicon wafer was used as a substrate. A hot spot (Fig.3.9) was fabricated on the polished side by using photolithography and liftoff process discussed in section 3.1.3 and the microporous coating was affixed on the rougher side. All the important steps of the aluminum microporous coating fabrication process are shown in Fig. 4.2. The brazing paste used in the current study does not wet the silicon surface. Hence, the surface was metalized by depositing a 400 ^{o}A and 1 µm thick layer of chromium and

aluminum respectively. Chromium acts as adhesive layer between aluminum and silicon substrate. The brazing paste melts at ~480ºC. Under such elevated temperature, the hot-spot which consist of ITO (resistive layer) and nickel (buss bar) can be damaged by the flux component in the brazing paste. Hence, a 1µm thick layer of silicon dioxide is sputtered as a protective layer. This layer also prevents scratching of thin films during coating application. Then, a coating mixture was prepared by mixing 99.7% pure aluminum powder provided by Valimet Inc., Stoddard solvent and brazing paste for aluminum. The solvent was used as a thinner for the brazing paste and evaporates during the brazing process.

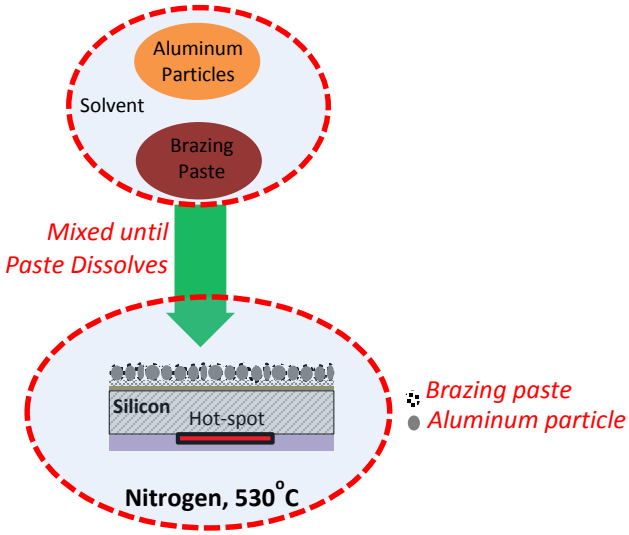

Figure 4-2 Fabrication Process of Aluminum Microporous Coating

The aluminum powder had average particle size of ~10.5 µm. The average particle size was determined by measuring 500 particles using optical microscope. The details of the particles size distribution are shown in Fig. 4.3.

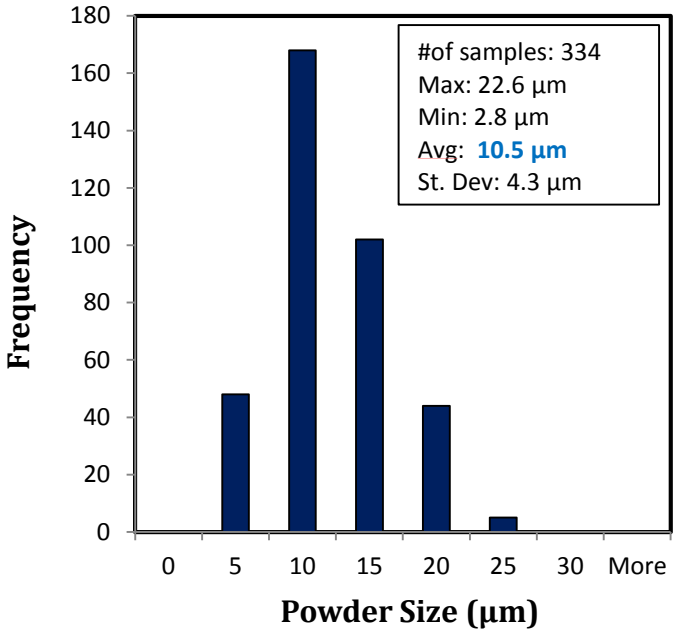

Figure 4-3 Aluminum Particle Size Distribution

The coating mixture was applied on the metalized surface by a spatula and then spread uniformly by shaking the sample. Thus prepared sample was left in the ambient condition for ~ 30 minutes to evaporate the solvent. This is an important step as the non-evaporated solvent can explode during the baking which creates non uniform coating with holes. The next step is to melt the brazing paste to affix aluminum particles to the substrate. A tube furnace was used for this purpose. The brazing process was carried out in a nitrogen environment. The purpose of using nitrogen was to prevent oxidation which is known to hinder the flow of melted brazing paste.

4.1.2 Optimization

An optimization study was conducted to fabricate a coating suitable for the current study. As described earlier, an optimal coating will have high porosity while being as thin as possible. The reduced coating thickness will minimize the water film thickness and

eventually reduce the thermal resistance during evaporation. Additionally, the thinner coating will also reduce the thermal resistance associated with its thickness. The major factor influencing the thickness is particle size used in the coating. Various particle sizes were tested and the minimum thickness attained was ~ 80-100 µm using a particle size of ~10 µm (Fig. 4.3). Further decreasing the particle size could not decrease the coating thickness. This lower limit of coating thickness came from the presence of larger Zn/Al alloy in the brazing paste. The approximate size of the alloy particles was ~80 µm which was determined from the optical microscope. These alloy particles in the paste eventually melt during heating. However, during the application of coating on the silicon substrate, the alloy (~80 µm) supported multi-layer of aluminum particles (~10 µm) on top of each other.

Porosity is defined as the ratio of porous volume to particle and porous volume combined. The maximum porosity is possible when particles adhere to each other and to the substrate without the use of binder. This is possible in metallic substrates using process like sintering. However, it is not a feasible option for silicon substrate. Hence, an optimization study was conducted on particle to paste ratio to achieve higher porosity while maintaining bonding strength. Excessive use of paste can clog up the pores as shown in Fig. 4.4, eliminating potential nucleation cavities for thin film boiling, and less use of paste can result in coating with holes resulting from particle detachment from the substrate (Fig 4.4).

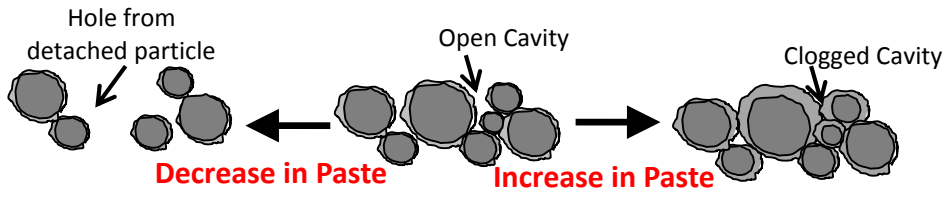

Figure 4-4 Schematic Showing the Effect of Paste Amount in Porosity

With these considerations three different particles to paste ratio 1g: 1.1g, 1g: 1g and 1.g: 0.9g were used to fabricate the coating to find the minimum amount of paste that gives good bonding. The particle size of 10 µm was used in all combinations. It was found that the 1g: 1g ratio succeeded. The porous structure of thus fabricated coating is illustrated by SEM images in Fig. 4.5.

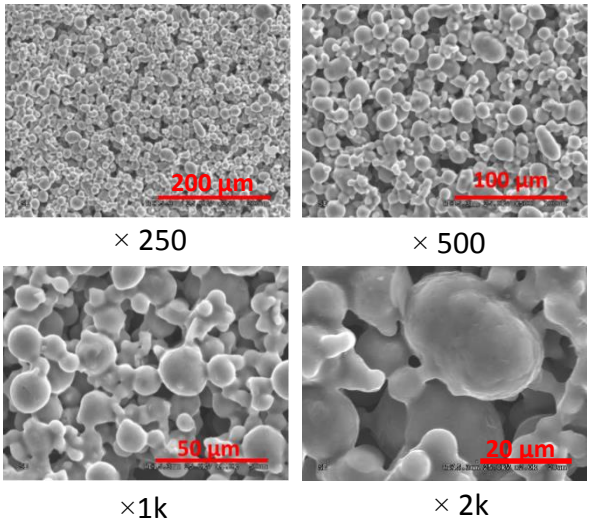

Figure 4-5 SEM Images of Optimum Microporous Coating

(particle/pate = 1g: 1g) at Various Magnifications

4.1.3 Cleaning Process

Flux in the brazing paste helps the melted alloy to wet the substrate and particles during the heating process by removing the oxide. Flux residue reduces the porosity and also makes the coating unstable for the test. Hence, it is vital to eliminate any residue left from brazing process. For this purpose, the coating was immersed for one minute in an ultrasonic bath of 5% alkali and 95% distilled water since the flux residue is soluble in alkali. Then, the sample was thoroughly rinsed with distilled water. Subsequently, the sample underwent sonication for another minute in an acetone bath followed by rinsing with

distilled water. The coating was considered unusable if substantial amount of particles detached from the substrate creating visible holes.

4.1.4 Wetting Characterization

Wetting test was conducted by dispensing a 20 µl distilled water drop on the hot water treated sample and measuring the subsequent wetting area at different time intervals. High speed visualization was used to capture the images and the wetting area was calculated by using image analysis software. The wetting analysis of SHNC conducted in chapter 2 was based on a ~75 nl water drop. Same droplet volume was not possible with aluminum microporous coating since the coating is much thicker (~100 µm) as compared to SHNC (~1µm). If used, 75 nl droplet soaks into the pores of aluminum microporous coating which makes the visual quantification of droplet spreading unfeasible. Hence, the wetting test on microporous coating was conducted with a bigger 20 µl water droplet. The droplet immediately spread upon contact with the coating and spread to the edge of the substrate. The spreading area at various time intervals is plotted in Fig. 4.6. The droplet spreads comparatively faster for the first 20 ms, where the spreading rate is ~2.2 mm^2/ms. Initial spreading is crucial as the hot spot area is smaller as compared to entire chip area (100 mm^2). The comparison with SHNC (Fig 4.6) clearly indicates a similar wetting performance up to ~12 ms. Water droplet spreading rate on aluminum microporous coating exceeds that on SHNC from this point onwards. Initial spreading rate similar to that on SHNC with addition of increased nucleation sites for thin film boiling, validate the potential benefit of the porous structure to further enhance the heat transfer.

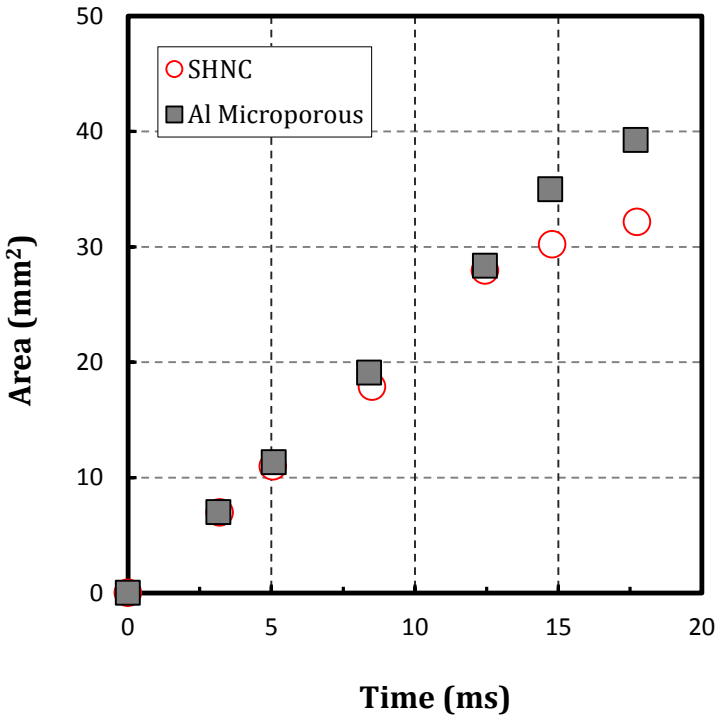

Figure 4-6 a Spreading Speed of a Drop of Water (14 µl) on Aluminum Microporous Coating

The progression of droplet spreading on both the coatings is visually demonstrated in Fig 4.7. It was observed that aluminum microporous coating developed a primary liquid cap and a secondary wetting rim during spreading. Increase in coating thickness increased the spreading rate. However, it also increases the conductive thermal resistance associated with the coating. Thicker coating also loses importance at extremely high heat flux, region of vigorous evaporation, where the thin-film of water breaks causing partial dryout. Hence, the best performance can be achieved by minimizing the coating thickness and maintaining the wettability. For that purpose, smallest possible particle size was used (10 µm). Smaller particles were found to not bind as well.

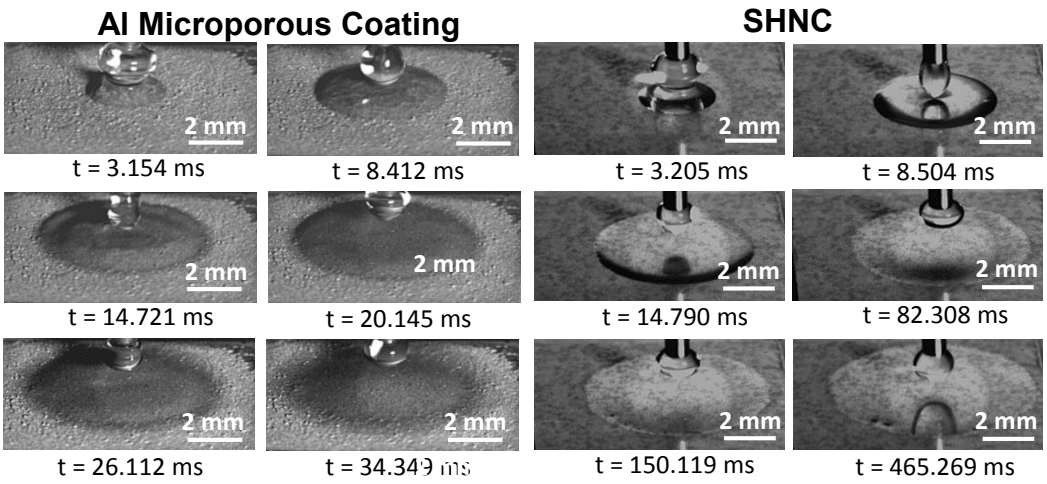

Figure 4-7 Wettability Comparison of Microporous Coating and SHNC.

4.2 Test Result

4.2.1 Cooling Performance Comparison of Aluminum Microporous Coating and Plain Silicon Surface

The baseline case established in Chapter 2, shown in Fig.3.29 has been used to compare the performance of ~100 μm thick aluminum porous structure. The flow rate of 600 Hz with the droplet size of ~75 nl was implemented again. The test results are shown in Fig. 4.8. The results indicate a noticeable enhancement on dry out heat flux as well as hot spot temperature. At the dry-out heat flux (~780 W/cm^2) of plain surface, a reduction of ~80^{o}C in hot spot temperature was attained by using aluminum microporous coating. This further enhancement occurred due to the coatings affinity for water in terms of spreading and to its dense nucleation sites in its porosity. The nucleation sites are of immense value for moderate heat fluxes where thin-film boiling and thin-film evaporation simultaneously remove heat. The high wettability becomes vital at higher heat flux where the delivered dose of water spreads immediately upon contact preventing partial or complete dryout. A

closer look of cooling performance at lower heat flux reveals the onset of phase change heat transfer at an early heat flux of ~120 W/cm^2 as shown in Fig. 4.8.

4.2.2 Performance Comparison of SHNC and Aluminum Microporous Coating

A cooling test on SHNC surface shown in Fig.3.30 in section 3.3 is compared in Fig.4.8 with the aluminum microporous coating.

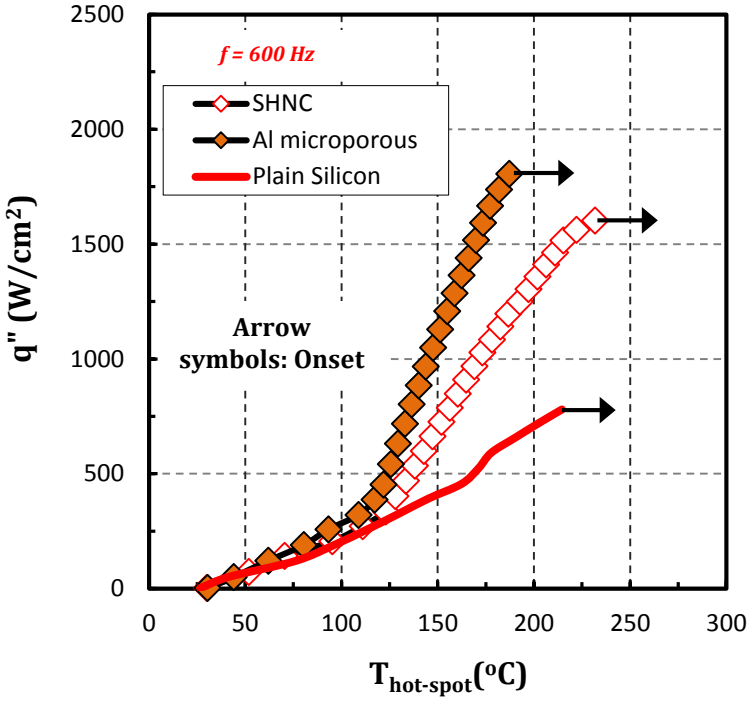

Figure 4-8 Cooling Performance Comparison of Aluminum Microporous Coating and SHNC

The difference in cooling performance is clearly evident starting from a lower heat flux level (~120 W/cm^2) and gets magnified with increasing heat flux. As mentioned earlier, the notion of fabricating microporous coating is to further enhance the performance compared to SHNC. On the microporous coating there is an 8% enhancement in dry-out heat flux relative to that on the SHNC surface. The hot-spot temperature is reduced noticeably at all heat flux levels relative to that obtained with SHNC surface. At 1000

W/cm^2, the hot spot is cooler by ~25^{o}C and the maximum reduction is at the dry-out heat flux (~1602 W/cm^2) of SHNC surface. The hot-spot temperature is cooler by ~60^{o}C for aluminum microporous coating at this heat flux. Closer look at the lower heat flux (~120 W/cm^2) shows the early onset of phase change heat transfer in microporous coating by the shifting to the left of the curve from this point onwards.

The major heat transfer mechanisms are thin-film boiling and thin-film evaporation at moderate heat flux. At lower heat flux few bubbles are observed as the number of nucleation site is proportional to applied heat flux [60]. Figure 4.9 illustrates the regimes observed.

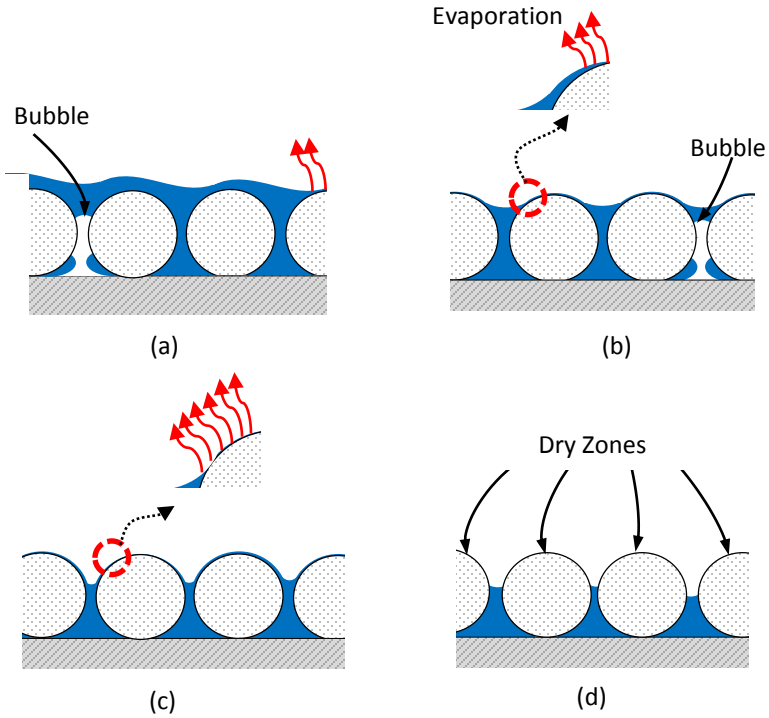

Figure 4-9 Thin-Film Evaporation and Boiling Process in Simplified Representation of Microporous Coating

The bubble grows out of a cavity (Fig. 4.9a) and ruptures immediately after crossing fluid boundary layer. At this point, evaporation is not as dominant as boiling. With the increase of heat flux, rate of evaporation increases as a result of reduction in thin-film thickness. At this point, effective boiling and evaporation are believed to coexist (Fig. 4.9b). Further increasing the heat flux brings the thin-film to the proximity of the mouth of the cavity (Fig. 4.9c). At this point, thin-film evaporation suppresses thin-film boiling. Here, evaporation occurs through a number of thin meniscus formed on the coating. Further increase of heat flux introduces dry zones (Fig. 4.9d) due to insufficient liquid delivery. This is also called a partial dry out. At this point, there exists multiple minute reservoirs on the surface incapable of completely wetting the surface.

4.2.3 Effect of System Temperature

Tests similar to the one explained in section 3.4 was also conducted at various system temperature and atmospheric pressure in gassy condition. The motivation behind this study is to identify the effects of elevated system temperature that can occur due to the components around the chip. Various system temperature was attained and controlled during the test as described in section 3.3.2.3. The test results are plotted in Fig. 4.10. The results clearly indicate minimal effect of system temperature similar to the one reported on the SHNC surface. This, again, can be related to the near saturation temperature inside the micro-gap due to vapor accumulation resulted from vigorous thin-film evaporation/boiling.

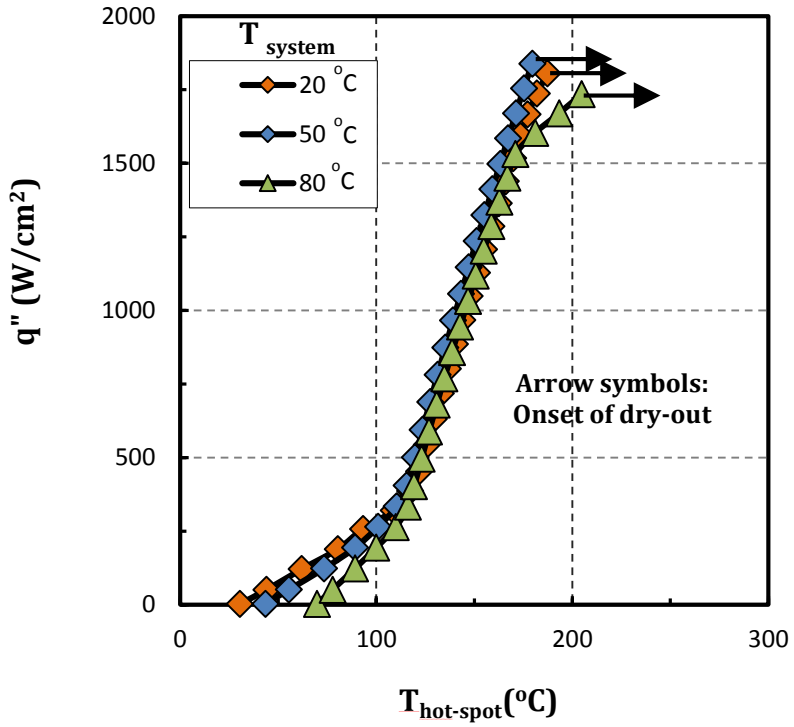

Figure 4-10 Effects of System Temperature on Cooling Performance of Aluminum Microporous Coating

4.2.4 Effect of Surface Orientation

Various scenarios that can pose challenge to the thermal management of hot spot has been tested thus far. This includes elevated system pressure and temperatures. Another parameter that is crucial for microelectronics cooling is system orientation. Space constraint in embedded thermal management may require the coolant delivery at an orientation other than horizontal. Hence, any benefits or penalties of cooling hot-spot at multiple orientations were assessed. Tests were conducted at room temperature and atmospheric pressure at five different orientations which are 0°, 45°, 90°, 135° and 180°. In the present study, change in orientation include both test surface and nozzle orientation,

meaning nozzle is perpendicular to the surface at all orientations. Liquid delivery was maintained at 600 Hz. Test results are shown in Fig 4.11. Tests results are fairly consistent at all orientations except 90^{o} where the performance slightly improved primarily at lower heat flux. This is a direct consequence of excess water removal at lower heat flux by gravity.

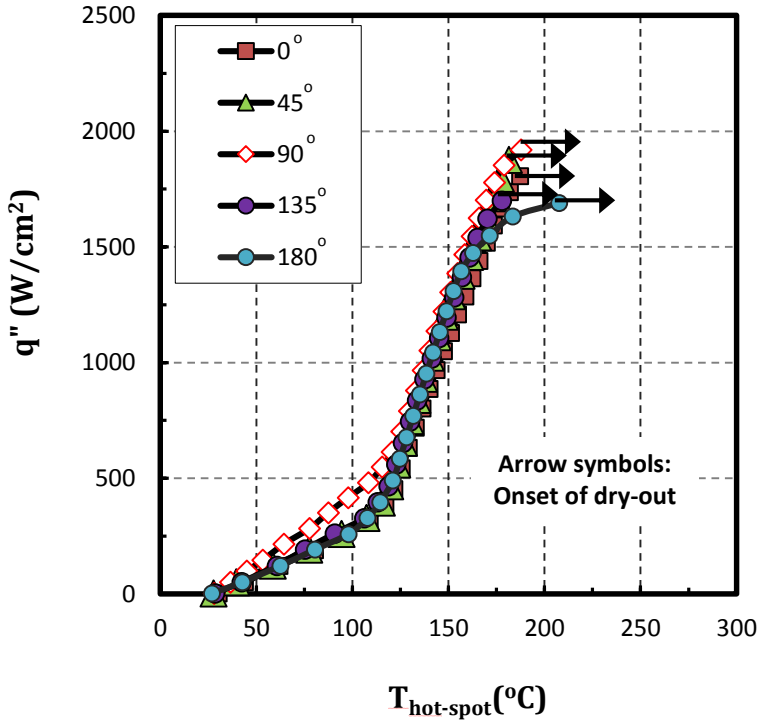

Figure 4-11 Effects of Surface Orientation on Cooling Performance

4.2.5 HTC Comparison between SHNC and Aluminum Microporous Coating

Procedure similar to the one described in section 3.3.3 was followed to estimate and compare the HTC of microporous coating with SHNC surface. The results are shown in Fig. 4.12. Aluminum based microporous coating yields HTC that is 2.5 times higher than that of SHNC surface. The noticeable enhancement in HTC validates the use of highly wettable porous structure for hot-spot cooling.

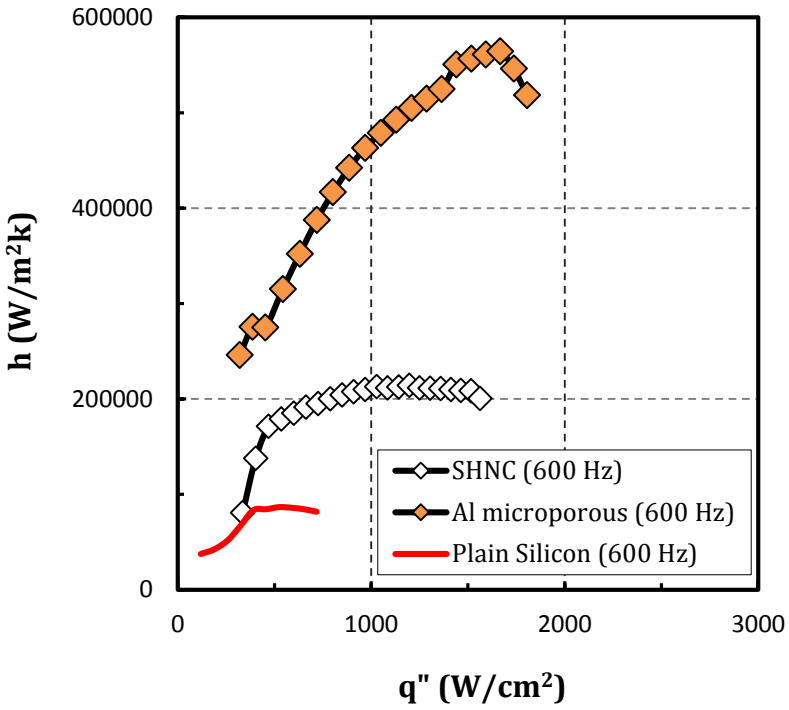

Figure 4-12 HTC Comparison between SHNC and Al Microporous Coating

Chapter 5

Conclusion

5.1 Conclusions of Chapter 2: Nucleate Pool Boiling

1. Only for heat fluxes below 5 W/cm^2, hydrophobic Teflon yielded the best BHT performance, reducing surface superheats relative to plain silicon by up to 5^{o}C. This is explained by the hydrophobicity of the surface which promotes earlier incipience of nucleate boiling compared to the other two surfaces.

2. BHT and CHF were together enhanced as wettability of the test surface increased, with Teflon yielding the worst BHT and gradually transitioning to the lowest CHF of ~13 W/cm^2, followed by intermediately hydrophilic silicon (CHF ≈ 71 W/cm^2), then by aluminum oxide, the most hydrophilic surface, which performed best (CHF ≈125 W/cm^2).

3. The measured CHFs varied linearly with measured static contact angle of each surface, with higher CHF corresponding to lower contact angle (higher wettability). The higher CHF could be explained by the better rewetting of the evaporating microlayer and the accompanying smaller dry spots as wettability increases.

4. The maximum heat transfer coefficient attained by plain and aluminum oxide surfaces are ~20 kW/m^{2}K and ~36 kW/m^{2}K respectively. At 648 kW/m^2, where plain silicon yields the maximum BHT, aluminum oxide reached 28 kW/m^{2}K which is a 40% enhancement in BHT. The trend of improving BHT performance with increasing

wettability (decreasing contact angle), could be explained by more efficient microlayer evaporation resulting from increasing wettability.

5. The bubble over Teflon was larger and became detached above the test surface, leaving behind a small vapor remnant on the surface. On the other test surfaces, the bubbles detached at the base, directly on the test surface. These behaviors appeared consistent and seemed dictated by the respective measured static contact angles on each surface.

6. Due to the vapor remnant on Teflon there was no waiting period on the Teflon test surface, but there was a waiting period on silicon (hydrophilic), and a waiting period 23 times longer than on silicon on aluminum oxide (most hydrophilic). The trend of duration of the ebullition cycle was opposite. The shortest duration occurred on the most hydrophilic surface (0.025 sec), and the longest on the hydrophobic Teflon (1.94 sec).

7. Over aluminum oxide (most hydrophilic) and silicon (hydrophilic), the behavior of the bubble bases seemed to follow the inertia-controlled and heat-transfer-controlled bubble growth phases. Growth of bubble heights on Teflon, unlike for the two wetting surfaces, was influenced by necking and stretching of the bubble as the moment of departure approached.

5.2 Conclusions of Chapter 3: Hot-Spot Cooling by Pulsed Jet Impingement on SHNC

5.2.1 Open Test

1. With water delivered at constant 500 Hz on the SHNC coating made in 10 cycles, dryout heat flux increased up to 4.6 times, to ~1,200 W/cm^2 from ~260 W/cm^2 on the

reference plain Si test surface. The hotspot temperature for the SHNC surface case was ~225^{o}C at the dryout heat flux.

2. Two different modes of heat transfer were observed, which were a mixed mode of thin-film boiling and evaporation at moderate heat flux, and thin-film evaporation only at higher heat flux.

3. Results obtained with the more wettable SHNC coating made in 20 cycles further demonstrated the impact of wettability increase. They showed ~12% enhancement in dryout heat flux and hot spot temperatures reduced by ~19 degrees at 1,000 W/cm^2, relative to those obtained with the coating made in 10 cycles.

4. Effect of mass flow rate on dry-out heat flux was found to be linear, increasing mass flow rate increased the dry-out heat flux.

5. Tests were also conducted with variable mass flow rate, where the delivered mass flow rate for a given heat flux was determined from water dose volume, heat flux and the latent heat of vaporization of the water. By this scheme, applied mass flow rates were much lower than for the constant mass flow rate cases. Compared to constant mass flow rate case of 600 Hz, heat transfer performance was diminished and only thin-film evaporation was observed. No thin-film boiling was detected and thin-film evaporation started even at moderate heat flux of 200 W/cm^2. Dryout heat fluxes reached only up to 800 W/cm^2.

5.2.2 Test in Micro-Gap

6. The narrow vertical space in the micro-gap helps to spread the liquid on the heated plain silicon surface irrespective of its poor wettability. Hence, micro-gap resulted in higher dry-out heat flux (~ 779 W/cm^2) as compared to open test (~ 260 W/cm^2).

7. Optimized SHNC yielded an enhancement of ~105% in dry-out heat flux compared to plain surface due to better and faster rewetting of hot-spot on SHNC. Effects of flow rate were found to be similar to prior results where increasing flow rate yielded increased dry-out heat flux with marginal effect on hot-spot temperature.

8. System temperature was found to have negligible effect on cooling performance. A near-saturation environment which were inside the micro-gap had more influence on cooling performance than the controlled one outside of it. Increase in system pressure slightly degraded the cooling performance. This is attributed to the increased saturation temperature of water with increasing pressure.

9. SHNC yielded higher HTC than plain silicon surface at all heat flux levels. A maximum HTC of 2.2 $\times$ 10^5 W/m^{2}K was achieved at heat flux of 1130 W/cm^2 using aluminum microporous coating. For plain surface, maximum HTC of only 8.5 $\times$ 10^4 W/m^{2}K was achieved at heat flux of 590 W/cm^2.

5.3 Conclusions of Chapter 4: Hot-Spot Cooing by Pulsed Jet Impingement on Aluminum Microporous Coating (Micro-Gap)

1. Aluminum based microporous coating resulted in dry-out heat flux that was more than 2 times higher than that of plain surface. At the dry-out heat flux of plain surface the hot-spot was ~78^{o}C cooler for microporous coating.

2. Compared to the SHNC surface, the microporous coating yielded marginal enhancement in dry-out heat flux, however, hot-spot temperature was lower at all heat flux levels for microporous coating. The maximum difference in hot-spot temperature was found to be ~58^{o}C at ~1602 W/cm^{2}.

3. Maximum HTC of 5.6×10^{5} W/m^{2}Kwas achieved for aluminum based microporous coating. This was an enhancement of more than 2.5 times compared to the SHNC surface (2.1×10^{5} W/m^{2}k).This is attributed to the increased number of nucleation sites for thin-film boiling at moderate heat flux and high wettability to promote thin-film evaporation at higher heat flux, with the aluminum microporous coating.

5.4 Recommendations for the Future Work

1. Increase in surface wettability without changing surface roughness increased the CHF and BHT. A follow up study should focus on the effects of altering the boiling surface roughness by creating a structured patterns like micro pin-fins. Surfaces with diverse wettability can be established by altering the geometry of micro pin-fins. Deposition of aluminum oxide and Teflon on thus fabricated microstructures can further enhance the hydrophilicity and hydrophobicity respectively.

2. Pool boiling tests showed that hydrophobic surface yielded higher BHT at lower heat flux due to early incipience of bubbles, however, the BHT degraded dramatically above 5 W/cm^2. Hence, a mixed surface energy surface, like micro scale patterns of Teflon on plain silicon or aluminum oxide coated surface, could extend the enhancement to higher heat flux level.

3. Enhanced surfaces like SHNC and aluminum based microporous coating resulted in enhanced HTC during liquid cooling of hot-spot by pulsed jet impingement. Thin-film boiling was observed at moderate heat flux as a result of excessive mass flow rate. A better controlled liquid delivery system could further enhance the cooling performance by instigating thin-film evaporation even at lower heat flux.

Appendix A

Additional Test Results

A.1 Nucleate Pool Boiling (Tests on Mixed Surface Energy)

Effect of different wettability on the same boiling surface was investigated by tailoring the surfaces in such a way that only a portion of the silicon surface is coated with Teflon. Three different samples (sample A, sample B and sample C) were prepared as shown in Fig. A.1. Samples A, B and C have a Teflon coating at the center of the surface with sizes of 1 ×1 mm^2, 2 × 2 mm^2 and 3 × 3 mm^2 respectively. The remaining portion of the boiling surface is plain silicon.

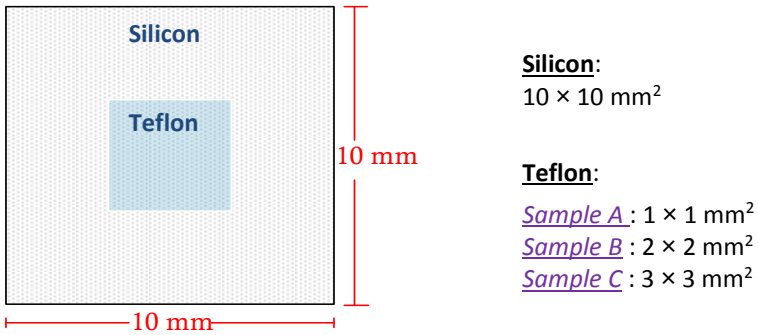

Figure A.1 Surfaces with Mixed Surface Energy

The test results on mixed surface energy are demonstrated in Fig. A.2. the mixed surface energy yielded similar CHF as compared to plain silicon. None of these samples encounter early CHF as shown in Fig. 2.12 by surface completely covered with Teflon coating. Sample A has ~ 52%, sample B and sample C has ~ 44% CHF enhancement as compared to the sample entirely coated with Teflon. BHT continuously degraded with increasing Teflon coated area.

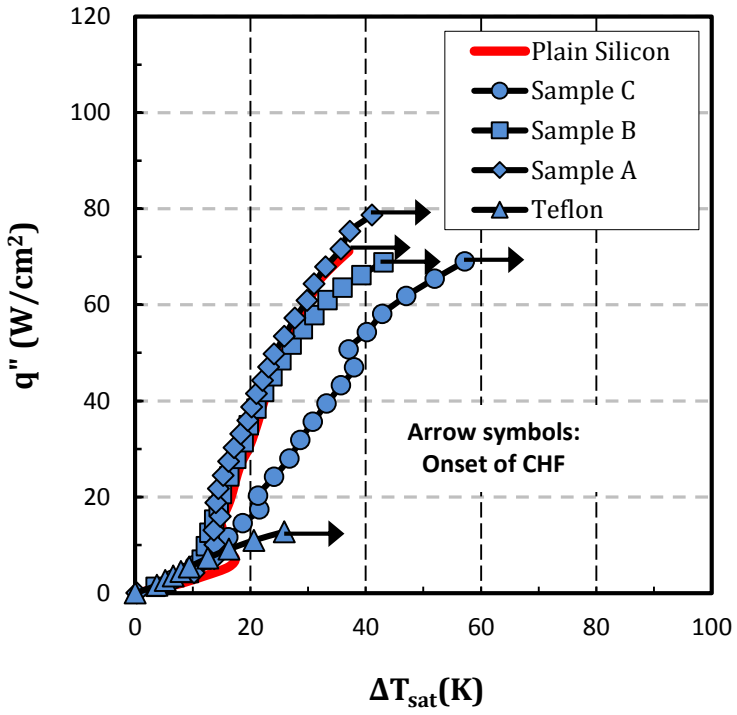

Figure A.2 Pool Boiling Tests on Surfaces with Mixed Surface Energy

The closer look at the lower heat flux region discloses a trend completely opposite to that of Fig. A.2 for BHT. It was found that BHT is enhanced with increasing coverage of Teflon on silicon surface. As shown in Fig. A.3, BHT continuously enhances from plain silicon surface to samples A, B and C which also corresponds to the sequence of increasing Teflon coated area. This indicates that use of Teflon (hydrophobic surface) can be beneficial for BHT if the Teflon coating is pattern in such a way that it prevents the vapor blanketing even at higher heat flux.

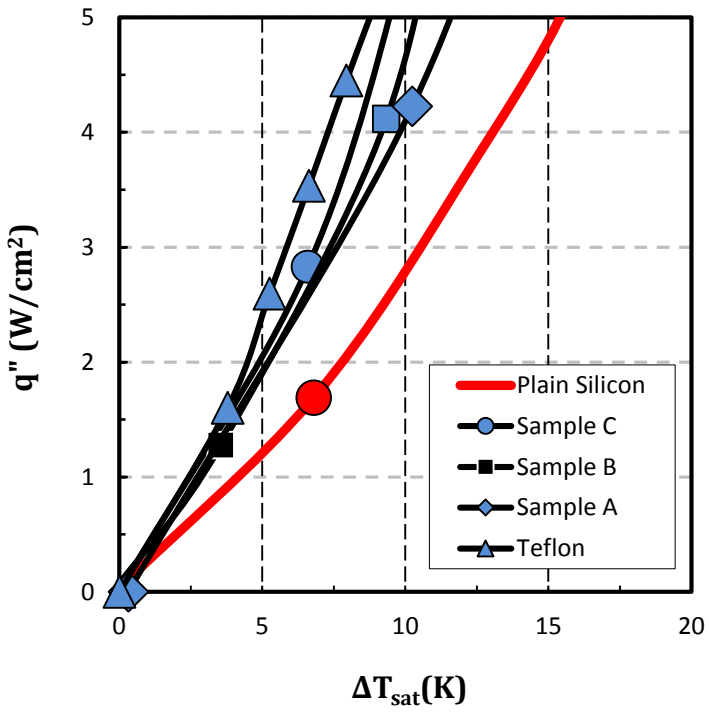

Figure A.3 BHT Comparison at Low Heat Flux

The bubble behavior of case B (2×2 mm^2) was captured at two different heat fluxes of 0.2 W/cm^2 and 5W/cm^2. The images of single cycle of growth and departure at 0.2 W/cm^2 are shown in Fig. A.4 (a). The total period for one cycle was found to be ~556 ms which is ~ 3.5 times shorter than that of the surface entirely coated with Teflon as shown in Fig. A.4. This decrease in time period can be attributed to the lack of bubble base expansion beyond the 2×2 mm^2 Teflon coating. With the reduced base, the net surface tension force, acting parallel to the surface at the triple-contact line also reduces. Figure 9(b) shows the images taken at 5 W/cm^2. At this point there are more than one active nucleation sites on Teflon coated area. The wavy appearance of the liquid vapor interface is due to the merger of various growing bubbles.

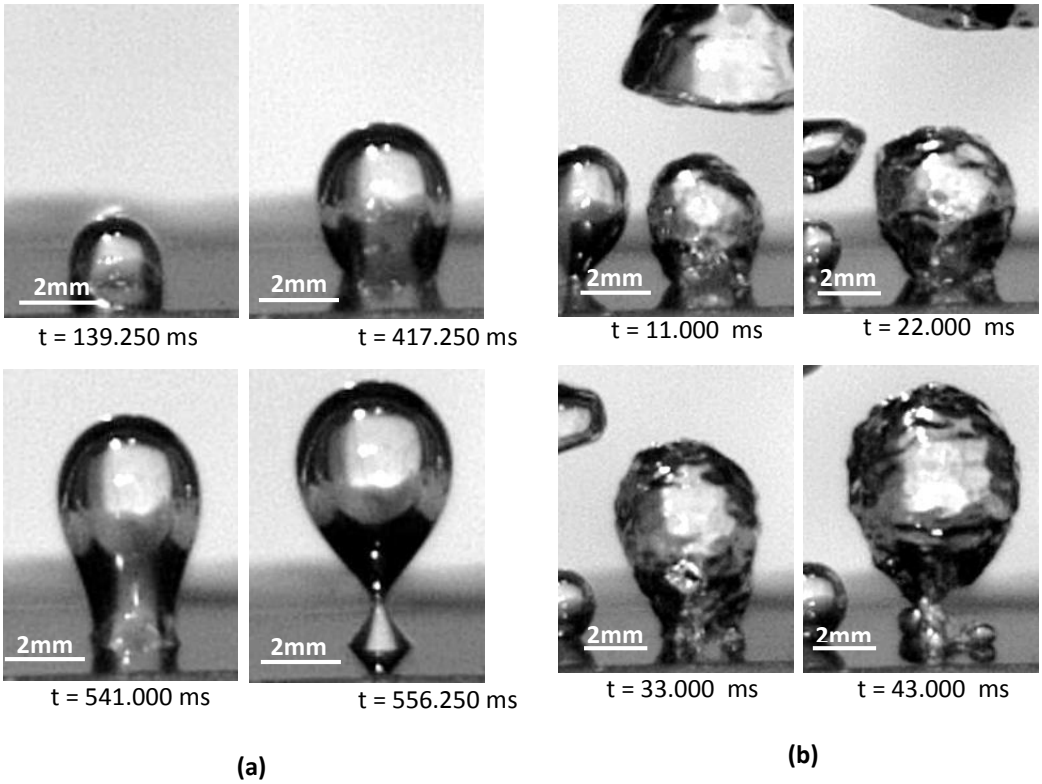

Figure A.4 Images of Bubbles (Case B) at Heat Flux of (a) 0.2 W/cm^2 and (b) 5 W/cm^2.

A.2 Hot-Spot Cooling (Air Assisted Evaporation)

Tests conducted on aluminum based microporous coating (chapter 4) yielded comparatively better performance. This enhancement can be further improved if the vapor accumulated in the micro gap can be eliminated. Hence, in an effort to study the effects of vapor trapped in the micro gap during the test, forced convection by pressurized air was implemented to eliminate the vapor. The details of the scheme is shown in Fig.A.5. Here, all the sides are enclosed unlike previous cases where two sides were left open for vapor removal. The only route for vapor exit is the compressed air outlet at the bottom of the Lexan block.

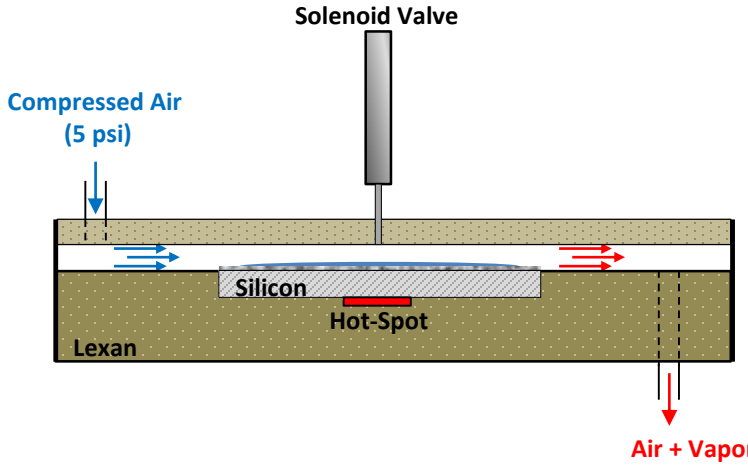

Figure A.5 Schematics of Air Assisted Evaporation Micro-Gap Setup

Compressed air pressure was maintained at 5 psi throughout the testing. And constant flow rate of 600 Hz was used for liquid delivery. Test result is shown in Fig. A.6.

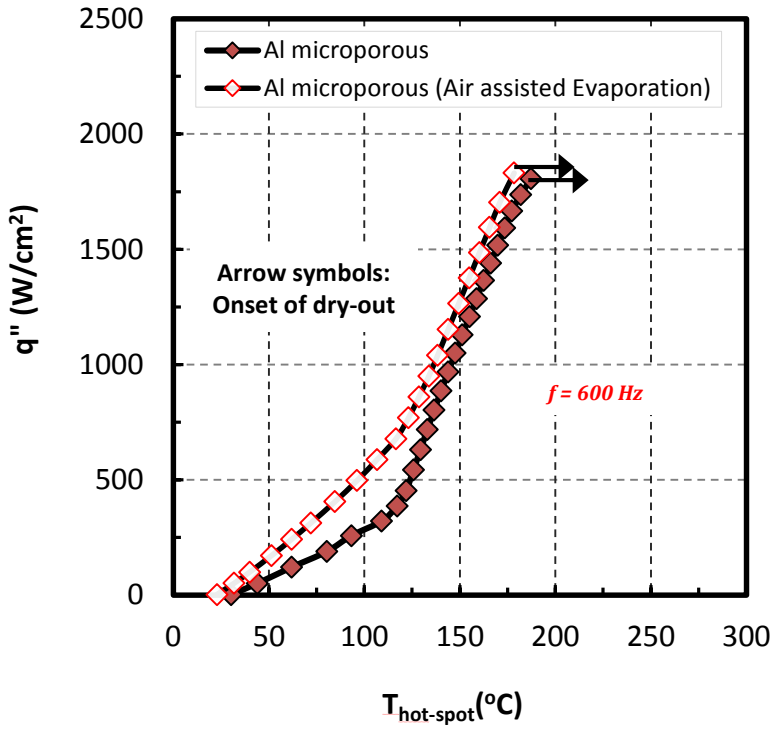

Figure A.6 Effects of Air Assisted Evaporation on Cooling Performance.

It clearly indicates improvement in performance predominantly at lower heat flux. This is due to the removal of excess fluid at lower heat flux similar to the effects of gravity at vertical orientation. At higher heat flux (above 800 W/cm^2) where vapor accumulates due to vigorous evaporation, there seem to be a constant reduction in hot-spot temperature by ~9^{o}C up to the dry-out heat flux.

A.2 Hot-Spot Cooling (Spray Cooling)

Hot-spot cooling test similar to the one conducted in chapter 4 was repeated using a spray nozzle. The spray nozzles delivers coolant water at higher mass flow rate as compared to liquid delivery system shown in Fig. 3.1. The test setup is shown in Fig. A.7.

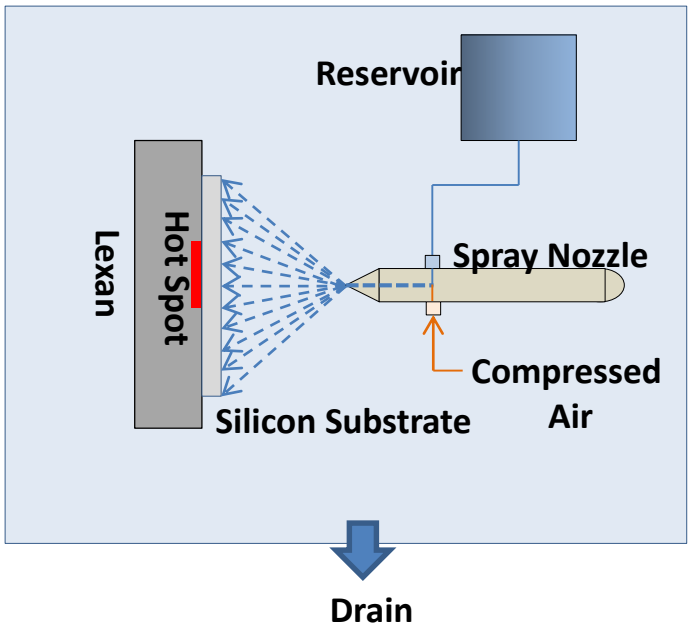

Figure A.7 Spray Cooling Test Setup

Images from high speed camera (Fig. A.8) was used to estimate the cone angle of the spray nozzle and was found to be 47±4^o.

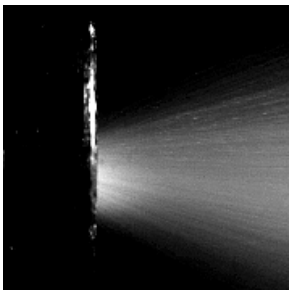

Figure A.8 Spray Nozzle

The sauter mean diameter was calculated by using equation A.1 [62] and was found to be 107 µm.

$$d_{32} = 3.67 d_o [We_{d_o}^{\frac{1}{2}} Re_{d_o}]^{-0.259} \quad \text{(A.1)}$$

The flow rate of the spray nozzle was calibrated with the applied compressed air pressure and shown in Fig. A.9

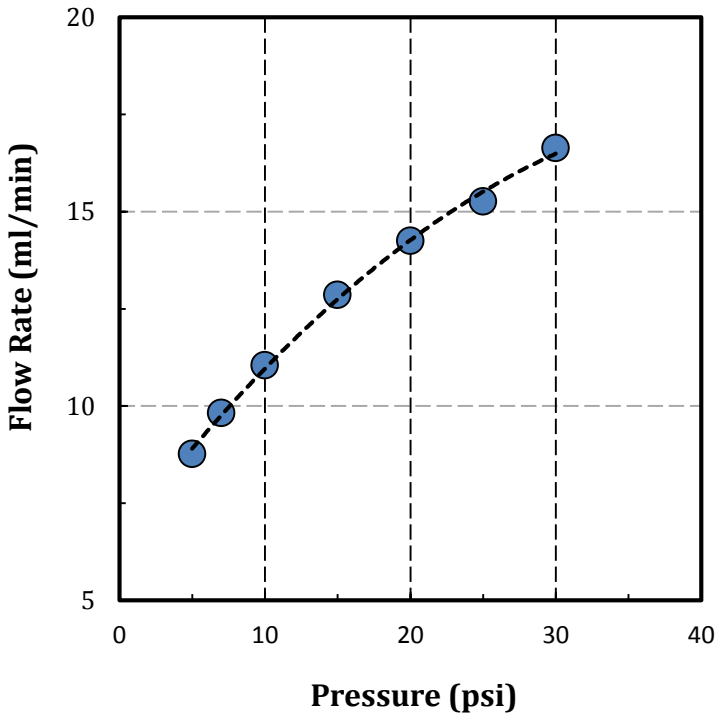

Figure A.9 Flow Rate Calibration

The test results are shown in Fig. A.10 and was also compared with the jet impingement tests (vertical orientation) conducted in chapter 4.

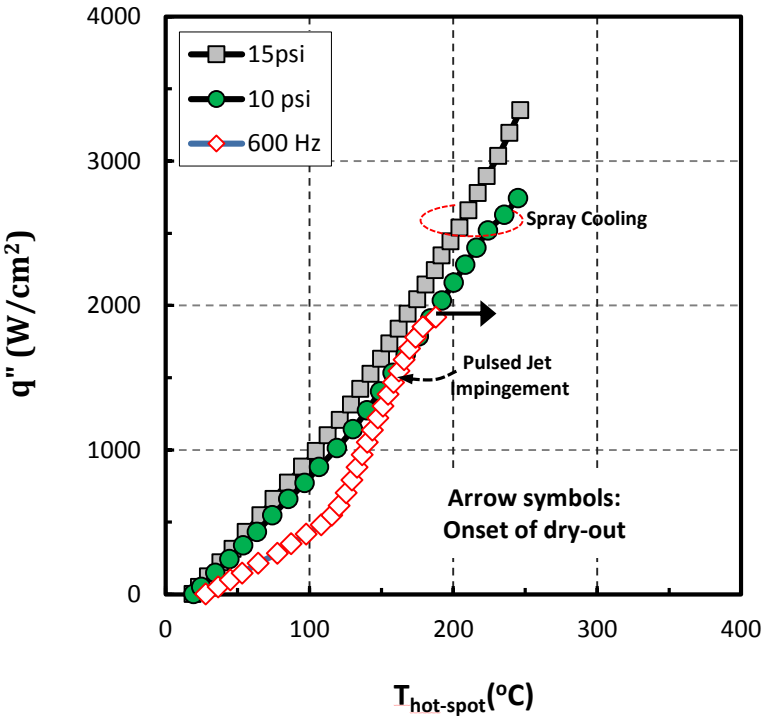

Figure A.10 Spray Cooling Test Results

Table A.1 Volumetric Flow Rate Comparison of Solenoid Valve and Spray Nozzle

Liquid Delivery	Pressure (psi)	Frequency (Hz)	Flow Rate (ml/min)
Spray Nozzle	15 psi	-	12.86
Solenoid Valve	15 psi	600 Hz	2.66

References

1 H. Honda, H. Takamastu and J.J. Wei, "Enhanced Boiling of FC-72 on Silicon Chips with Micro-pin-fins and Submicron Scale Roughness," *J. Heat Transfer,* vol. 124, pp. 383-390, 2002.

2 S. Ujereh, T. Fisher and I. Mudawar, "Effects of Carbon Nanotube Arrays on Nucleate Pool Boiling," *Int. J. Heat and Mass Transfer,* vol. 50, pp. 4023-4038, 2007.

3 S.M. You, J. H. Kim and K. H. Kim., "Effect of Nano-particles on Critical Heat Flux of Water in Pool Boiling Heat Transfer," *Applied Physics Letters,* vol. 83, no. 16, pp. 3374-3376, 2003.

4 G. Moreno, S. Narumanchi and C. King, "Pool Boiling Heat Transfer Characteristics of HFO-1234yf on Plain and Microporous- Enhanced Surfaces," *J. Heat Transfer,* vol. 135, p. 111014, 2013.

5 S. G. Liter and M. Kaviany, "Pool-Boiling CHF Enhancement by Modulated Porous-Layer Coating: Theory and Experiment," *Int. J. Heat Mass Transfer,* vol. 44, pp. 4287-4311, 2001.

6 A.B.D. Cassie and S. Baxter, "Wettability of Porous Surfaces," *Trans. Faraday,* vol. 40, pp. 546-551, 1944.

7 R.N. Wenzel, "Resistance of Solid Surfaces to Wetting by Water," *Ind. Eng. Chem.,* vol. 28, pp. 988-994, 1936.

8 J.H. Kim, “Enhancement of Pool Boiling Heat Transfer Using Thermally-Conductive microporous Coating Techniques*,”* Arlington: University of Texas at Arlington, 2006.

9 k.N. Rainey and S.M. You, "Pool Boiling Heat Transfer From Plain and Microporous, Square Pin-Finned Surfaces in Saturated FC-72," *Journal of heat Transfer,* vol. 122, pp. 509-516, 2000.

10 R.F. Gaertner and J.W. Westwater, "Population of Active Sites in Nucleate Boiling Heat Transfer," *Chem. Eng. Prog. Symp. Series,* vol. 56, pp. 39-48, 1960.

11 Y.Y. Hsu and R.W. Graham , “Transport Processes in Boiling and Two-Phase Systems,” Hemisphere, 1976.

12 K. Yamagata, F. Hirano, K.Nishikawa and H. Matsuoka, "Nucleate Boiling of Water on the Horizontal Heating Surface," *Mem. Fac. Engr, Kyushu,* pp. 99-163, 1955.

13 N. Zuber, "Hydrodynamic Aspects of Boiling Heat Transfer," Physics and Mathematics, AEC Report No. AECU-44, 1959.

14 J. H. Lienhard, V.K. Dhir and D.M. Riherd, "Peak Pool Boiling Heat Flux Measurements on Finite Horizontal Flat Plate," *J. Heat transfer,* vol. 95, pp. 477-482, 1973.

15 K. H. Sun and J.H. Lienhard, "The Peak Pool Boiling Heat Flux on Horizontal Cylinders," *Int. J. Heat and Mass Transfer,* vol. 13, pp. 1425-1439, (1970).

16 J. S. Ded and J.H. Lienhard, "The Peak Pool Boiling Heat Flux from a Sphere," *AIChE Journal,* vol. 18, pp. 337-343, 1972.

17 S.K.R. Chowdhury and R.H.S. Winterton, "Surface Effects in Pool Boiling," *Int. J. Heat Mass Transfer,* vol. 28, pp. 1881-1889, 1985.

18 Y. Takata, S. Hidaka, M. Masuda and T. Ito, "Pool Boiling on a Superhydrophilic Surface," *Int. J. Energy Res.,* vol. 27, pp. 111-119, 2003.

19 S. P. Liaw and V.K. Dhir, "Effect of Surface Wettability on Transition Boiling Heat Transfer from a Vertical Surface," *Proceedings of the Eighth International Heat Transfer Conference*, San Francisco, 1969.

20 Y. Takata, S. Hidaka and T. Uraguchi, "Boiling Feature on a Super Water-repellent Surface," *Taylor and Francis,* vol. 27, pp. 25-30, 2006.

21 Y. A. Kirichenko and P.S. Cherniakov, "Determination of the First Critical Thermal Heat Flux on Flat Heaters," *J. Eng. Phys.,* vol. 20, pp. 699-702, 1973.

22 Y. Haramura and Y. Katto, "A New Hydrodynamic Model of Critical Heat Flux, Applicable Widely to Both Pool and Forced Convection Boiling on Submerged Bodies in Saturated Liquids," *Int. J. Heat Mass Transfer,* vol. 26, pp. 389-399, 1983.

23 P. Sadasivan, P.R. Chappidi, C. Unal and R.A. Nelson, "Possible Mechanism of Macrolayer Formation," *Int. Comm. Heat Mass Transfer,* vol. 19, pp. 801-815, 1992.

24 S. Kandlikar, "A Theoretical Model to Predict Pool Boiling CHF Incorporating Effects of Contact Angle and Orientation," *J. Heat Transfer,* vol. 123, pp. 1071-1078, 2001.

25 V. P. Carey, “Liquid Vapor Phase Change Phenomena,” Washington, DC: Hemisphere, 1992.

26 B.B. Mikic and W.M Rohsenow, "A New Correlation of Pool Boiling Data Including Effect of Heating Surface Characteristics," *J. Heat Transfer,* vol. 124, pp. 245-250, 1969.

27 H. Jawurek, "Simultaneous Determination of Microlayer Geometry and Bubble Growth in Nucleate Boiling," *Int. J. Heat and Mass Transfer,* vol. 12, pp. 843-848, 1969.

28 M.G. Cooper and A.J.P. Lloyd, "The Microlayer in Nucleate Pool Boiling," *Int. J. Heat and Mass Transfer,* vol. 12, pp. 895-913 , 1969.

29 Y.H. Zhao, T. Masuoka and T. Tsuruta, "Unified Theoretical Prediction of Fully Developed Nucleate Boiling and Critical Heat Flux Based on Dynamic Microlayer Model," *Int. J. Heat and Mass Transfer,* vol. 45, pp. 3189-3197, 2002.

30 Y. Utaka, Y. Kashiwabra and M. Ozaki, "Microlayer Structure in Nucleate Boiling of Water and Etanol at Atmospheric Pressure," *International Journal of Heat and Mass Transfer,* vol. 57, pp. 222-230, 2013.

31 S.J. Kline and F.A. McClintock, "Desribing Uncertainties in Single Smaple Experiments," *Mechanical Engineering,* vol. 75(1), pp. 3-8, 1953.

32 S.M Kwark, G. Moreno, R. Kumar, H. Moon and S.M. You, "Nanocoating Characterization in Pool Boiling Heat Transfer of Pure Water," *International Journal of Heat and Mass Transfer,* vol. 53, pp. 4579-4587, 2010.

33 Y. Nam, J. Wu and G. a. J. Y. Warrier, "Experimental and Numerical Study of Single Bubble Dynamics on a Hydrophobic Surface," *J. Heat Transfer,* vol. 131, p. 121004, 2009.

34 H. Jo, H.S. Ahn, S. Kang and M.H. Kim, "A Study of Nucleate Boiling Heat Transfer on Hydrophilic, Hydrophobic and Heterogeneous Wetting Surfaces," *Int. J. Heat and Mass Transfer,* vol. 54, pp. 5643-5652, 2011.

35 A. H. Howard and I. Mudawar, "Orientation Effects on Pool Boiling Critical Heat Flux (CHF) and Modeling of CHF for Near-Vertical Surfaces," *Int. J. Heat and Mass Transfer,* vol. 42, no. 9, p. 1665–1688, 1999.

36 M. Ohadi, S. V. Dessiatoun, K. Choo and M. Pecht, "A Comparison Analysis of Air, Liquid, and Two-Phase Cooling of Data Centers," in *Semiconductor Thermal Measurement and Management Symposium (SEMI-THERM), 28th Annual IEEE* , 2012.

37 B. Agostini, M. Fabbri, J. E. Park, L. Wojtan, J. R. Thome and B. Michel, "State of the Art of High Heat Flux Cooling Technologies," *Heat Transfer Eng., Taylor & Francis,* vol. 28, no. 4, pp. 258-281, 2007.

38 J. Jiang, Y.-X. Tao and L. Byrd, "Evaporative Heat Transfer From Thin Liquid Film on a Heated Cylinder," *Int.J.Heat Mass Transfer,* vol. 43, no. 1, pp. 85-99, 2000.

39 C. Höhmann and P. Stephan, "Microscale Temperature Measurement at an Evaporating Liquid Meniscus," *Exp.Therm.Fluid Sci.,* vol. 26, no. 2-4, pp. 157-162, 2002.

40 H. Wang, S. V. Garimella and J. Y. Murthy, "Characteristics of an Evaporating Thin Film in a Microchannel," *Int.J.Heat Mass Transfer, vol. 50, 19–20,* no. 19-20, pp. 3933-3943, 2007.

41 H.K. Dhavaleswarapu, S.V. Garimella, J.Y. Murthy, "Microscale Temperature Measurements Near the Triple Line of an Evaporating Thin Liquid Film," *Journal of Heat Transfer,* vol. 131, no. 6, pp. 061501(1)-061501(7), 2009.

42 C.-C. Hsieh and S.-C. Yao, "Evaporative Heat Transfer Characteristics of a Water Spray on Micro-Structured Silicon Surface," *Int.J.Heat Mass Transfer*, vol. 49, 962-974, 2006.

43 J.H. Kim, S.M. You and S.U.S. Choi, "Evaporative Spray Cooling of Plain and Microporous Coated Surfaces," *Int.J.Heat Mass Transfer,* vol. 47, no. 14–16, pp. 3307-3315, 2004.

44 C.H. Amon, S.-C. Yao, C.-F. Wu and C.-C. Hsieh, "Microelectromechanical System-Based Evaporative Thermal Management of High Heat Flux Electronics," *Journal of Heat Transfer,* vol. 127, no. 1, pp. 66-75, 2005.

45 A. Bar-Cohen, G. Sherwood, M. Hodes and G. Solbreken, "Gas-Assisted Evaporative Cooling of High Density Electronic Modules," *IEEE Transactions on Components, Packaging, and Manufacturing Technology: Part A,* vol. 18, no. 3, pp. 502-509, 1995.

46 S. Narayanan, A. Fedorov and Y. Joshi, "On-Chip Thermal Management of Hotspots Using a Perspiration Nanopatch," *J Micromech Microengineering,* vol. 20, no. 7, p. 75010, 2010.

47 Y. Takata, S. Hidaka, M. Masuda and T. Ito, "Pool Boiling on a Superhydrophilic Surface," *Int.J.Energy Res.,* vol. 27, no. 2, pp. 111-119, 2003.

48 Y. Nam, S. Sharratt, C. Byon, S.-J. Kim and Y. Ju, "Fabrication and Characterization of the Capillary Performance of Superhydrophilic Cu Micropost Arrays," *Journal of Microelectromechanical Systems,* vol. 19, no. 3, pp. 581-588, 2010.

49 R. Chen, M.-C. Lu, V. Srinivasan, Z. Wang, H.H. Cho and A. Majumdar, "Nanowires for Enhanced Boiling Heat Transfer," *Nano Letters,* vol. 9, no. 2, pp. 548-553, 2009.

50 S.M. Kwark, M. Amaya, R. Kumar, G. Moreno and S.M. You, "Effects of Pressure, Orientation, and Heater Size on Pool Boiling of Water with Nanocoated Heaters," *Int.J.Heat Mass Transfer,* vol. 53, no. 23-24, pp. 5199-5208, 2010.

51 K. Nishikawa, Y. Fujita, H. Ohta and S. Hidaka, "Effects of System Pressure and Surface Roughness on Nucleate Boiling Heat Transfer," *Memoirs of the faculty of Engineering, Kyushu University. ,* 1982.

52 R. King, M. Amaya and S.M. You, "Evaporative Cooling Preformance of a Brazed Microporous Coating on an Aluminum Surface.," in *Proceedings of ASME International Mechanical Engineering and Exposition*, Houston, 2012.

53 M.P. Mughal and O.A. Plumb, "An experimental study of boiling on a wicked surface," *Int. J. Heat Mass Transfer,* vol. 39, no. 4, pp. 771-777, 1996.

54 C. Li, G.P. Peterson and Y. Wang, "Evaporation/Boiling in Thin Capillary Wicks (I) - Wick thickness Effects," *Journal of Heat Transfer,* vol. 128, pp. 1312-1319, 2006.

55 J.P. O'Connor and S.M. You, "A painting Technique to Enhance Pool Boiling Heat Transfer in Saturated FC-72," *J. Heat Transfer ,* vol. 117, pp. 387-393, 1995.

56 J.H. Kim, "Enhancement of Pool Boiling Heat Transfer Using Thermally-Conductive Microporous Coating Technique," University of Texas at Arlington, 2006.

57 J. Min and R.L. Webb "Long-Term Wetting and Corrosion Characteristics of Hot Water Treated Aluminum and Copper Fin Stocks," *International Journal of Refrigeration,* vol. 25, p. 1054–1061, 2002.

58 K.R. Zavadil, "Inducing and Imaging Localized Passivity Breakdown in Aluminum using an AFM Approach," *Electrochemical Society,* vol. 11, no. 22, pp. 13-21, 2008.

59 N. Nikaido, S. Shirai and M. a. U. S. Iihashi, "Process for Coating Aluminum Aluminum Alloy". Patent 3945899, 23 March 1976.

60 R.F. Gaertner and J.W. Westwater, "Population of Active Sites in nucleate Boiling Heat Transfer," *Chem. Eng. Prog. Symp. Series,* vol. 56, pp. 39-48, 1960.

61 K.A. Estes and I. Mudawar, "Correlation of Sauter Mean Diameter and Critical Heat Flux for Spray Cooling of Small Surfaces," *Int. J. Heat Mass Transfer,* vol. 38, pp. 2985-2996, 1995.

Biographical Information

Shailesh Malla obtained his Bachelor of Science in Mechanical Engineering from the University of Texas at Arlington in 2008. He then continued to work for the doctorate degree in the Micro-Scale Heat Transfer Laboratory at the University of Texas at Arlington. His research focused on nucleate boiling and thin-film evaporation on enhanced silicon surfaces.